IDENTIFYING THE SOURCES AND VARIABILITY OF SOLAR $F_{10.7}$ WITH DIFFERENTIAL EMISSION MEASURES

BY

SAMUEL JOSEPH SCHONFELD, B.A., M.S.

A dissertation submitted to the Graduate School

in partial fulfillment of the requirements

for the degree

Doctor of Philosophy

Major Subject: Astronomy

New Mexico State University

Las Cruces New Mexico

December 2017

"Identifying the Sources and Variability of Solar $F_{10.7}$ with Differential Emission Measures," a dissertation prepared by Samuel Joseph Schonfeld in partial fulfillment of the requirements for the degree, Doctor of Philosophy, has been approved and accepted by the following:

Louí-Vicente Reyes
Dean of the Graduate School

R. T. James McAteer
Co-Chair of the Examining Committee

Stephen M. White
Co-Chair of the Examining Committee

Date

Committee in charge:

Dr. R. T. James McAteer, Co-Chair

Dr. Stephen M. White, Co-Chair

Dr. Jason Jackiewicz

Dr. David Voelz

Dr. Rene Walterbos

ACKNOWLEDGMENTS

I must first acknowledge the financial support that has facilitated my dissertation research. Much of this is in the form of large research grants: the Air Force Office of Scientific Research grants LRIR 14RV14COR, LRIR 17RVCOR416, and FA9550-15-1-0014 awarded to Stephen White, the NSF Career Award 1255024 awarded to James McAteer, and the PAARE NSF:0849986 grant awarded to Bernard McNamara. In addition, I was personally awarded two years of funding through the New Mexico Space Grant (a NASA EPSCoR branch) and was supported for four summers by the Air Force Research Laboratory Scholars Program to perform research with Stephen White on Kirtland Air Force Base in Albuquerque, NM. I have also received numerous smaller awards that facilitated my travel to specific conferences including: the New Mexico State University College of Arts and Sciences Travel Grant, the American Astronomical Society Solar Physics Division Studentship Award, and the SHINE student travel award. I am grateful to these and other institutions that have supported me financially during graduate school.

The guidance I received from mentors in graduate school, both professional and academic, has been fundamental to my success. James McAteer, thank you for all your support and for always helping me focus on the things that matter. Stephen White, it has been such a fun experience working with you. You have been so patient with the slow progress of the research whenever I'm away from AFRL and so understanding of my stubborn skepticism when I'm there. Rachel Hock-Mysliwiec, I really appreciate you taking the time (especially with all your new responsibilities) to work with me on research and help me think about future

career options, it has been invaluable. Carl Henney, thank you for all your input on the science and for helping me annoy Stephen with research details during our excellent cubicle breaks.

I have been guided by so many incredible people during my life and education, and all of them have helped me complete this dissertation in some way. I can't possibly mention everyone, but know that you mean so much to me.

To my whole family who have been wonderfully supportive and always interested in my progress. Mom, thank you so much for your constant support (and occasional reality checks) and for taking the reigns when it came to college searching. Without you I never would have ended up at Whitman and where I am today. I'm sorry I kept ignoring you every time you suggested I should take a break, but I think you'll agree that pushing straight through all 23.5 years of school has worked out alright. Dad, I think it was watching you with all your research and teaching that helped guide me into science. I suspect that your telescope and that one short summer astronomy class at the SRJC also had some influence on my field of study. I wish I hadn't picked up quite as much of your habit of working late nights to a deadline, but I'm so glad we've been able commiserate over our now shared graduate school experience. Grandma Muriel and Grandpa Hy, thank you so much for your support (both emotional and financial) during college and graduate school. The help you have given me paying for my education has been remarkably freeing and made the process so much less stressful than I know it could have been.

I have also had the privilege to learn from phenomenal teachers in nurturing school environments that shaped my perspective on education and got me to

graduate school in the first place. No matter how many new buildings, I will always feel comfortable when I visit Summerfield Waldorf School, and I am so grateful for the 10 years I was privileged to walk those grounds, learning to learn. Mr. Berg, your love of physics and dry humor helped me find my passion even in an unfamiliar and often overwhelming high school environment. Andrea Dobson, your enthusiasm and energy are infectious, and I'm so glad my first real tour of the universe was with you. Nathaniel Paust, thank you for putting up with me senior year and for taking me on as a student, even before you really wanted to. I'm sorry for the extra paperwork. The entire Whitman community, you helped me recharge and refocus for four years, and I will always consider Walla Walla my first home away from home.

I've also had the privilege to study with some great friends while learning about the universe. Brit, thank you for convincing me to take that first astronomy class. You changed my life for the better. To the Scatter Plots, thank you for all those whiteboard sessions that got us through classes. A special thank you to Laura for always having the time to discuss research issues, and for bringing yours to me. To Jean and Sean, two thirds of the house/office mate trio. To Xander and Emma, I always enjoy being able to emerge from my room and have someone to talk to, anytime day or night. And of course, Candace. Thank you for making sure I eat well, sharing stories, and showing me how (and occasionally how not) to write a thesis.

Finally, I have received exceptional logistical support that has significantly smoothed some of the rough edges of graduate school. To Ofelia Ruiz and Lorenza Sanchez, you are both amazing. The science that I (and everyone in the Astronomy department) do would come grinding to a halt without the buffer that you

provide between us and the administrative details of NMSU. To Jeff Coughlin, thank you for providing this excellent LaTeX template. It saved me countless hours of formatting nightmares.

VITA

November 21, 1989	Born in Santa Rosa, California
2012	B.A., Physics, Astronomy with Honors, *Magna cum Laude* Whitman College Walla Walla, Washington, USA
2015	M.S., Astronomy New Mexico State University Las Cruces, New Mexico, USA

PROFESSIONAL AND HONORARY SOCIETIES

American Astronomical Society (Solar Physics Division)

American Geophysical Union

American Physical Society

Phi Beta Kappa

Sigma Xi

PUBLICATIONS

Schonfeld, S.J. et al. 2015, The Astrophysical Journal, 808, 29. *Coronal Sources of the Solar $F_{10.7}$ Radio Flux*

Schonfeld, S.J. et al. 2017, The Astrophysical Journal, 844, 163. *The Slowly Varying Corona. I. Daily Differential Emission Measure Distributions Derived from EVE Spectra*

FIELD OF STUDY

Major Field: Astronomy

ABSTRACT

IDENTIFYING THE SOURCES AND VARIABILITY OF SOLAR $F_{10.7}$ WITH DIFFERENTIAL EMISSION MEASURES

BY

SAMUEL JOSEPH SCHONFELD, B.A., M.S.

Doctor of Philosophy

New Mexico State University

Las Cruces, New Mexico, 2017

Dr. R. T. James McAteer, Co-Chair

Dr. Stephen M. White, Co-Chair

The solar corona emits high-energy Extreme Ultraviolet (EUV) light that is absorbed in the Earth's upper atmosphere, creating the ionosphere. Understanding how changes in the Sun's EUV emission influence the terrestrial atmosphere is important, but, due to the absorption, EUV can not be observed from the ground. Instead, a common proxy measurement is $F_{10.7}$, the 10.7 cm (2.8 GHz) solar microwave flux density measured at 1 AU. $F_{10.7}$ is produced in the same coronal plasma as EUV and they correlate well over solar cycle timescales.

However, $F_{10.7}$ is typically averaged over 81 days when used as a proxy because there are known short-term discrepancies in its relationship with EUV: it varies

much more over a typical solar rotation than does EUV. This is due to the presence of two different coronal $F_{10.7}$ emission mechanisms, bremsstrahlung that correlates extremely well with EUV, and gyroresonance that has no direct relationship with EUV emission. The purpose of this research is to determine the contribution of each of these mechanisms to the $F_{10.7}$ flux and variability.

A test study is performed using a set of EUV images from the Atmospheric Imaging Assembly to compute differential emission measures (DEMs, a measure of the plasma thermal content) that are used to predict an $F_{10.7}$ bremsstrahlung image. This is compared with an imaging observation of $F_{10.7}$ taken with the Very Large Array and proves the ability to identify both bremsstrahlung and gyroresonance emission with DEMs. Using the lessons from this initial analysis, four years of full-Sun DEMs are computed from EUV Variability Experiment spectra. This reveals an unexpected temporal bimodality in the coronal thermal structure. These DEMs are used to predict the bremsstrahlung emission at five microwave frequencies including $F_{10.7}$ and then the relative contribution of bremsstrahlung and gyroresonance emission is determined both spectroscopically and using the DEM predictions. Bremsstrahlung emission is found to dominate the coronal $F_{10.7}$ except during short periods of intense activity near solar maximum. A bremsstrahlung correction to $F_{10.7}$ is calculated and compared to the traditional $F_{10.7}$ proxy, revealing the fundamental limitation of its efficacy as a single-input EUV proxy.

Contents

LIST OF TABLES

LIST OF FIGURES

LIST OF ABBREVIATIONS

AIA	Atmospheric Imaging Assembly
CCD	Charge-Coupled Device
CIRA	Committee on Space Research International Reference Atmosphere
CoMP	Coronal Multichannel Polarimeter
COSPAR	Committee on Space Research
CSRH	Chinese Spectra Radioheliograph
DEM	Differential Emission Measure
EIT	Extreme Ultraviolet Imaging Telescope
EM	Emission Measure
EOVSA	Expanded Owens Valley Solar Array
ESA	European Space Agency
EUV	Extreme Ultraviolet
EUVAC	Extreme Ultraviolet flux model for Aeronomic Calculations
EUVE	Extreme Ultraviolet Explorer
EVE	Extreme Ultraviolet Variability Experiment
FIP	First Ionization Potential
FWHM	Full-Width Half Max
HMI	Helioseismic and Magnetic Imager
IDL	Interactive Data Language
ISS	International Space Station
LASCO	Large Angle Spectroscopic Coronagraph
MCMC	Markov chain Monte Carlo
MEGS	Multiple Extreme Ultraviolet Grating Spectrographs
NASA	National Aeronautics and Space Administration
NoRH	Nobeyama Radioheliograph
NoRP	Nobeyama Radio Polarimeters
NRAO	National Radio Astronomy Observatory
PINTofALE	Package for Interactive Analysis of Line Emission
RHESSI	Reuven Ramaty High-Energy Solar Spectroscopic Imager
SDO	Solar Dynamics Observatory
SEE	Solar Extreme Ultraviolet Experiment
SOHO	Solar and Heliospheric Observatory
SSN	Sunspot Number
SVD	Singular Value Decomposition
TIMED	Thermosphere, Ionosphere, and Mesosphere Energetics and Dynamics
TSI	Total Solar Irradiance
VLA	Very Large Array

1. INTRODUCTION

The Sun is the primary energy source in the solar system and as such any fluctuations in solar forcing can have dramatic effects on Earth and the near Earth environment. The most obvious examples of this include the diurnal variation caused by the daily revolution of the Earth about its rotation axis and the annual variation caused by the combination of the tilt of this rotation axis and the orbit of the Earth around the Sun. Intrinsic solar variability can also impact the terrestrial environment, although this variation has strong wavelength dependence and therefore impacts different parts of the terrestrial environment in very different ways. The response of the atmosphere to changes in solar forcing is the subject of study in various sub-disciplines of atmospheric research (e.g. climatology and aeronomy) and the motivation for this dissertation.

Specifically, the upper atmosphere (ionosphere-thermosphere) is particularly sensitive to high-energy Extreme Ultraviolet (EUV, $10 - 121$ nm, and even higher energy) light which is emitted by the solar atmosphere. This emission varies with solar activity over the course of the 11-year solar cycle but observational constraints make it difficult (and until sounding rockets and satellites, impossible) to measure. Instead, various proxies of solar activity are used to approximate this high-energy solar forcing. The most popular of these is the $F_{10.7}$ (10.7 cm, 2.8 GHz) solar radio flux that is used in numerous terrestrial ionosphere models (e.g., Jacchia 1971; Hedin et al. 1977; Ridley et al. 2006; Bowman et al. 2008; Bilitza et al. 2014). The goal of this dissertation is to evaluate the efficacy of $F_{10.7}$ in this application by studying the direct relationship between $F_{10.7}$ and EUV emission.

1.1. The Earth's Atmosphere

The terrestrial atmosphere is typically considered to have five layers as shown in Figure 1.1 which are, increasing in altitude, the: troposphere, stratosphere, mesosphere, thermosphere, and exosphere. These layers are defined based on the complex atmospheric temperature profile which is caused by altitude variable heating and cooling rates due to the interplay of chemical stratification and solar irradiation (National Research Council 1981). Humans occupy the troposphere but visit the upper layers with the help of various technologies, entering the stratosphere on high-altitude polar-route commercial plane flights, and orbiting the Earth in the thermosphere on the International Space Station (ISS).

The density and composition differences in the atmospheric layers influence how they interact with the solar irradiance. As light passes through the atmosphere, it is absorbed and scattered by atoms and molecules in the atmosphere. Each chemical species in the atmosphere has ranges of the solar spectrum that it interacts with, and with a significant concentration of specific molecules, whole regions of the Sun's spectrum can be absorbed in the atmosphere. The most famous example of this is the ozone layer, a dynamic $\sim$30 km thick over-density of O_3 in the stratosphere centered at $\sim$35 km. Ozone dissociates into O and O_2 when it absorbs UV light in the 200–300 nm range, preventing this light that can damage living cells from reaching the ground (Anderson & Muench 1985).

1.1.1. The Ionosphere-Thermosphere

A similar photoabsorptive filtering process occurs in the upper mesosphere and thermosphere (extending approximately $70 - 1000$ km above the Earth's sur-

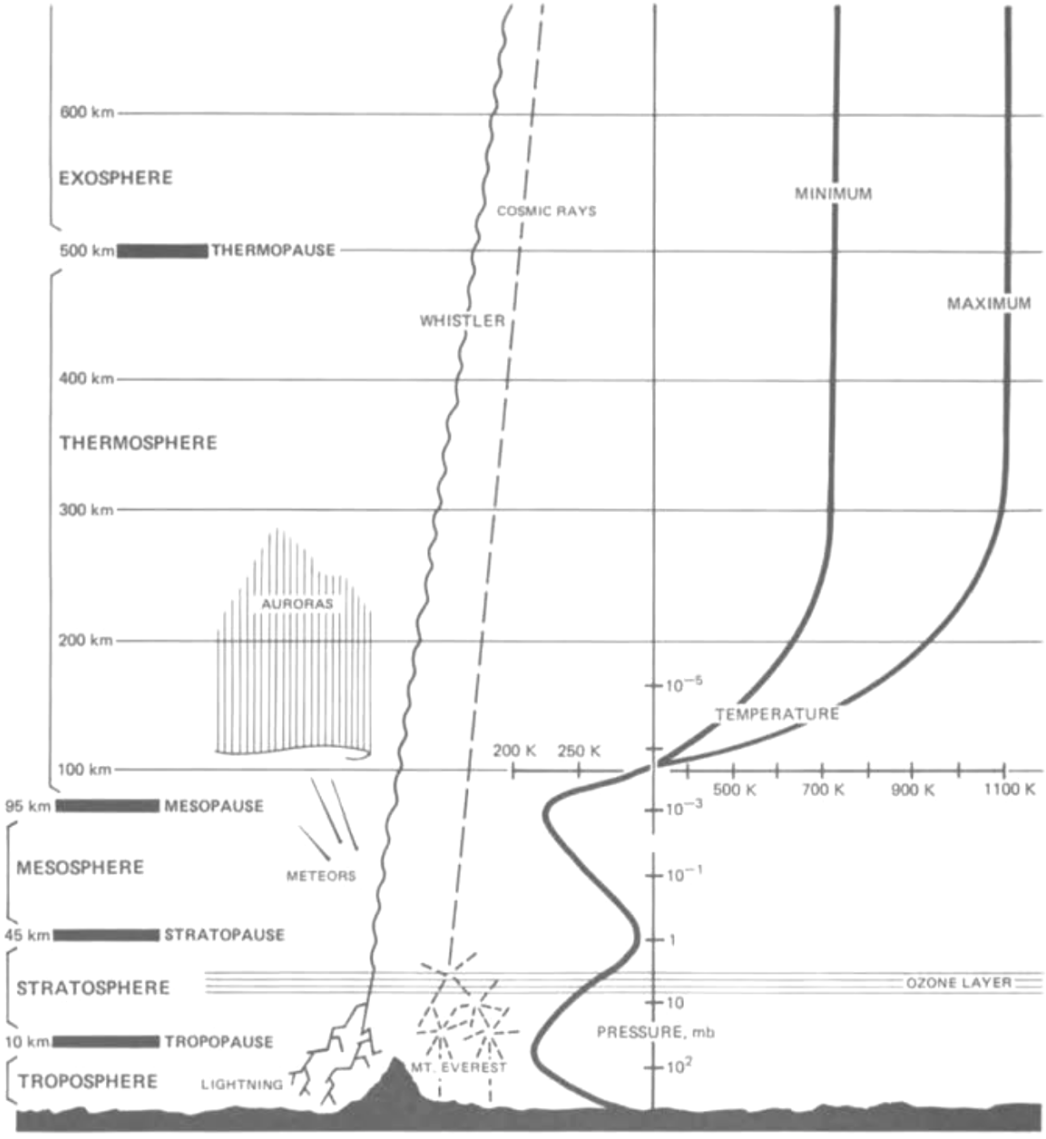

Fig. 1.1.— A shematic of the neutral layers of the Earth's atmosphere. The layers, their boundaries, and their approximate altitudes are given on the left while the atmospheric temperature profile (at solar minimum and solar maximum) with altitude and pressure is shown on the right. Various features in the atmosphere (most notably the Ozone layer and the extent of auroras) are also indicated for context. (National Research Council 1981)

face (Rich 1985)), where EUV light is absorbed by primarily O, O_2, and N_2 (see Figure 1.2, Haigh 2004)[1]. This light has high enough energy that when it is absorbed it dissociates molecules and ionizes the reacting atom or molecule, releasing an electron (Tobiska 1996). As the electron velocity thermalizes it deposits its kinetic energy into the atmosphere, causing it to heat and expand[2]. Because of this ionization in the thermosphere the layer is often referred to as the ionosphere-thermosphere, where the ionosphere refers to the ionized constituents (electrons and ions), and the thermosphere to the neutral constituents (atoms and molecules).

The ionosphere has a complex vertical structure (see Figure 1.3) determined by the interplay of the absorption cross sections of the atmospheric constituents and the incoming solar EUV spectrum. During the day, abundant Lyman-α (1216 Å) and higher energy X-ray photons penetrate to and are absorbed by the upper mesosphere and bottom of the thermosphere, creating the ionospheric *D region*. Just above this at 95–140 km, Lyman-β (1026 Å), soft X-rays, and the UV continuum produce the *E region*. This layer becomes much less pronounced at night, but remains present constantly due to transport from the day-side ionosphere. The next layer is divided into two parts, the *F1 region* (140–200 km) and the *F2 region* (200-400 km) that are both produced primarily by the absorption of

[1]There is no special affinity between these molecules and EUV light. The EUV interaction in the thermosphere (as opposed to other atmospheric layers) is due to the increasing atmospheric density as light propagates towards the ground; higher altitudes simply have insufficient atmosphere to signififcantly attenuate the incoming spectrum. As the most abundant atmospheric constituents, atomic and molecular nitrogen and oxygen naturally cause the majority of the absorption. For a review of the interaction cross-sections of various atmospheric molecules see Hudson (1971).

[2]The dynamics involved in heating this region of the atmosphere are complex, with external forcing both from the mesosphere below and the magnetosphere above. An introduction to these effects can be found in Schrijver & Siscoe (2009) chapters 10 and 11.

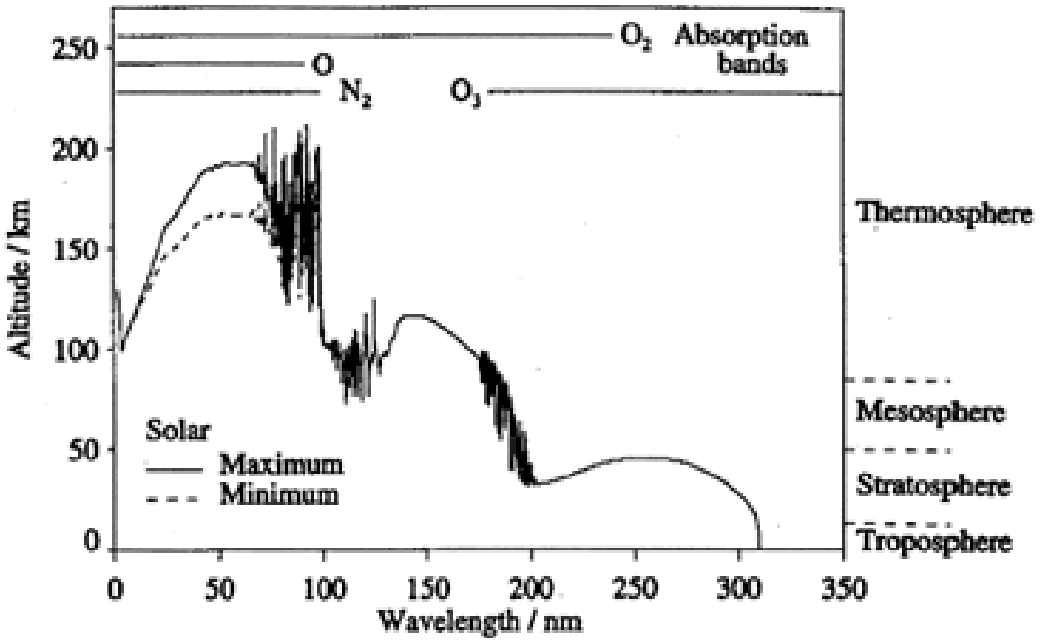

Fig. 1.2.— The altitude of peak atmospheric absorption of Ultraviolet light as a function of wavelength for solar maximum (solid) and solar minimum (dashed). The dominant absorbing atoms and molecules and their relevant absorption ranges are shown at the top of the plot. The only solar activity dependence appears in the EUV range which is absorbed in the ionosphere-thermosphere. (Haigh 2004)

He II 304 Å light as well as the 100–800 Å continuum. The *F1 region* is present only during the day while the *F2 region* is sustained at night due to transport processes, although with decreased density and increased altitude. Above these, the *Topside Ionosphere* extending into the exosphere is generated by transport of ions and electrons from the lower ionospheric layers. This overview is drawn from Rich (1985) and more detail about the physics and dynamics of the ionosphere-thermosphere can be found in Schunk & Nagy (2004)

Most of the EUV light that generates the ionosphere (and nearly all of the EUV variability) is produced in the corona (discussed in Chapter 1.2), the outer, highly-variable, layer of the solar atmosphere. This coronal variability leads to

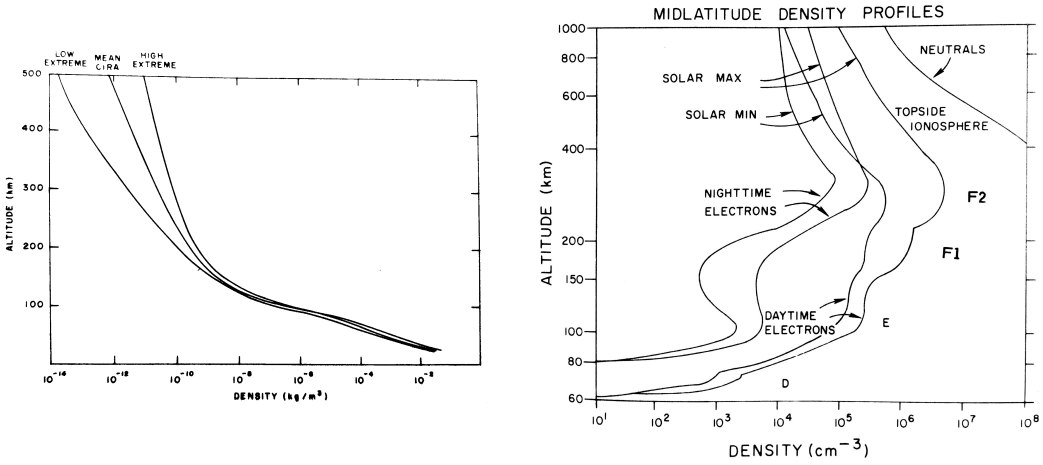

Fig. 1.3.— *Left:* mean thermosphere neutral density profiles derived from the Committee on Space Research (COSPAR) International Reference Atmosphere (CIRA 1972) model atmosphere at various levels of solar activity (Champion et al. 1985). *Right:* average ionospheric electron density profiles for various solar activity and illumination conditions (Rich 1985). The *D*, *E*, *F1*, and *F2* layers and the Topside Ionosphere are indicated along with a characteristic total neutral density profile for reference.

order of magnitude changes in the thermospheric neutral density and the ionospheric electron density (figure 1.3) on time-scales of hours to years depending on the relevant solar processes. It is extremely important to understand ionosphere-thermosphere variability because a significant fraction of satellites (including all current manned space vehicles) orbit within this atmospheric layer (Tobiska 1996). Changes in the thermospheric neutral density cause variations in satellite drag (e.g., De Lafontaine & Garg 1982) and the ionospheric electron density influences material surface charging properties (e.g., Garret 1985) and communications stability (e.g., Dandekar 1985; Klobuchar 1985; McNamara 1985), all of which impact mission safety, longevity, and effectiveness.

Because of the impact on satellite operations, significant effort has been exerted towards modeling the ionosphere-thermosphere region. This began in the

early 1960's with one dimensional models, based on satellite kinematics, that measure total atmospheric density at the orbit altitude, and sounding rocket flights measuring atmospheric density and composition. The first models were designed to describe the atmosphere at given solar times and activity levels (Mathur & Mitra 1960; Paetzold & Zschorner 1961; Martin et al. 1961; CIRA 1961; Kallmann-Biji & Sibley 1964) characterized by the $F_{10.7}$ index described in Chapters 1.3 and 6. These quickly evolved into activity dependent models based on satellite drag observations (King-Hele & Walker 1961; Anderson 1962; King-Hele & Rees 1963; Paetzold 1963; King-Hele & Quinn 1965; Bhatnagar & Mitra 1966) and heat conduction calculations (Nicolet 1961; Jacchia 1964) that soon became time dependent with the inclusion of the equations of hydrostatic equilibrium (Harris & Priester 1962; CIRA 1965). By the early 1970's a sufficient understanding was developed to create reference atmospheres (e.g., CIRA 1972), models that represented temporally averaged atmospheric profiles for specific latitudes, solar times, and activity levels. These quickly developed into full three dimensional, time, and solar and geomagnetic activity dependent thermosphere models (e.g., Barlier et al. 1978; Fuller-Rowell & Rees 1980; Dickinson et al. 1981). Today, a full treatment of ionospheric modeling involves coupling the time dependent light, particles, and magnetic fields of the entire Sun-Earth system from the solar corona and the inner heliospheric environment down through the magnetosphere and into the ionosphere-thermosphere (Tóth et al. 2005).

1.2. The Solar Corona

The atmosphere of the Sun, a schematic of which is shown in Figure 1.4, has components in a wide range of temperatures and densities and can there-

fore be broken into multiple layers which are studied with unique methods. The photosphere is the visible surface of the Sun that is seen with optical continuum observations and is generally taken as the $\sim$ 500 km thick layer between where the Sun becomes optically thick (opaque) in optical wavelengths and the solar temperature minimum of $\sim 4,300$ K (Gingerich et al. 1971; Altrock et al. 1985). The next layer is the chromosphere (Lockyer 1868), so named because it was first observed as a red ring around the Sun during total solar eclipses. This red coloring is due to hydrogen recombination and H_α emission (e.g., Leenaarts et al. 2012), and this type of atomic line emission is seen in all levels of the solar atmosphere above the photosphere. Next is the highly dynamic transition region which is a boundary layer between the chromosphere and the corona. In the space of only $\sim$ 500 km the density decreases by an order of magnitude while the temperature increases by nearly two orders of magnitude (Mariska 1986). Lastly is the corona, the hottest and least dense layer of the solar atmosphere. The corona (which means "crown" in Latin) got its name because, like the chromosphere, it can only be observed with the eye during total solar eclipses when it appears as a faint, tenuous, often spiked ring encircling the Sun (Golub & Pasachoff 2010).

Figure 1.4 represents an idealized, one dimensional corona. The true corona is a highly dynamic and complex structure that responds primarily to the emergence of magnetic field from the solar interior (Golub & Pasachoff 2010). One common feature in the corona is an active region, a volume of hotter and denser plasma that is structured by closed magnetic fields extending from underlying sunspots and that appears bright in the EUV (e.g., Brickhouse & Schmelz 2006; Tripathi et al. 2008; Teriaca et al. 2012; Iwai & Shibasaki 2013). Large, coherent regions of open magnetic field are typically observed as coronal holes, extended dark patches in

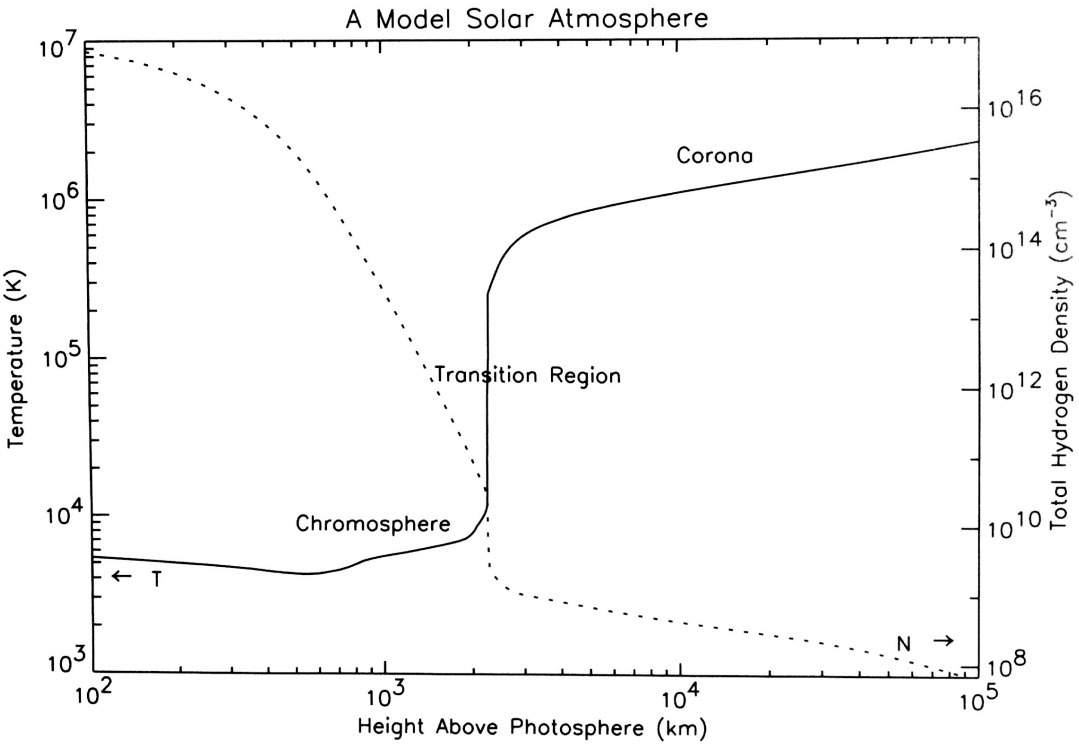

Fig. 1.4.— The plasma temperature (solid) and Hydrogen density (dotted) as a function of height above the optically thick solar surface. (Courtesy of G. Avrett) (Golub & Pasachoff 2010)

the corona (e.g., Zirker 1977). These low density and temperature regions (Munro & Withbroe 1972; Doschek et al. 1997, e.g.,) are nearly ubiquitous at the magnetic poles (e.g., Krieger 1977) but can reach to low latitudes (even occasionally crossing the equator as in Timothy et al. 1975) and are the source of the fast solar wind (e.g., Krieger et al. 1973; Lukianova et al. 2017; Tokumaru et al. 2017). The corona also contains other, typically smaller, coherent structures such as filament channels (e.g., Makarov et al. 1982; Martin et al. 1994; Knizhnik et al. 2015) and prominences (e.g., Nasmyth 1852; Moe et al. 1979; Zhang et al. 2016), and all of them are manifestations of different magnetic field topologies. Examples of various coronal structures can been seen in Figure 1.5.

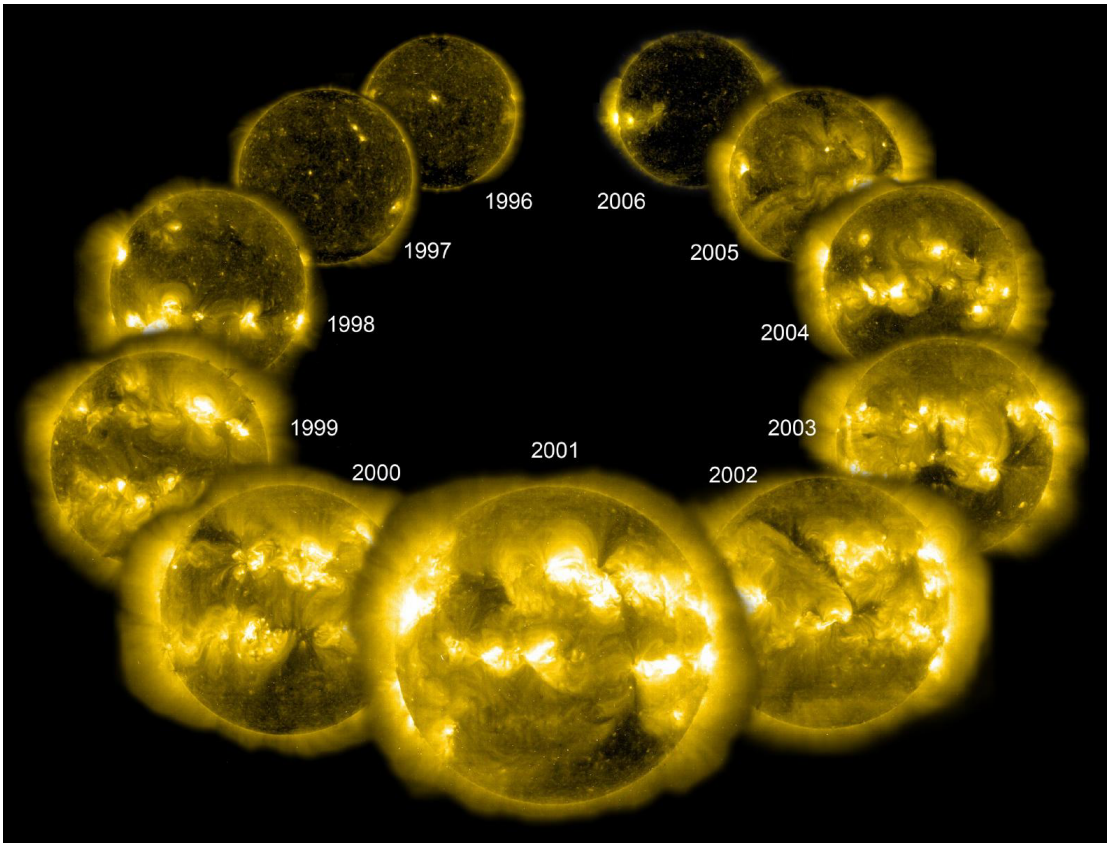

Fig. 1.5.— The 11 year solar cycle as observed by the National Aeronautics and Space Administration (NASA) / European Space Agency (ESA) Solar and Heliospheric Observatory (SOHO) Extreme Ultraviolet Imaging Telescope (EIT) in the 284 Å bandpass dominated by Fe XV emission. As the underlying photospheric magnetic field evolves, the corona responds, with increasing activity and emission during solar maximum. (Assembled by Steele Hill)

In addition to spatial variations, the magnetic field forcing of the corona also produces significant temporal variability. Consequently, coronal activity follows the same 11 year roughly sinusoidal variation as the sunspot cycle (Golub & Pasachoff 2010). At solar minimum (1996 and 2006 in Figure 1.5) the corona is generally quiet, with fewer and smaller active regions (if any) and large coronal holes visible as dark voids at the poles. During solar maximum (2000–2002) the corona is filled with large, bright active regions, and the complex magnetic topol-

ogy can lead to coronal holes at any latitude. One of the principle research areas in solar physics is understanding and predicting this cycle variability, especially as it relates to the effects it has in the corona (e.g., Javaraiah 2016).

1.2.1. Coronal Emission

As a hot plasma, there are various physical mechanisms in the corona that produce light across the electromagnetic spectrum. For example, the Large Angle Spectroscopic Coronagraph (LASCO) onboard the Solar and Heliospheric Observer (SOHO) satellite (Brueckner et al. 1995) observes the outer corona in Thomson scattered white light, and the Coronal Multichannel Polarimeter (CoMP) instrument observes emission lines of Fe XIII in the infra-red to measure coronal magnetic fields (Tomczyk et al. 2008). However, due to the bright photospheric black body emission in the UV, visible, and infra-red, the corona is most commonly studied using low energy (microwave and radio) and high-energy (EUV and X-ray) light. In general, emission from a magnetized plasma such as the corona can be broken into three categories: collisionally activated, magnetically induced, and bulk plasma emission (Kundu 1965).

Collisionally induced emission is any light produced by the collision between electrons and atoms. This includes collisionally excited atomic line emission (bound-bound), radiative recombination (free-bound), and bremsstrahlung (free-free, Rybicki & Lightman 1979, German for "breaking radiation"), all of which are mediated by electron-ion collisions in the plasma. The intensity of bremsstrahlung emission is uniquely determined by the bulk plasma properties while both collisionally excited line emission and radiative recombination are also influenced by

the detailed physics of the interacting atom (Rybicki & Lightman 1979). Coronal emission lines are seen discretely across the electromagnetic spectrum but most prominently in the EUV and soft X-ray (Golub & Pasachoff 2010) while bremsstrahlung is a true continuum emission process and is observed both at low energies in the microwave and radio (Kundu 1965) and at high energies in the X-ray (Golub & Pasachoff 2010).

Magnetically induced emission results from electrons accelerating around magnetic fields due to the Lorentz interaction of individual electrons within the bulk plasma (Kundu 1965). In typical non-flaring conditions on the Sun, the plasma temperatures result in the mildly relativistic version of this process producing gyroresonance emission (White & Kundu 1997). The characteristic motion causes a preferred emission energy related to the oscillation frequency which is mediated by the magnetic field strength (Rybicki & Lightman 1979). For magnetic field strengths found in coronal active regions, this emission occurs in the microwave (Kundu 1965).

Plasma emissions are caused by the bulk motion of the ionized plasma. This can occur both due to continuous wave phenomenon such as bulk ion oscillations and Alfvén waves or due to intermittent impulsive phenomenon such as Cherenkov radiation excited by electron beams accelerated by magnetic reconnection (Kundu 1965). However, these plasma emissions are typically produced as low-frequency radio waves (tens to hundreds of MHz) and quickly dissipate their energy into thermal scales and are therefore transient, impacting coronal emissions only locally and on short timescales (Dulk 1985). Consequently, plasma wave processes are inconsequential for the analysis in this dissertation and are ignored.

1.2.2. The Differential Emission Measure Connection

The corona is (typically) an optically thin plasma, meaning that while it emits light, it does not block emission from background (or lower altitude) sources. Consequently, rather than observing a specific coronal feature, coronal observations detect light from all features along the observed line of sight simultaneously. This has many benefits because it allows for a complete census of coronal plasma (e.g., Vásquez 2016) and for the study of low altitude features beneath overlying structures. However, optically thin media also provide their own challenges, complicating the study of features of interest with contributions from irrelevant underlying sources (e.g., Aschwanden & Boerner 2011; Aschwanden et al. 2013).

A prominent diagnostic of optically thin plasma is the emission measure (EM), the square of the plasma density integrated along the line of sight of the optically thin observation (e.g., Kahler et al. 1970). For the corona, with its complex thermal and magnetic structures, this is typically taken a step further to the differential emission measure (DEM), the EM as a function of temperature (e.g., Craig & Brown 1976). The DEM is directly related to the collisionally induced emission processes described in Chapters 1.2.1 and 2 because the collision frequency (and energy) is controlled by the availability of the two colliding species (density squared) and the particle speeds (determined by the temperature). Consequently, if the DEM is known, the emission from the various collisional processes can be calculated. The DEM, its underlying assumptions, and typical calculation methods are discussed in detail in Chapter 3.

1.3. Significance of $F_{10.7}$

As described in Chapter 1.1, EUV emission from the Sun plays an important role in determining the structure of the Earth's upper atmosphere, which in turn influences satellite operations. But, because EUV is absorbed in the atmosphere it can't be observed from the ground and must be observed from space (Kumar et al. 1974). Additionally, the calibration of EUV instruments is notoriously difficult, and solar observing instruments which are constantly exposed to high EUV fluxes struggle with long term stability (Woods et al. 2012). This means that even with satellites capable of observing in EUV wavelengths, long-term well-calibrated studies of the total solar EUV irradiance are difficult. Consequently, models of the ionosphere-thermosphere typically rely on other measures of solar activity which are easier to observe and calibrate over long periods.

Of particular note is the $F_{10.7}$ index (the solar radio flux at 10.7 cm, 2.8 GHz) that has long been known to correlate with solar EUV emission on time-scales of days and longer (Covington 1948, 1951; Covington et al. 1955; Vats et al. 1998; Foukal 1998; Tapping et al. 2003) and has been measured daily since 1947 (Covington 1969; Tapping 1987). This correlation and the transparency of the atmosphere to microwave signals (Tapping 2013) has led to the use of $F_{10.7}$ as a proxy measurement for solar EUV irradiance. The observed $F_{10.7}$ signal has been used since the beginning of ionosphere-thermosphere modeling (Mathur & Mitra 1960; Paetzold & Zschorner 1961; Harris & Priester 1962; Jacchia 1964; Bhatnagar & Mitra 1966; Jacchia 1971) and remains one of the primary model inputs today, even with the availability of direct EUV observations (Tobiska et al. 2008). $F_{10.7}$ is often preferred over other proxies of solar activity such as Sunspot

Number (SSN), the Mg II core-to-wing index, Lyman-α irradiance, etc. due to its high degree of correlation with solar EUV output which results from the fact that the main variable components of both originate in the same coronal plasma (Swarup et al. 1963) (discussed further in Chapter 2).

Numerous studies have investigated the variability of long duration coronal microwave (primarily $F_{10.7}$) time series for use as proxies of EUV (Covington 1951, 1969; Tapping 1987; Wilson et al. 1987; Lean & Brueckner 1989; Bouwer 1992; Foukal 1998; Parker et al. 1998; Vats et al. 1998; Tobiska et al. 2008; Dudok de Wit et al. 2009; Maruyama 2010; Svalgaard & Hudson 2010; Chen et al. 2011; Johnson 2011; Maruyama 2011; Henney et al. 2012; Deng et al. 2013) and total solar irradiance (TSI, Tapping et al. 2007; Fröhlich 2009; Tapping & Valdés 2011) but there is still considerable debate as to the exact source of the time-variable component. As pointed out in Chapter 1.2.1, both bremsstrahlung and gyroresonance microwave emission are produced in the non-flaring corona. As it happens, $F_{10.7}$ is at a particularly interesting part of the microwave spectrum, where gyroresonance is near its peak contribution (Kundu 1965). However, it is the connection between EUV and microwave bremsstrahlung emission that is most relevant when $F_{10.7}$ is used in models. In this context, the gyroresonance component serves only to distort the relationship between EUV and $F_{10.7}$. Currently, the relative contribution from gyroresonance and bremsstrahlung emission remains an unanswered question. Some studies have argued that the variable microwave component is optically thin bremsstrahlung emission originating from the active regions (Felli et al. 1981; Tapping & DeTracey 1990) while more recent studies suggested that it is primarily gyroresonance emission from the strong magnetic fields above sunspots in active region cores (Schmahl & Kundu 1995,

1998; Dudok de Wit et al. 2014).

1.4. Research Questions

This dissertation attempts to resolve the uncertainty surrounding the source mechanism responsible for the solar $F_{10.7}$ index. This is done by connecting the bremsstrahlung component of $F_{10.7}$ directly to EUV emission using the coronal DEM. Specifically, this work seeks to answer:

1. Can a comparison between the source structure of $F_{10.7}$ and DEMs from EUV images be used to identify gyroresonance emission?

2. What is the variability of the global DEM and the associated coronal thermal properties over a solar cycle?

3. How does the relative contribution of bremsstrahlung and gyroresonance emission in $F_{10.7}$ vary with solar activity?

I give a detailed description of the relevant coronal emission processes in Chapter 2 and describe the physical significance and derivation of the DEM in Chapter 3. The first question is addressed in Chapter 4 by comparing $F_{10.7}$ images taken with the Karl G. Jansky Very Large Array (VLA) with EUV images taken by the Atmospheric Imaging Assembly (AIA). The second question is discussed in Chapter 5 by computing DEMs with over four years of EUV spectral irradiance observations from the Extreme Ultraviolet Variability Experiment (EVE) Multiple EUV Grating Spectrographs (MEGS)-A instrument. The third question is investigated in Chapter 6 by comparing the time series of $F_{10.7}$ with the DEM time series developed in Chapter 5. This research is well timed due to the 2010 launch

of the Solar Dynamics Observatory (SDO) spacecraft (Pesnell et al. 2011) that houses EVE and AIA which are crucial for this study, and the impending commissioning of the Expanded Owens Valley Solar Array (EOVSA) that will perform daily spatially resolved solar observations at 3–18 GHz (Gary et al. 2011).

2. PHYSICS OF CORONAL EMISSION

Accelerating charges produce light. This fundamental concept is the basis for (nearly[1]) all of astrophysics. It is by understanding how the physical parameters of a source translate into particle motion, and therefor the emitted light, that the universe is understood. In the research presented herein, the connections between the physical processes responsible for light emission are central to the data analysis and interpretation. Consequently, it is necessary to provide a basic review of the fundamentals of the relevant emission mechanisms to facilitate a proper understanding of the DEM techniques presented in Chapter 3. A basic background of the relevant physical processes of atomic emission is provided in Chapter 2.1, unbound electron emission is discussed in Chapter 2.2, and the specific relationship between these emission mechanisms in the context of $F_{10.7}$ in the solar corona is described in Chapter 2.3. In this chapter, all information not attributed to a specific reference is drawn from Rybicki & Lightman (1979), the definitive text on astrophysical radiation.

2.1. Atomic Emission

The basic structure of the atom was laid down by Bohr (1913) who unified the experimental structure of the atom from Rutherford (1911) with the quantom

[1]In the modern era, some sub-fields of astrophysics can be studied strictly by observing matter. These include, for example, planetary science (which can sample the ground or atmosphere of a planet), space weather and local interstellar medium investigations (which can directly measure the plasma of interest), and neutrino physics (which can detect individual neutrinos directly). Additionally, we now understand that the vast majority of matter (Oort 1932; Zwicky 1933; Rubin et al. 1978) and energy (Riess et al. 1998; Perlmutter et al. 1999) in the universe is dark, that is, it does not interact electromagnetically. Recent observations of gravitational waves (Abbott et al. 2016b,a, 2017) also demonstrate that certain distant astrophysical phonomena can be observed directly without light.

mechanical understanding of Planck (1900). Bohr's insight, that an electron can only exist with discrete energies such that it "orbits" the nucleus in stationary states that have angular momentum $n\hbar$ (for integer n), revolutionized the understanding of the atom and led to a profusion of discoveries in spectroscopy. A schematic of the Bohr atom is shown in Figure 2.1. Prior to this formulation, it was understood that specific elements displayed unique emission and absorption spectra, e.g. the Hydrogen Lyman (Lyman 1906), Balmer (Balmer 1885), and Paschen (Paschen 1908) series. These could be described mathematically through the Rydberg equation

$$\frac{1}{\lambda} = R\left(\frac{1}{n_1^2} - \frac{1}{n_2^2}\right) \tag{2.1}$$

where λ is the transition wavelength, R is the Rydberg constant ($1.097{\times}10^{-7}$ m^{-1}), and n_1 and n_2 are integers such that $n_2 > n_1 \geq 1$. This accurate mathematical description of atomic emission and absorption was a crucial motivator for Bohr's new physical description of the atom. From his formulation and the physical insight it imparted, Bohr immediately identified emission series that had previously been attributed to Hydrogen as the $n = 3$ (Fowler 1912) and $n = 4$ (Pickering & Fleming 1896; Pickering 1897) based series of singly ionized Helium, He II. The predictive nature of Bohr's theory changed spectroscopy from taxonomy to a probe of the fundamental physics of the universe. It is now understood that atomic energy states are much more complex than those proposed by Bohr (e.g. relating to spin-orbit coupling of the electron magnetic moment and the hyperfine structure caused by the nuclear spin and isotopic mass) and require a fully quantum mechanical treatment, but his simple description is sufficient for the applications presented here.

The emission of light from and absorption of light by an atom is a natural

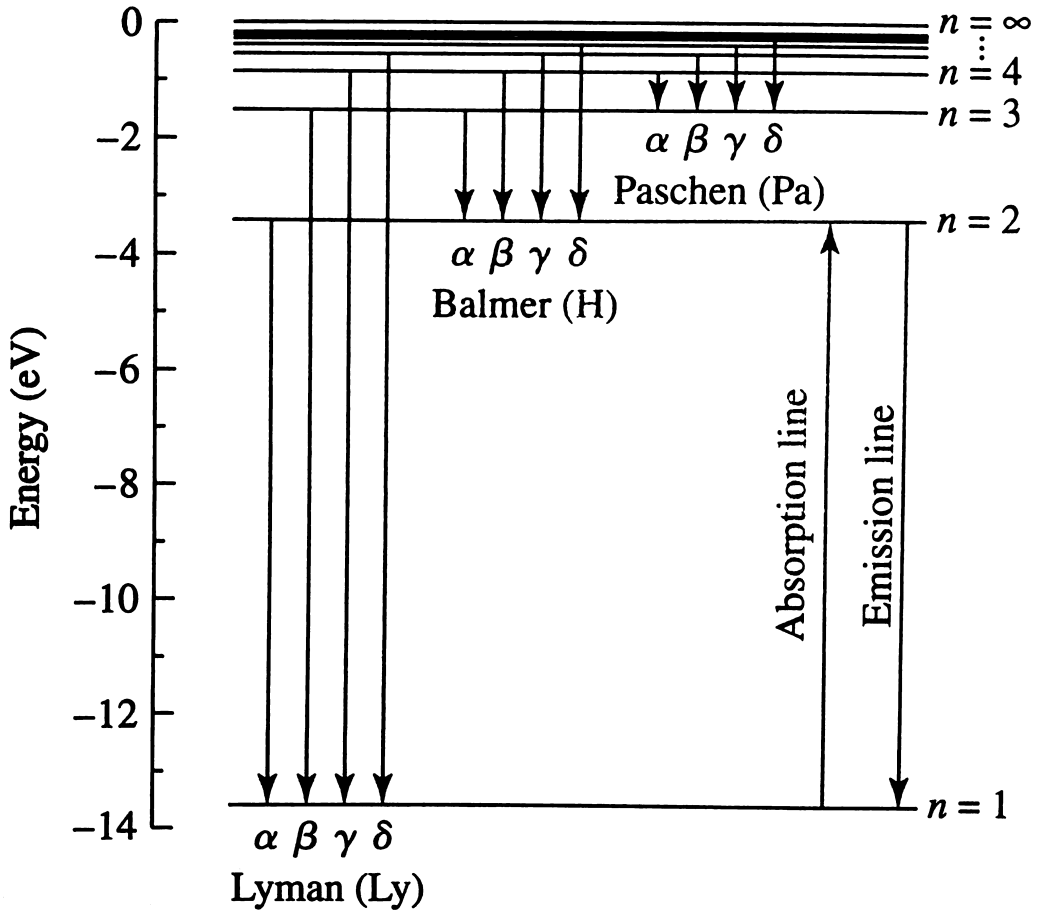

Fig. 2.1.— Schematic of the energy levels described by the Bohr model of a Hydrogen atom. The Lyman, Balmer, and Paschen series are shown along with an indication of the energy and level of each of the electron excitation states. (Carroll & Ostlie 2007)

response to the particle composition of the atom itself. In the simplest case, a hydrogen atom consists of a single proton in the nucleus with an electron in a stable "orbit" surrounding it. This naturally defines a potential energy of the atom based on the separation between the proton and the electron, typically defined by the energy "level" of the electron relative to the proton (Figure 2.1). By interacting with the permeating electromagnetic field, the energy of this system

can increase through absorption or decrease through emission of light, electromagnetic radiation. The energy of the absorbed or emitted photon (quanta of light) is determined by the change in energy of the atom and therefore by the specific energetic properties of the atom.

The rate of emission and absorption of light in a medium is due to a combination of the atomic structure of its constituent matter and the macroscopic environment under consideration. For an individual atom, the available energy states are determined by its intrinsic nature based on the number and relative orientation of its protons, neutrons, and electrons (as well as external factors such as density and magnetic fields that will be ignored for this discussion). The current occupied energy state determines the available transitions that can be achieved. Each individual atomic transition is characterized by three rates: a rate of spontaneous emission (know as the Einstein A-coefficient, the transition probability per unit time), and rates of absorption and stimulated emission that are dependent on the ambient radiation field (and the Einstein B-coefficients which are proportionality constants). These rates for each possible transition describe the radiative properties of each atom, and the overall radiative properties of a system are then determined by the number of atoms occupying each energy state and the background radiation field. For a system in thermodynamic equilibrium, the population of energy levels within a specific ion is governed by the Boltzmann distribution, and the populations of ions of the same atomic species are determined by the Saha equation. Knowledge of the density and temperature of the medium is needed to calculate these absolute populations directly, and these populations coupled with the individual atomic physics of each constituent determine the radiative properties of the medium as a whole.

2.1.1. Bound-bound Emission

In the case of the solar corona, the plasma environment has a high temperature and low density and the system is far from thermal equilibrium. This has significant effects on the nature of coronal atomic emission which is discussed thoroughly in Golub & Pasachoff (2010) Chapter 3.3. The low densities mean that the corona tends to be optically thin to all light with energy greater than microwaves, meaning that photo-absorption is not a relevant factor when determining atomic energy states. Instead, the high temperatures provide particles sufficient kinetic energy to excite and ionize atoms through collisions (typically with electrons that have already been ionized during previous collisions). In the corona, hydrogen and helium are completely ionized and heavier elements such as iron are typically missing between one third and two thirds of their electrons.

The result of these factors is that coronal bound-bound emission proceeds from collisional excitation and emits largely in the EUV portion of the spectrum, although many coronal lines across the electromagnetic spectrum are observed. Notably, emission lines observed in the infra-red (e.g., Münch 1966; Pasachoff & Muzyka 1976) can be used to measure coronal magnetic field strengths (e.g., Tomczyk et al. 2008; Raouafi et al. 2016). The energetic properties of each emission line (including the energy of the transition itself and the ionization stage of the atom) lead to the production of emission lines only when the plasma has temperatures and densities conducive to the production of the line. In this way, individual emission lines probe the state of the coronal plasma. This feature is exploited in the calculation of the DEM which is discussed in detail in Chapter 3.

2.1.2. Free-bound Emission

Atomic emission is also produced when a free electron is captured by an atom into one of its stable energy levels. In this case, because the electron begins unbound and can in principle have any energy, the emission from an individual recombination event produces a photon with energy greater than or equal to the ionization energy of the state into which it is captured. The exact energy is determined by the initial kinetic energy of the captured electron. Due to the interaction cross section of these transitions, free-bound continuum emission goes as ν^{-3} or λ^3 above the ionization energy. This lends the continuum spectrum a saw-tooth quality visible in Figure 2.2 and means that free-bound continua are sharper at higher energies. This recombination typically occurs directly into the ground state of the recombining ion, but when that is not the case, the electron will then usually quickly cascade down to the ground state through bound-bound transitions. This process provides the main source of Hα emission from the upper chromosphere where the majority of hydrogen is ionized (Leenaarts et al. 2012).

There are four free-bound continua in the solar EUV spectrum that are listed in table 2.1. Each of these are visible in the EUV spectrum (Figure 2.2), but the He II edge does not contribute noticeably except during solar flares. During non-flaring times, the He I continuum provides significant emission and the H I continuum dominates the spectrum at 800–912 Å. These free-bound continua are produced in the cooler and denser chromosphere (Milligan et al. 2012) where recombination to these relatively low ionization potential ions (relative to Fe VIII–XVIII commonly found in the corona) is most common.

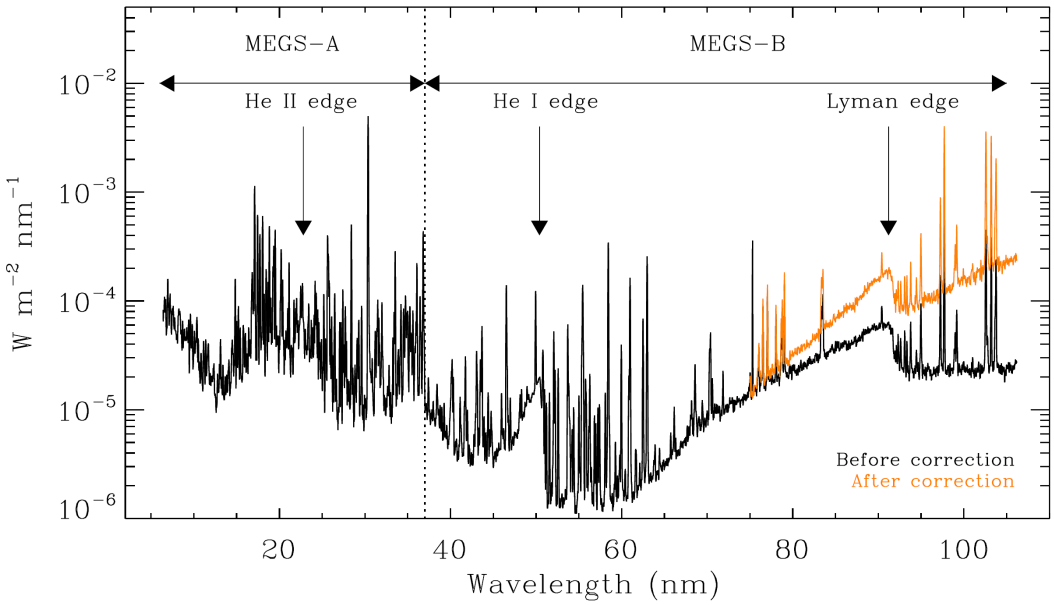

Fig. 2.2.— Complete spectrum from the EVE MEGS-A and MEGS-B spectrographs. Each sharp vertical line in the spectrum is an emission line (or a blend of lines) associated with specific ions and electronic transitions. The hydrogen and helium free-bound continuum edges are identified and the C I continuum is visible at the red edge of the spectrum, although its ionization edge is just beyond the wavelength range of the spectrum. (Milligan et al. 2012)

2.2. Unbound Plasma Emission

Due to the plasma nature of the corona, significant emission is also produced by electrons accelerating unbound from atomic nuclei. This acceleration is caused by the two basic mechanisms connecting charged particles and electromagnetic fields described in the Lorentz force,

$$\mathbf{F} = q\left(\mathbf{E} + \mathbf{v} \times \mathbf{B}\right), \tag{2.2}$$

with the particle charge q, the particle velocity vector $\mathbf{v}$, and the electric and magnetic fields $\mathbf{E}$ and $\mathbf{B}$, respectively (Lorentz 1895). The first term describes the force exerted on a particle by the electric field (often called the Coulomb

force) while the second describes the force exerted on a particle by the magnetic field. Each of the terms in equation 2.2 relates to one of the two unbound particle acceleration mechanisms that produce emission from the non-flaring corona: bremsstrahlung and gyroresonance (Kundu 1965), respectively.

2.2.1. Bremsstrahlung

Thermal bremsstrahlung emission results from the collisional coulomb interaction of electrons and ions (Wild et al. 1963). This is a true continuum emission mechanism that varies as $e^{-\nu/T}$ due to the velocity distribution of the emitting electrons. However, this broadband emission is typically negligible compared to individual emission lines or other continuum emission sources and it is therefore observed primarily in the microwave and X-ray regimes where other emission mechanisms tend to be less dominant. For the work presented herein, only the properties of microwave bremsstrahlung emission are relevant.

Optically thin bremsstrahlung in the radio limit has a flux density (in units of erg cm^{-2} s^{-1} Hz^{-1}) given by

$$f_\nu \;=\; 9.78 \times 10^{-3} \frac{2k_\mathrm{B}}{c^2} \left(1 + 4\frac{N_\mathrm{He}}{N_\mathrm{H}}\right) \int\int T^{-0.5} \mathrm{DEM}(T) G(T)\, \mathrm{d}T\, \mathrm{d}\Omega \qquad (2.3)$$

Table 2.1. EUV free-bound continuum edges (Hock 2012)

Ion	Ionization energy [eV]	Recombination edge wavelength [Å]
He II	54.48	227.6
He I	24.62	503.8
H I	13.61	911.8
C I	11.27	1100.0

where $k_{\rm B} = 1.38 \times 10^{-16}$ g cm^{-2} s^{-2} K^{-1} is Boltzmann's constant, $c = 3 \times 10^{10}$ cm s^{-1} is the speed of light, $N_{\rm He}/N_{\rm H} = 0.085$ (Asplund et al. 2009) is the number (or number density) ratio of Helium to Hydrogen in the emitting medium, T is the temperature in Kelvin, $\mathrm{G}(T) = 24.5 + ln\,(T/\nu)$ is the Gaunt factor where ν is the frequency in Hz, $\mathrm{d}\Omega$ is the solid angle of the source (Dulk 1985) and $\mathrm{DEM}(T)$ is the integral along the line of sight through the corona of $\mathrm{d}(n_e n_{\rm H})/\mathrm{d}T$ discussed in detail in Chapter 3. The dependence of the flux on $n^2\,T^{-0.5}$ means that the optically thin bremsstrahlung flux is actually relatively insensitive to the temperature distribution and is much more sensitive to the plasma density. This means that coronal bremsstrahlung emission is produced primarily in active regions where the plasma density is largest (e.g., Tripathi et al. 2008; Young et al. 2009).

Thermal bremsstrahlung emission at microwave frequencies (1–30 GHz) generally becomes optically thick in the chromosphere because of both the increased density and decreased temperature. The altitude (and therefore temperature and density) at which this optically thick boundary occurs is a strong function of frequency ν since bremsstrahlung opacity varies as $\nu^{-2}\,n^2\,T^{-1.5}$ (Dulk 1985), with higher frequencies penetrating deeper into the chromosphere. This leads to a frequency dependence in the observed height of the solar limb at microwave frequencies, with the apparent size of the solar disk decreasing with increasing frequency (Fürst et al. 1979). In active regions with very high density this optically thick boundary can also occur in the corona at low microwave frequencies, increasing the observed brightness temperature dramatically and blocking observation of the lower atmosphere. It is common for active regions to be optically thick in the corona due to bremsstrahlung at 1.4 GHz but optically thin at 5 GHz (White

1999). Coronal bremsstrahlung emission is generally not strongly polarized, but magnetic fields do break the degeneracy of collisional interactions and produce weak circular polarization (White & Kundu 1997).

2.2.2. Gyroresonance

Gyroresonance emission arises from the acceleration of electrons as they spiral around magnetic field lines. A charged particle moving with a component of its velocity perpendicular to a uniform magnetic field will follow a helical path around the axis of that field with a gyrofrequency of

$$\omega = \frac{qB}{mc} \tag{2.4}$$

where q and m are the charge and mass of the particle, respectively, and B is the magnitude of the magnetic field. At coronal temperatures, even thermal electrons have weakly relativistic velocities and produce opacity not just at the gyrofrequency but also at low order harmonics (Wild et al. 1963). Depending primarily on the magnetic field orientation and the polarization mode, this emission becomes optically thick in the $s = 1,\ 2,\ 3,$ or 4 harmonic of the gyrofrequency

$$\nu_B = 2.80B \quad \text{[MHz]} \tag{2.5}$$

(White & Kundu 1997). This means that $F_{10.7}$ gyroresonance observations at 2.8 GHz come from thin (short path length), optically thick, surfaces with constant magnetic field strengths of $B = 10^3/s = 1000,\ 500,\ 333,$ and 250 G for harmonics $s = 1,\ 2,\ 3,$ and 4 respectively. Because of this magnetic field dependence, gyroresonance emission tends to be very compact, only occurring above sunspots where the magnetic fields are strongest and maintain sufficient field strength in

the corona. The combination of the density and temperature structure of the solar atmosphere with the properties of gyroresonance emission leads to a peaked spectrum with a maximum between 1–5 GHz (e.g. Piddington & Minnett 1951; Kundu 1965; Schmahl & Kundu 1998)

The characteristic motion associated with the gyroresonance process naturally causes the emission to be highly circularly polarized (because any intrinsic linear polarization is wiped out by Faraday rotation in the solar atmosphere). Emission with polarization in the sense of an electron spiraling around the field is called the extraordinary or x-mode, while polarization with the opposite sense of rotation is called the ordinary or o-mode. Electrons couple much more strongly to the x-mode than the o-mode because of the shared sense of rotation. Consequently, the x-mode generally has larger opacity and becomes optically thick in higher (harmonic and altitude) gyroresonant layers. The generally positive temperature gradient in the lower corona means that the x-mode then has a higher brightness temperature causing an observed net circular polarization from gyroresonance sources in the sense of the local x-mode.

2.3. The $F_{10.7}$ Connection

As noted in Chapter 2.1, atomic emission is a complex process. However, assuming the atomic details are known, the EUV emission properties of a bulk plasma in ionization equilibrium are completely determined by the relative elemental abundances and the electron density and temperature distribution, the DEM (Craig & Brown 1976). Similarly, the optically thin coronal microwave bremsstrahlung emission is also determined by the DEM (see Equation 2.3). This

means that bound-bound EUV emission lines and microwave bremsstrahlung emission are connected through the bulk plasma density and temperature. This is the fundamental physics behind the use of $F_{10.7}$ as an EUV proxy.

But, as has been recognized, multiple sources contribute to the observed $F_{10.7}$ flux density. Both bremsstrahlung and gyroresonance emission are produced in the corona, and thermal blackbody emission from the optically thick chromosphere also contributes. However, because both bremsstrahlung and gyroresonance emission are produced predominantly in and around active regions, it can be difficult to separate the two mechanisms both spatially and temporally. To properly compare EUV and $F_{10.7}$, the relative contribution from bremsstrahlung emission sources must be known. Even then, comparison with EUV emission can be complicated by optical depth effects. Coronal EUV emission lines are optically thin all the way down to the optically thick (and non-emitting) chromosphere. In certain circumstances (high density or low observation frequency), bremsstrahlung emission can be optically thick in the corona, and when gyroresonance emission is observed it is always from optically thick layers. This optically thick floor will block all emission from lower altitudes, and if $F_{10.7}$ becomes optically thick in the corona, that means some of the plasma observed in the EUV is hidden from observation in $F_{10.7}$[2]. This complication is addressed specifically in Chapter 4.

[2]It is this optical depth effect and the chromospheric contribution that necessitate using $F_{10.7}$ rather than a lower or higher frequency microwave observation with less gyroresonance emission as an EUV proxy. At lower frequencies the coronal bremsstrahlung becomes optically thick and therefore EUV emission from the low corona in active regions is not properly represented in the microwave. At higher frequencies, the coronal contribution to the signal becomes overwhelmed by the blackbody emission from the chromosphere.

3. THE DIFFERENTIAL EMISSION MEASURE

The emission measure (EM) is defined as

$$\mathrm{EM} = \int_0^l n_e(s) n_{\mathrm{H}}(s)\ \mathrm{d}s, \tag{3.1}$$

where n_e is the electron number density, n_{H} is the hydrogen number density, and l is the path length through the optically thin medium (Greenstein & Minkowski 1953). This formulation arises from the analysis of low-density plasma far from thermal equilibrium (but in statistical equilibrium) when emission is generated primarily through particle collisions. Since the corona is not isothermal, it is conventional to use the differential emission measure (DEM) which represents the column–integrated squared plasma density as a function of temperature such that

$$\mathrm{EM} = \int \mathrm{DEM}(T)\ \mathrm{d}T \tag{3.2}$$

and therefore

$$\mathrm{DEM}(T) = \int \frac{\mathrm{d}}{\mathrm{d}T} n_e(s) n_{\mathrm{H}}(s)\ ds. \tag{3.3}$$

The observed intensity I_λ at wavelength λ is then

$$I_\lambda = \int R_\lambda(T) \mathrm{DEM}(T)\ \mathrm{d}T \tag{3.4}$$

where $R_\lambda(T)$ is the temperature response function of the instrument (Craig & Brown 1976). This response function is dependent on both the technical details of the instrument (wavelength resolution, filter passband shape, detector response, etc.) and the atomic physics of the emitting plasma (composition, transition probabilities, occupation states, temperature sensitivity, etc.). By observing multiple emission lines with different temperature sensitivity (either as spectral lines or through narrow band imaging) it is possible to invert the system of equations

(equation 3.4) to determine the DEM of the source plasma. However, with the addition of measurement errors such as Poisson noise and any instrumental effects, this system becomes under-constrained, and a precise, analytic inversion is impossible. Additionally, even if a self-consistent solution can be found, its relation to the actual emitting plasma is dependent on the atomic parameters in $R_\lambda(T)$ which, in the EUV, may have errors of up to $\sim 50\%$ (Del Zanna et al. 2011).

3.1. Information Content of the DEM

In principle, the DEM contains information about the square of the plasma density as a function of temperature along the integrated optically thin line-of-sight. This provides a thermal understanding of the plasma which can in principle be used to study both plasma heating and cooling (e.g. Reale & Landi 2012; Fletcher et al. 2013; Warren et al. 2013; Caspi et al. 2014) as well as coronal thermal structures (e.g. Aschwanden & Boerner 2011; Del Zanna et al. 2011; Warren et al. 2011; Aschwanden et al. 2013; Petralia et al. 2014), so long as DEMs can be collected in a time series or an image, respectively. Obviously, the DEM only describes the observed plasma that was used to generate it. This statement is trivial, but it does have important practical implications. Most notably for coronal DEMs, even though the chromosphere and transition region plasma are in the line-of-sight of on-disk observations, they are not characterized by DEMs derived from observations sensitive to plasma at coronal temperatures.

Even if the DEM is known and accurately represents the observed plasma, its descriptive power is limited. This is due to a combination of the inability of the observations to characterize the optically thin system and the fundamental

degeneracies inherent in the observations. Often, independent observations can constrain these unknowns, but in their absence, common simplifying assumptions can be made. Since it is the most common technique for calculating coronal DEMs, the following sections describe the calculation of DEMs using EUV atomic emission lines.

3.1.1. Plasma Density

Since the DEM itself represents an integral of the square of plasma density along lines of sight through the solar atmosphere, it does not contain specific information about the density at any point. If the emitting volume is known, the average density (as a function of temperature) can be calculated from the DEM, but due to the optically thin nature of the emission it can be difficult to estimate the emitting volume. Even if the volume is known, the stochastic nature of magnetic processes in the corona (Klimchuk 2015) means there is no guarantee of a uniform density. For example, even for features such as coronal loops that can be approximated as cylinders, non-uniform plasma filling factors can lead to an overestimate of the emitting volume and therefor an underestimate of the true plasma density (Cargill & Klimchuk 2004).

This is particularly problematic because the emission from which the DEM is derived is sensitive to the local plasma density, as well as the EM. As discussed in Chapter 2.1, electronic excitation and a fraction of the de-excitation in the corona is caused by electron–ion collisions whose rate is mediated by the electron density (Gaetz & Salpeter 1983). Therefore, the rates at which individual excitation states within an ion are populated and depopulated are functions of the electron density.

Depending on the details of the excitation and de-excitation pathways for each individual transition, increased density can lead to decreased (through collisional quenching) or increased (through collisional excitation) emission. An example of this effect is shown in Figure 3.1 for a selection of iron EUV emission lines. Different transitions of the same charge state can have different dependencies on density, a property that is exploited for coronal density diagnostics (Tripathi et al. 2008; Warren & Brooks 2009; Young et al. 2009). These considerations break the degeneracy between plasma density and observation path length inherent in the DEM.

The consequence of this density dependence is that the plasma density must be known or assumed to calculate the DEM. However, as discussed above, the density of coronal plasma is non-uniform. In active regions, non-flaring densities can be as high as (3–10)$\times 10^{10}$ cm^{-3} (Tripathi et al. 2008; Young et al. 2009), while in the diffuse quiet corona outside active regions, values as low as (6–25)$\times 10^{7}$ cm^{-3} (Doschek et al. 1997; Warren & Brooks 2009) may be appropriate. This means that high-temperature lines will preferentially originate from higher density active regions while low-temperature lines will dominate the emission from the lower density quiet Sun. For spatially resolved DEMs, the range of densities will tend to be narrower, but even with arbitrary resolution the optically thin nature of the observations means that a DEM will always describe plasma of non-uniform density. Without a formal quantitative basis on which to assign different densities to emission generated from plasma at different temperatures, the DEM is at best a constant density approximation of the true plasma distribution.

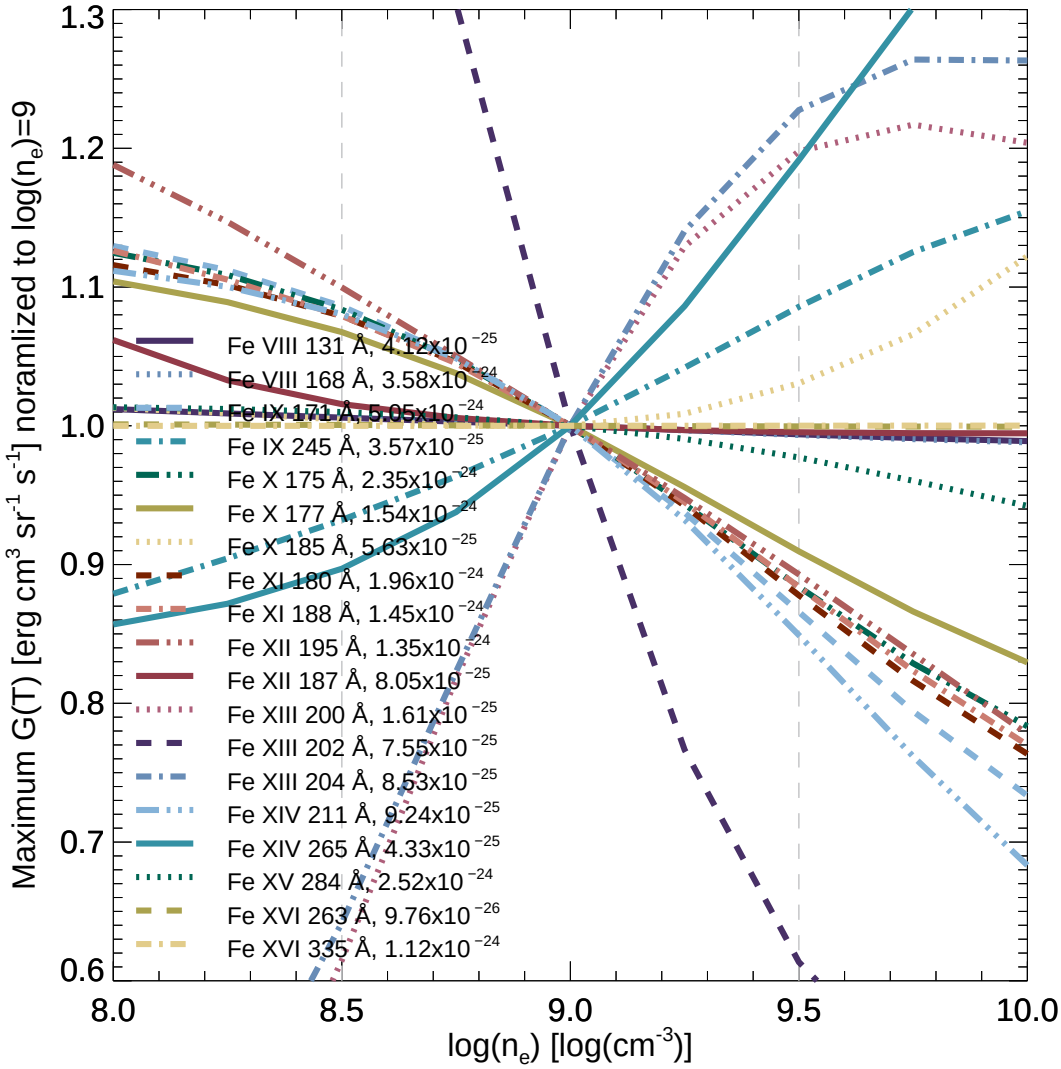

Fig. 3.1.— Relative emission contribution as a function of plasma density for a selection of iron EUV emission lines. This shows the dramatic differences in the density dependence possible for coronal EUV emission lines. Ideally, DEMs should be calculated from emission lines with similar density dependence.

3.1.2. Elemental Abundances

The energetics of the solar corona are dominated by the most populous elements, hydrogen (which is a single proton at coronal temperatures) and helium (an alpha particle). Thus, the emission measure of interest is the total emission

measure, dominated by hydrogen, helium, and the electrons they donate to the plasma. However, H and He do not produce lines in the EUV that are useful for determining coronal DEMs whereas metals, with their higher last electron ionization potentials, emit in numerous suitable lines (e.g. Dere et al. 1997; Del Zanna et al. 2015). This means that DEMs are typically calculated using metal emission lines, and the abundances of those elements relative to hydrogen determine the total DEM. For a DEM determined with single element observations the relationship between the abundance and the DEM is inverse; the greater the abundance of the element the less total plasma is needed to explain a given observed emission. Thus, calculation of the DEM is dependent on accurate knowledge of coronal elemental abundances.

Significant efforts have been made to determine solar elemental abundances both through observations of the solar photosphere and early solar system meteorites (e.g., Asplund et al. 2009, and references therein), but the relationship of these abundances to those found in the corona is not fully understood (e.g. Reames 1999; White et al. 2000; Warren 2014). In particular, the first ionization potential (FIP) effect is an observed enhancement of the coronal abundance of elements with first ionization potential below 10 eV relative to their photospheric levels (Veck & Parkinson 1981; Meyer 1985). Various studies have found the magnitude of this effect to be an enhancement of about four (e.g. Feldman 1992, and references therein), although observations of the time variability of this effect in active regions suggests the effect could be half this canonical value or less (Baker et al. 2015; Brooks et al. 2017).

3.1.3. Optical Depth Effects

One of the primary requirements for the calculation of DEMs is their construction from observed optically thin emission. This is easily satisfied by coronal EUV emission due to the low densities of the emitting species. However, the assumption of optically thin emission is typically not valid for emission in the much cooler and denser chromosphere. In particular, the bright He II 304 Å chromospheric emission line is well documented to become optically thick in active regions (e.g. Cheung et al. 2015; Nuevo et al. 2015) and prominences/filaments (Parenti 2014) and hence cannot be used for DEM analysis. Even though there are numerous EUV emission lines from chromospheric material they are unsuitable for DEM analysis. This restricts the domain over which the DEM is valid and the low temperature DEM remains poorly sampled and typically requires constraints from microwave observations of the quiet Sun (Landi & Chiuderi Drago 2003) where the relationship between optically thin and thick emission can be more tractable.

3.2. DEM Solution Methods

The solution of equation 3.4 for DEM(T) is a classic inversion problem, using a finite number of observations to determine an underlying continuous distribution. In particular, this is an example of a Fredholm equation of the first kind

$$y(\mu) = \int_a^b K(\mu, \nu)\, x(\nu)\, d\nu \tag{3.5}$$

where $K(\mu, \nu)$ is the kernal and a, b, and $y(\mu)$ are known (Craig & Brown 1976). Hadamard (1902) defined problems describing physical systems as well-posed if they satisfy:

1. a solution exists,

2. the solution is unique, and

3. the solution is continuous with the initial conditions.

Any problem that does not satisfy these three conditions is termed ill-posed and tends to require complex numerical techniques and further assumptions to reach a solution. For the case of the DEM, condition 1 is always satisfied. However, due to unavoidable measurement errors, there is no guarantee that a set of noisy observations represents the true underlying DEM. This complication can typically be overcome simply by acknowledging some level of uncertainty in the results, and improvements in instrument characterization and performance minimizes these effects. In general, a finite number of observations cannot uniquely constrain a continuous distribution, and therefore condition 2 is not met. If the underlying DEM is assumed to be discrete with a number of temperature bins equal to the number of (linearly independent) observations (a condition that is obviously never satisfied but might approximate reality) then this does guarantee a unique solution. The final condition is the most problematic as the complex relationship between a given observation and the underlying DEM can lead to highly unstable solutions. In particular, the more sharply peaked the kernal functions ($R_\lambda(T)$ in equation 3.4), the more stable the solution. For a more complete discussion of these issues and a complete description of the difficulties associated with DEM calculation see Craig & Brown (1976).

This all necessitates the use of complex numerical techniques to calculate the underlying DEM from a set of EUV observations. Examples are described in the following sections for the two most prominent sets of methods, Markov chain

Monte Carlo (MCMC) simulations and inversion techniques. Unfortunately, no solution technique is perfect (hence their proliferation) and different methods will often yield markedly different solutions for the same set of observations. Because of this, it is particularly important that a DEM solution method provides (at least an estimate of) the error in the results. This both provides confidence in the level of physical interpretation that can be made from a DEM and allows comparison between different solution methods.

Certain safe assumptions can be made with all solution techniques that simplify the set of possible solutions and ensure physically meaningful results. The first restriction is in fact physically required, that the DEM have no negative components. Negative DEM components are common in various solution methods as the addition and subtraction of emission is numerically equivalent. Of course, the physical interpretation of negative DEM components is absurd, either negative plasma density or negative path length (or volume). Another common restriction is one relating to the smoothness of the solution. This is motivated by an understanding that the heating and cooling processes in the corona are multithermal (Klimchuk 2006) and have no mechanism to accumulate (or remove) plasma in narrow temperature ranges.

3.2.1. MCMC

Monte Carlo (Metropolis & Ulam 1949) solution techniques were originally developed to study those systems that are too complex for an analytic solution but also too small to be properly explained by the methods of statistical mechanics. The basic principle of the technique is simple: by testing the parameter space of

possible inputs, the approximate solution to a problem can be reached statistically based on the probability of the outputs. For example, the original application of the problem was to determine the probability of winning a game of "solitaire", a game utilizing a full deck of cards that is far too complex for an analytic, combinatorial solution, but also deterministic, such that the outcome of the game is determined by the initial card ordering. Using the Monte Carlo approach to determine the probability of winning involves "playing" a large number ($\sim 10^4$) of games with random initial conditions. With a large enough sample size (i.e. sufficiently complete coverage of the input parameter space) the probability of victory with the tested initial conditions approaches the probability with random initial conditions.

The same basic principle can be applied to study physical systems as long as the inputs and outputs are related analytically. In such cases, the usual desire is to determine the correct (or most probable) set of parameters to explain a set of observations. This is possible using properties of stochastic and memory-less computation systems originally clarrified by Markov (1906). Markov showed that a series of events determined uniquely by the current state of the system (i.e. the next step is determined completely from the current step, with no reference to any previous steps) subject to some convergence forcing will tend towards a single solution (as described in Metropolis et al. 1953) independent of the initial conditions of the series. A so-called Markov chain is thus a way to evolve a guess at the solution of a complex problem towards the true solution. In application, this involves setting an initial set of inputs to a calculable system, evaluating how these inputs reproduce an observable output, modifying the inputs based on the quality of agreement between the calculation and the observable, and repeating

until the result becomes stable and has good agreement with the observable. This process is usually performed as part of a Markov chain Monte Carlo (MCMC) implementation where many Markov chains are calculated from a Monte Carlo initial random sampling of the parameter space. This process tends to produce robust results (because it thoroughly samples the input parameter space) at the cost of computational efficiency (by performing numerous repetitive calculations).

3.2.1.1. PINTofALE MCMC techniques are applied to the DEM solution problem in the Package for Interactive Analysis of Line Emission (PINTofALE, Kashyap & Drake 2000) for the solution of coronal DEMs based on observed optically thin EUV and X-ray spectra. PINTofALE is a large package used to analyze spectra by connecting observations with the atomic physics of the emitting lines, but its centerpiece is its MCMC DEM calculation (Kashyap & Drake 1998). This samples the parameter space of possible DEMs (i.e. the amount of plasma in each temperature bin) by solving for observable intensities with equation 3.4 and iterating the DEM until it can explain the observed intensities. At each step, a Bayesian probability of the output fluxes given the observations determines if that realization moves the solution towards or away from the true DEM. Rather than adopting an arbitrary smoothness constraint, this method uses the temperature resolution of the input lines (i.e. the observations) to determine a set of Gaussian basis functions that are tuned in the MCMC process to determine the observed DEM. Another benefit of this kind of MCMC calculation is a robust and stable solution that naturally characterizes the error in the resulting DEM. The thoroughness of this solution comes at the cost of computation time, requiring seconds to minutes to calculate a single DEM on modern computers.

3.2.1.2. Warren et al. (2017) Another more recent method presented by Warren et al. (2017) uses a more nuanced implementation of the general MCMC method based on a sparse Bayesian approach. Instead of dynamic basis functions they instead use Gaussian basis functions spaced regularly in log(T) space but prefer solutions utilizing the minimum number of basis functions by utilizing a Cauchy (Lorentz) distribution for the prior probability of the basis function weights. Additionally, they use a more complex methodology of the general MCMC framework by calculating multiple Markov chains in parallel and updating the chains in pairs. However, this complexity is costly, taking ∼45 minutes to compute a single DEM.

3.2.2. Inversions

As described above, the DEM calculation satisfies the conditions of a classic ill-posed inversion problem. For any practical solution the DEM must be discretized and therefore equation 3.4 can be recast as a set of linear equations

$$\mathbf{I}_\lambda = \mathbf{R}_\lambda \mathbf{DEM} \tag{3.6}$$

where $\mathbf{I}_\lambda$ is a vector of observed intensities, $\mathbf{R}_\lambda$ is a matrix of the temperature response functions of the observed lines or filters, and **DEM** is the DEM vector. If $\mathbf{R}_\lambda$ is square (i.e. the DEM is discretized into a number of bins equal to the number of observations) then the DEM can in principle be computed using a direct inversion

$$\mathbf{DEM} = \mathbf{R}_\lambda^{-1} \mathbf{I}_\lambda. \tag{3.7}$$

However, such direct methods tend to be unstable and often produce solutions with unphysical negative DEM components. This is due to both observational

noise and fundamental uncertainties in the calculation of $\mathbf{R}_\lambda$. To overcome these limitations, numerous numerical techniques can be introduced to ensure more stability against measurement errors and require physically meaningful solutions. Another direct benefit of these solution schemes is the ability to compute DEMs with finer temperature resolution than is possible through a direct inversion. The primary reason these methods are often preferred over MCMC solutions is their speed, computing DEMs in (sometimes very small) fractions of a second. It is due to this speed advantage that these inversion techniques are utilized for the DEM calculations described in Chapters 4 and 5.

3.2.2.1. Hannah & Kontar (2012) DEMs are calculated in Hannah & Kontar (2012) using a regularized inversion method that utilizes Generalized Singular Value Decomposition (SVD) that is able to return estimates of the error in both the DEM and the temperature bins. The regularization involves a constraint of the DEM solution which allows for a solution despite observational uncertainties. However, the presence of these uncertainties (and solutions with more parameters than observational constraints) mean that there are infinite possible solutions that are consistent with the data (within some χ^2 goodness of fit threshold). The default zero order regularization constraint biases towards solutions with the minimum total EM, but higher order regularization schemes that bias towards solutions with the minimum temperature variation (i.e. narrow DEMs) are also possible. The method uses a two step process where an initial solution with weak regularization (i.e. an under-constrained solution) is used in the calculation of the final, properly constrained DEM. This method can also guarantee positive solutions at the cost of reduced χ^2 agreement with the observations. Finally, this

method is reasonably efficient, typically computing DEMs in less than a second, although including numerous observations can increase the computation time to a few seconds. This method is used to compute the spectroscopically determined DEMs in Chapter 5

3.2.2.2. Plowman et al. (2013) The method developed by Plowman et al. (2013) uses a hybrid approach to compute regularized inversion DEMs. They begin by computing the direct inversion (equation 3.7) using the squared-normalized instrument response functions as the basis functions of the inversion. They find that this choice of basis functions produces a result identical to an SVD with a large number of narrow basis functions and thus satisfies a minimum squared EM constraint (similar to the minimum total EM constraint in Hannah & Kontar (2012)). While this does not enforce positive solutions, it will tend to prefer them since negative EM will require more positive EM to balance it, leading to higher EM^2. To enforce positivity, they then perform an iterative correction process, modifying the DEM until it is strictly positive while maintaining agreement with the observations to within the desired χ^2 level. This regularization step requires that the DEM be re-sampled using regularly gridded basis functions (they use triangle functions spaced equally in log(T) space) instead of the instrument response functions. Finally, if this process fails to converge within a set number of iterations, the process is repeated with two weaker levels of regularization (solutions allowing more deviation from the observations) until a suitable solution is found. Only if all three regularization strengths fail to converge to a strictly positive solution are any negative EM components allowed to remain in the final solution. The primary benefit of this method is its speed, computing hundreds

to thousands of DEMs per second. This method is used to compute the DEM images in Chapter 4

3.2.2.3. Cheung et al. (2015) Similar to the method of Warren et al. (2017), Cheung et al. (2015) developed a solution method based on sparsity. Like the other inversion methods mentioned above, their implementation of a DEM inversion involves minimizing the total emission measure while constrained to the observations (within the observational error) and requires non-negative DEMs. This formulation lends itself to solution using the simplex algorithm (Dantzig et al. 1955) which is implemented as a native IDL function. The fundamental difference between this technique and those described before is the weight given to a particular solution. In the previous inversion methods, the techniques preferred solutions that matched the input data exactly, so long as the result satisfied the positivity and regularization constraints. In Cheung et al. (2015), the method prefers the solution with the minimum total EM, so long as it agrees with the observations to within the noise level. This acknowledges that all solutions within the observation errors should be given equal weight and therefore chooses the true minimum EM solution. This could in theory lead to systematic underestimation of the true DEM, but in practice the solutions cluster around the true distribution just like any other method. One downside of this method is the possibility of failure. If there is no positive solution within the observational constraints, this method fails to compute a result. This can be avoided by successively increasing the allowed error (similar to the successive iterations at different regularization levels applied by Plowman et al. (2013)) until a solution is found. Due to the simplicity of the mathematics involved in this formulation of the problem this

technique is extremely fast, solving $\sim 10^5$ DEMs per second.

3.3. The CHIANTI Atomic Line Database

Inherent in any calculation of the DEM is a reliance on the known atomic physics responsible for the observed emission. In the EUV, the premier reference for atomic line emission is the CHIANTI database (Dere et al. 1997) currently on release version 8.0.9 (Del Zanna et al. 2015). This database includes the atomic physics necessary to study optically thin plasma dominated by collisional excitation from the X-ray through the infra-red (although the database was originally designed for the soft X-ray and EUV 50–1100 Å). It includes both experimental and theoretical results for hundreds of ions including their energy structures, emission wavelengths, radiative rates, collision strengths, and electron excitation rates. This results in thousands of individual emission lines originating from plasma with temperatures of log(T)=4.5–8.0. Additionally, the database includes numerous IDL routines designed to facilitate the analysis of observational data, from spectral reconstruction to DEM fitting. These allow for tuning of the elemental abundances and ionization equilibrium calculations, and continuum emission processes are also included so that an observed spectrum can be self consistently analyzed completely within the CHIANTI database framework.

4. IMAGING $F_{10.7}$

The first space based coronal imaging was in the X-ray where sounding rockets imaged the Sun first with pinhole cameras (Blake et al. 1963) and then with grazing incidence optics (Giacconi et al. 1965). Continuous imaging of the solar corona began in earnest during the 1973–1974 Skylab mission when the eight instruments of the Apollo Telescope Mount observed the Sun from the visible to the X-ray, with five operating in the EUV and X-ray (Eddy & Ise 1979). This 9 month nearly continuous monitoring of the corona paved the way for numerous future spacecraft[1]. There are currently numerous coronal observing satellite missions including the Solar and Heliospheric Observatory (SOHO, Domingo et al. 1995), the Reuven Ramaty High-Energy Solar Spectroscopic Imager (RHESSI, Lin et al. 2002), and the Solar Dynamics Observatory (SDO, Pesnell et al. 2011), just to name a few.

The relatively young field of radio astronomy began with the Jansky (1933) discovery and Reber (1940) confirmation of a radio source at the galactic center. After World War II, physicists and engineers turned many of the wartime radar receivers to the sky leading to an explosion of discoveries in the new field of radio astronomy (Greenstein 1984). The first radio observations of the Sun were performed by Reber (1944) and Southworth (1945), although radio noise from the Sun was detected and considered an important military secret during World War II (Hey 1946). These initial investigations were performed using a single antenna or dish and provided little (if any) spatial resolution of the Sun. Today, the Siberian Solar Radio-Telescope (14.6 GHz Smolkov et al. 1986; Grechnev et al. 2003) and

[1]For a brief history of X-ray telescopes see Giacconi (2009)

the Nobeyama Radioheliograph (17 and 34 GHz, NoRH, Nakajima et al. 1994) make daily microwave images of the solar atmosphere. The Expanded Owens Valley Solar Array (EOVSA) in California is being commissioned, and it will soon image the Sun daily at 3–18 GHz (Gary et al. 2011). A similar instrument, the Chinese Spectral Radioheliograph (CSRH), is also under development and will image the Sun daily at 0.4–15 GHz (Yan et al. 2009).

As early as Kundu (1959) it was understood that solar thermal microwave sources could be split into three classes: a low intensity background originating from the quiet Sun (Martyn 1948), a moderate intensity signal seen in and around active regions (Covington 1947), and a high intensity component commonly associated with active region cores (Piddington & Minnett 1951). The background component (here taken to be 65.2 ± 2.0 sfu of the $F_{10.7}$ flux) can be explained with a uniform optically thick chromosphere of $11,000$ K and an overlying optically thin 10^6 K corona (Zirin et al. 1991), which is generally removed for the purposes of EUV approximation (but see also Landi & Chiuderi Drago 2003, 2008).

The ambiguity in the source of the $F_{10.7}$ variability (discussed in Chapter 1.3) is best resolved through imaging when the individual sources are resolved. Many such studies have been performed throughout the microwave regime, both of the entire solar disk (Swarup et al. 1963; Bastian & Dulk 1988; Gopalswamy et al. 1991; Tapping et al. 2003) and of individual active regions (Felli et al. 1981; White et al. 1992). There has been less work specifically at 2.8 GHz, and the best prior imaging was that of Saint-Hilaire et al. (2012) who used the Allen Telescope Array to observe the full Sun between 1.43 and 6 GHz (including $F_{10.7}$). They used the emission spectra and polarization to identify gyroresonance sources with a spatial resolution at 2.8 GHz of about $1'$. However, due to a lack of available

instrumentation, imaging of $F_{10.7}$ with resolution better than one arcminute did not become possible until the upgrade to the Karl G. Jansky Very Large Array (VLA). Selhorst et al. (2014) recently completed a study of the statistical properties of spatially resolved active regions observed at 17 GHz in order to identify bremsstrahlung and gyroresonance emission and noted that a similar analysis is needed to fully understand $F_{10.7}$. While high-resolution radio studies are necessary to identify gyroresonance regions and their contribution to $F_{10.7}$, they are not in general sufficient to determine the magnitude of the gyroresonance emission (White & Kundu 1997) and some independent estimate of one of the components of the radio signal is required.

The bremsstrahlung component of the flux can be extrapolated without direct radio observation if the DEM is known. As discussed in Chapter 3, DEMs can be calculated from sets of optically thin observations, including EUV imaging and spectroscopy, as long as they are sensitive to a range of coronal temperatures wide enough to sample the dominant coronal plasma. However, the fundamental problem remains the same for any optically thin observation and Landi & Chiuderi Drago (2003, 2008) constructed solar-minimum DEMs using both EUV and radio observations to constrain the plasma structure from the chromosphere all the way through the corona. More commonly, comparisons can be made between radio observations and the predicted bremsstrahlung component based on DEMs computed from EUV images, e.g., by White et al. (2000) and Zhang et al. (2001). If the abundance is known (as discussed in Chapter 3.1.2), then the DEM can be used to predict the optically thin bremsstrahlung emission from the plasma observed in the EUV. White et al. (2000) used this technique to measure the Fe abundance in an active region.

Below is described analysis of the first full-disk image of $F_{10.7}$ emission acquired with the VLA, which was the highest spatial resolution 2.8 GHz image ever taken at the time, and its comparison with spatially-resolved EUV images. The prediction of the bremsstrahlung emission along with the polarization signal in the radio are used to identify gyroresonance sources in the radio image and determine the total gyroresonance component of the $F_{10.7}$ flux. This work was published in Schonfeld et al. (2015).

4.1. Imaging Data

The observations for this analysis were taken during the rising phase of solar cycle 24 on 2011 December 9, between 15 and 23 UT. During this period there was moderate solar activity on the earthward hemisphere and the $F_{10.7}$ index was 143.5 ± 1.2 sfu (Tapping & Charrois 1994), but there were no recorded solar storms of any kind. The observed variability of coronal features was insignificant and occurred mostly on scales below the resolution of the radio observations.

4.1.1. Very Large Array

At the time of these observations, the Karl G. Jansky Very Large Array (VLA, operated by the National Radio Astronomy Observatory, NRAO) was in the process of being upgraded, and data were taken as a shared-risk project. As such, only 17 of the VLA's nominal 27 available antennae were equipped with the "S-band" feeds ($2 - 4$ GHz) needed to observe $F_{10.7}$. The VLA was in its most compact ("D") array configuration, appropriate for recovering the flux of large-scale sources in the solar atmosphere. The reduced number of antennae

decreased the resulting image quality significantly, because of both the reduced coverage of the u-v plane, as well as the 37% decrease in collecting area. For this analysis, eight 2 MHz channels centered on 2.783 GHz were summed for a total bandwidth of 16 MHz. Solar observations in S-band are taken with the additional nominally-20 dB attenuators in the signal path and these add phase changes that are corrected using independently measured values of the delays (Bin Chen, private communication). Unfortunately, the measurements of the primary flux calibration source were corrupted, preventing independent measurement of the amplitude changes due to the attenuators. Consequently, the solar fluxes were calibrated assuming exactly 20 dB of attenuation and a nominal flux for the secondary calibrator. We estimate that the VLA solar fluxes therefore have an uncertainty of order 20%.

The field of view of a single VLA pointing with the S-band receivers is nominally $15'$ and therefore mosaicking is required to image the entire $30'$ diameter solar disk. A honeycomb pattern mosaic was used, with a single pointing at disk center surrounded by six fields designed to overlap by half a beam width. The center of each field was tracked over the course of the eight hour observation, taking into account solar differential rotation. This led to some slight feature smearing near the edges of each field, but the magnitude was well below the final $25''$ resolution of the observation and there appeared to be no effect on the final mosaic image. Each field was calibrated separately and then the fields were imaged jointly in a single map using maximum entropy deconvolution. The images were restored with a spatial resolution of $25''$. Due to the limited field of view, as well as the restriction caused by the minimum baseline, the observations were insensitive to emission on the scale of the solar disk. Attempts to restore this

component using a default disk of the right dimension in the deconvolution process were unsuccessful (because they failed to produce a mostly flat disk as seen in the Allen Telescope Array observation of Saint-Hilaire et al. 2012), and we therefore do not address the spatial distribution of the large-scale emission here. This large-scale component will be analyzed with a subsequent data set acquired using more antennae and a larger mosaic pattern.

4.1.2. Nobeyama Radioheliograph

The 17 GHz data from the NoRH (Nakajima et al. 1994) were used to assess optical depth effects in the bremsstrahlung radio emission (the optical depth of bremsstrahlung at 17 GHz is 37 times smaller than at 2.8 GHz) and as a calibration check. NoRH makes full disk images of the Sun at 17 and 34 GHz every day between 23:00 and 06:30 UT. Located in Japan, the dedicated solar array is unable to observe simultaneously with the VLA, and therefore the Nobeyama images collected just after the completion of the VLA observation were used. The data were mapped and calibrated using standard procedures: amplitude calibration assumed that the background disk component that generally dominates the total flux had a brightness temperature of 10^4 K, which is known to be consistent with well-calibrated flux monitoring at this frequency by the Nobeyama Radio Polarimeters (NoRP; Nakajima et al. 1985). The magnetic field dependence of equation 2.4 means that 17 GHz is only sensitive to gyroresonance emission from strong magnetic fields, requiring a coronal field greater than 2000 G to observe the third harmonic. Coronal magnetic field strengths this high are typically only seen in the case of very large active regions. Given the absence of such regions during the observation, the Nobeyama observations are expected to detect purely

bremsstrahlung emission from the solar atmosphere that is excess to the (chromospheric) background brightness temperature level of 10^4 K. The 17 GHz image was made by synthesizing and deconvolving data taken at 45 s intervals over a period of several hours, and rotating the final image back in time to match the VLA image. The spatial resolution in the final 17 GHz image is $12''$, and the flat background disk of 10^4 K (with a radius 1.0125 times the photospheric radius that fits the 17 GHz visibilities) is subtracted for the region analysis.

4.1.3. Atmospheric Imaging Assembly

The full disk EUV images used for this analysis came from the Atmospheric Imaging Assembly (AIA) (Lemen et al. 2012) aboard the Solar Dynamics Observatory satellite. All six coronal EUV channels (94 Å, 131 Å, 171 Å, 193 Å, 211 Å, and 335 Å) were used at one minute cadence over the course of the VLA observation. The point spread function corrections from Poduval et al. (2013) were applied to the level 1.5 images which were then summed after rotation to a common time at the midpoint of the VLA observation to produce longer integrations and increase the signal to noise. The blurring created by small scale feature fluctuations during this long integration had no effect on the results because the bremsstrahlung prediction resulting from the EUV data was convolved with a $25''$ Gaussian beam before analysis to match the resolution of the radio observations. The EUV image sequence was also used to check for any time variability that might affect the results (Figure 4.1). No major time variability is present and therefore the time-integrated EUV data is appropriate for comparison with the 8-hour VLA data set.

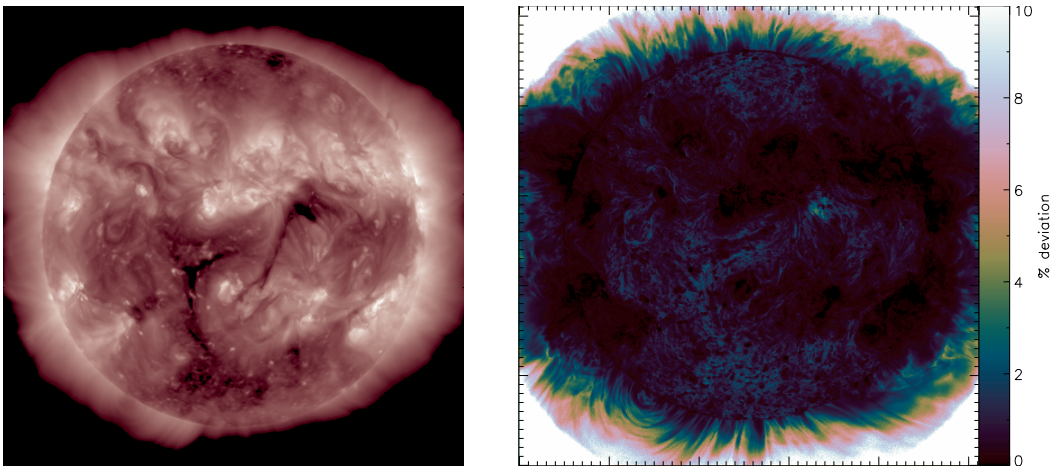

Fig. 4.1.— Full disk solar images of *left:* the eight hour integrated 211 Å AIA image and *right:* the standard deviation of each pixel in the 211 Å image time series plotted as a percentage of the observed flux. Notice that the on-disk variation is small, especially in active regions which have high signal to noise.

4.1.4. Helioseismic and Magnetic Imager

Photospheric line-of-sight magnetic field measurements were obtained by the Helioseismic and Magnetic Imager (HMI) (Scherrer et al. 2011) on the Solar Dynamics Observatory. These 4096 × 4096 low-noise full sun magnetic field maps are produced every 5 minutes (Schou et al. 2011), but only the single observation closest to 19:00 UT (the central time of the VLA observation) was used because, like the corona, the photosphere showed very little variability during the observation window. While radio and EUV observations are sensitive to the corona and chromosphere which lie megameters above the photosphere, strong photospheric magnetic fields indicate large active regions which extend into the corona where gyroresonance emission should be the strongest. HMI magnetograms are used to qualitatively connect radio polarization measurements to the coronal magnetic field.

4.2. Full-Sun DEMs from AIA Images

The DEMs were calculated using the inversion method presented in Plowman et al. (2013) described in Chapter 3.2.2 that can compute a full resolution AIA (4096×4096 pixels) DEM image in about one hour on a single processor workstation. The AIA images used here are dominated by the lines of Fe VIII, IX, XII, XIV, XVIII, and XXI, which together cover the temperature range $\log(T) = 5.6 - 7.0$ corresponding to the bulk of coronal plasma. The AIA response functions were calculated using the CHIANTI 7.1.3 package (Landi et al. 2013) assuming coronal abundances (Feldman 1992) and the CHIANTI default ionization balance (Boerner et al. 2012).

Full disk representations of the calculated DEMs are shown in Figure 4.2. The left image shows the total emission measure which is obtained by integrating the DEM in each pixel over the temperature axis. This EM dominates the contribution to the final bremsstrahlung prediction because it is linear in the integral in equation 2.3 and has over two orders of magnitude variation on the solar disk. On the right is an image of the emission-measure-weighted median temperature calculated from the derived full disk DEM. This map shows some small discontinuities along the east and north limb (which appear saturated in the image) but these regions play no role in the analysis as described in Chapter 4.3. The temperature impacts the bremsstrahlung emission as $T^{-0.5}$ (Dulk 1985) in the integral over temperature (Equation 2.3), and, because the median temperature varies by only half an order of magnitude across the solar disk, the temperature variation plays a relatively minor role in the predicted radio fluxes compared to the emission measure.

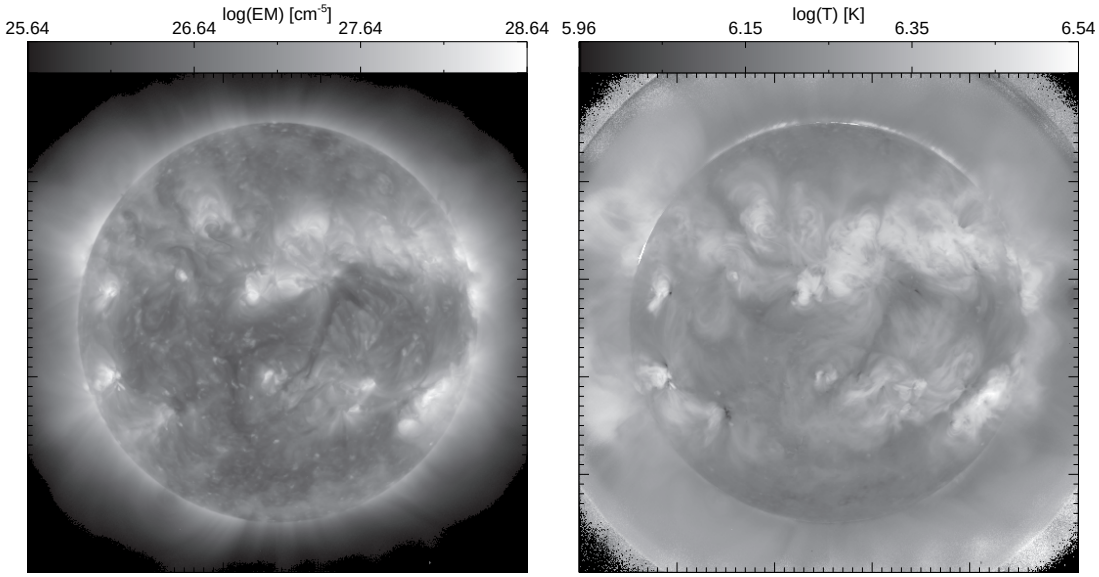

Fig. 4.2.— Full disk solar images of *left:* the total emission measure and *right:* the emission-measure-weighted median temperature as calculated from the AIA images. The apparent static and black patches in the corners of the temperature image are due to vignetting of the AIA detectors where no signal is detected.

4.3. Analysis

An image of the expected coronal component of the bremsstrahlung emission is calculated using the DEMs computed from the AIA images and equation 2.3, assuming a coronal abundance for Fe discussed in Chapter 4.4.2. This image is computed at the full AIA resolution and then convolved with a 25″ full width half maximum Gaussian and down-binned to match the resolution of the radio observations. The brightness temperature of the bremsstrahlung prediction and radio observation are shown in Figure 4.3 on the same scale, with individual regions outlined and labelled. Notice that while the overall morphologies agree quite well, the observation has large, high temperature emission peaks from the centers of many of the regions which are absent from the bremsstrahlung prediction. Additionally, the bremsstrahlung prediction has significantly more faint emission surrounding the active regions than is observed. It is important to emphasize that

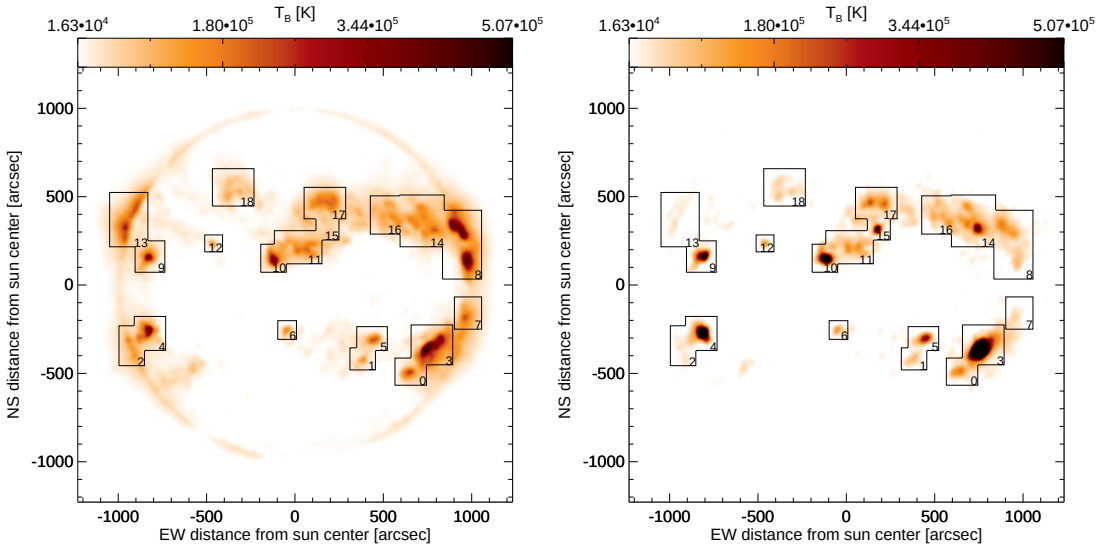

Fig. 4.3.— Full disk solar images on the same brightness temperature scale of *left:* the optically thin bremsstrahlung prediction and *right:* the 2.783 GHz observation. Individually analyzed regions are boxed and numbered.

the prediction image is based on the AIA observations and therefore it will vary from the observed optically thin bremsstrahlung wherever the EUV is sensitive to different plasma than the radio.

The average $F_{10.7}$ flux measured by the official Solar Monitoring Program in Penticton, Canada, at 18, 20, and 22 UT on 2011 December 9 is 143.5 ± 1.2 sfu. Subtracting the quiet sun background of 67.2 ± 2.1 sfu (the 65.2 ± 2.0 sfu constant solar minimum level scaled to a Sun-Earth separation of 0.985 AU) leaves an observed variable $F_{10.7}$ component of 76.3 ± 2.4 sfu. The total $F_{10.7}$ flux from the predicted bremsstrahlung image is 77.7 ± 0.1 sfu, which compares well with the observed variable flux. This suggests that gyroresonance emission is not distorting the $F_{10.7}$ flux significantly since the optically thin bremsstrahlung component can account for all of the variable $F_{10.7}$ on this day. However, this conclusion ignores several complicating details which are discussed in Chapter 4.4.

4.3.1. Region Comparison

The full disk images in Figure 4.3 cannot be compared quantitatively because of the failure to restore the flat background disk (which is in any case absent from the EUV images) to the $F_{10.7}$ radio image. Instead, individual regions on the Sun for which the imaging is reliable are analyzed. The bremsstrahlung prediction, radio intensity, circular polarization, and photospheric line-of-sight magnetic field strength in each region are compared in order to determine if gyroresonance emission is present. These comparisons for the regions with the largest observed polarizations are shown in Figure 4.4. In region 3, the general morphologies of the observed and predicted active regions agree very well despite the much higher observed radio brightness temperature than predicted by the EUV data. Additionally, the circular polarization signal is large above the strong photospheric magnetic fields, as expected. The remaining three regions shown in the figure each display varying levels of morphological deviation between the bremsstrahlung prediction and radio observation, suggesting that there are gyroresonance sources offset from the peak bremsstrahlung emission (because optical depth effects in the bremsstrahlung sources will not produce offsets). In region 4, the peak observed emission is shifted to the southwest by about $20''$, aligning with the observed polarization signal. The observation of region 10 extends east and west farther than the predicted emission, aligning with the polarization signal directly above the east-west oriented photospheric magnetic fields. Region 15 shows a strongly polarized radio source above an isolated sunspot with no corresponding predicted bremsstrahlung source. These regions show that the VLA resolution is sufficient to extract active region details in both the intensity and the individual polarization channels, allowing for the identification of large gyroresonance sources simply

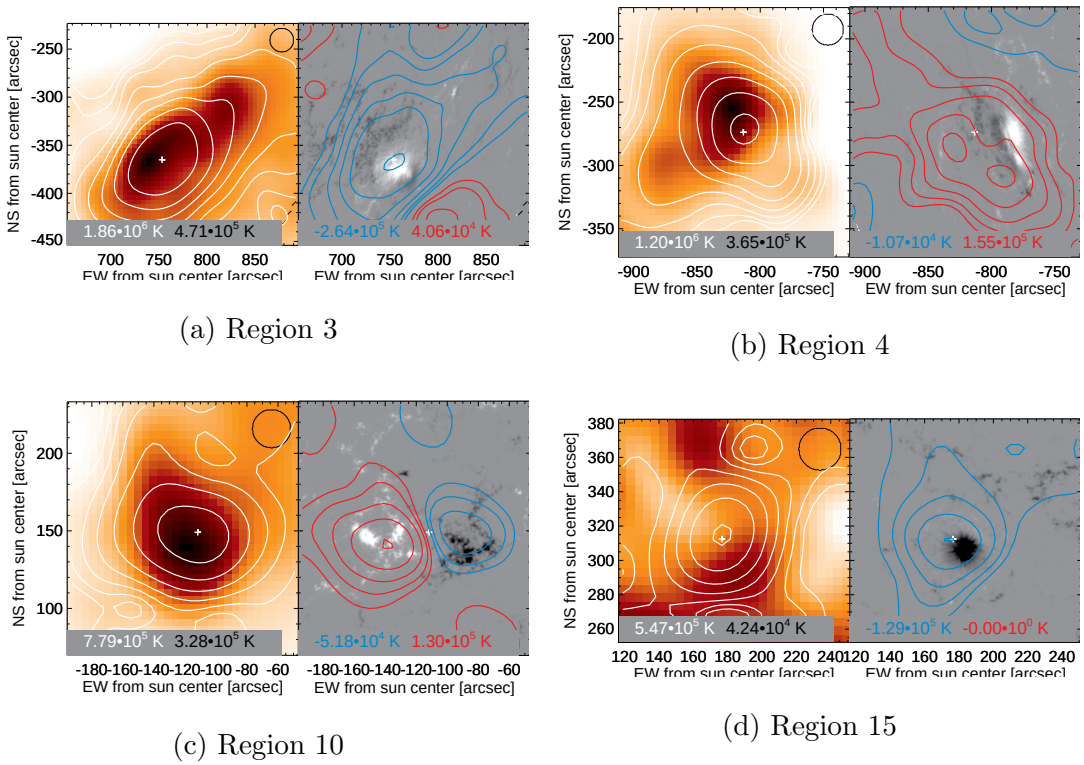

(a) Region 3

(b) Region 4

(c) Region 10

(d) Region 15

Fig. 4.4.— Individual regions of interest which each have a peak polarization brightness temperature greater than 10^5 K. The left pane shows the bremsstrahlung prediction as an inverted heat map with the radio intensity overplotted with white contours at $(8, 16, 32, 64, 128, 256, 512, 1024) \times 10^3$ K. The right pane shows the photospheric line-of-sight magnetic field in gray scale with the radio polarization brightness plotted with contours (blue for left hand polarization and red for right hand polarization) at $\pm(8, 16, 32, 64, 128, 256, 512) \times 10^3$ K. The small black circle in the top right corner of the left pane is the approximate beam size and the white plus signs mark the location of peak observed radio intensity. The left pane also lists the peak brightness temperature of the radio observation (white) and the bremsstrahlung prediction (black) while the right pane lists the minimum (left hand) and maximum (right hand) polarization brightness temperatures.

from the polarization and morphological inconsistencies.

In order to isolate the active region fluxes from any larger-scale background, identical background-subtraction approaches are used in both the bremsstrahlung prediction and the radio observation to allow quantitative comparison between the data sets. This involves using the solar disk around the border of each region

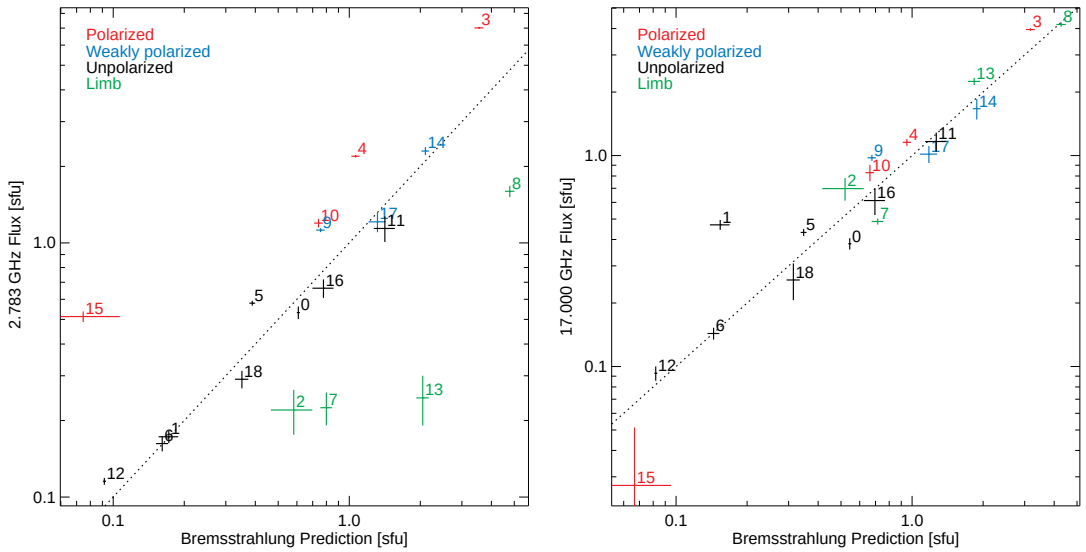

Fig. 4.5.— Total flux observed in each region at *left:* 2.783 GHz and *right:* 17 GHz is plotted against the total predicted optically thin bremsstrahlung emission. The dotted lines indicate where the bremsstrahlung prediction equals the observed flux. Regions that lie above the line have more observed flux than is predicted, suggesting gyroresonance emission. Regions that lie below the line are non-physical and indicate more predicted optically thin bremsstrahlung emission than the total observed flux. Regions labelled in red have peak polarization brightness temperatures of $T_B \geq 10^5$K, blue regions have $5 \times 10^4 \leq T_B \leq 10^5$K, black regions have $T_B \leq 5 \times 10^4$K, and green regions lie above the solar limb.

to estimate the disk emission within the region itself. This is done for concentric borders up to $3'$ outside each region, using the average result to calculate the region flux and the variation in the total region flux as a measure of the uncertainty. Note that while these uncertainties are quoted for the remainder of the paper, the systematic uncertainties associated with the DEM calculation and the uncertainty in the VLA flux calibration may be much larger (as discussed in §4.4.3). The flux from each region is plotted in Figure 4.5 where the regions have been classified based on their maximum polarization brightness temperature and their proximity to the solar limb.

The peak circular polarization brightness temperature is emphasized rather

than degree of polarization because the effective noise level in the latter is very high. This is due to both the noise level in Stokes I and V and the inability to fully restore the disk emission in total intensity which greatly affects the low intensity regions. In addition, the large beam size at 2.8 GHz results in smearing between any smaller gyroresonance sources and the more extended bremsstrahlung emission. In some cases (notably region 10), oppositely polarized gyroresonance sources overlap within the 25″ beam size and cancel, resulting in artificially low polarization. All the regions with strong circular polarization show degrees of polarization greater than 30%, but this is likely an underestimate.

4.4. Discussion

A dramatic feature of Figure 4.3 is that the EUV-predicted radio fluxes of the regions at the solar limb are all well in excess of their counterparts in the radio image. This effect can also be seen in the left panel of Figure 4.5 where the limb regions are plotted as green points which all lie in the non-physical regime. The total predicted bremsstrahlung flux from the limb regions is 8.2 ± 0.3 sfu whereas only 2.3 ± 0.1 sfu is observed. Correcting for this 5.9 ± 0.3 sfu difference in the limb flux (i.e. subtracting it from the total 77.7 ± 0.1 sfu bremsstrahlung prediction) suggests that there should be 71.8 ± 0.3 sfu of optically thin coronal bremsstrahlung in the $F_{10.7}$ signal. Comparison to the observed 76.3 ± 2.4 sfu variable component now suggests the presence of a small amount of gyroresonance emission. Note that this is a conservative correction for the discrepancy at the limb because it does not account for any of the limb emission outside the main active regions.

The chromosphere provides the optically thick background for both the ra-

dio and EUV observations and therefore sets the height of the visible solar limb, however this height is frequency dependent. The effective solar limb at 2.8 GHz is around 30″ above the solar photosphere (Gary 1996), while the height of the effective solar limb at EUV wavelengths is only a few arcseconds above the photosphere (Auchère et al. 1998; Zhang et al. 1998). It is believed that the extra height of the radio limb is due to cool filamentary chromospheric material (such as spicules) that extends into the solar corona and can provide extra opacity at the limb. We interpret the depressed radio signal from the limb regions as the occultation of emission originating behind the chromospheric limb. This has interesting implications for $F_{10.7}$ as an EUV proxy because the difference in limb altitude may cause the obscuration of a significant fraction of the solar emission in the radio which is visible in the EUV. In this case, plasma that produces at least $7.7 \pm 0.5\%$ of the variable $F_{10.7}$ component and that is visible in EUV is not observed in the radio. Not only does this complicate comparison of $F_{10.7}$ and EUV fluxes, it can also cause an offset in time-series comparisons because EUV sources will become visible before corresponding $F_{10.7}$ sources rotate into view, and will remain visible after $F_{10.7}$ sources rotate behind the limb. This effect is explored in detail in Chapter 6.1.1.

4.4.1. Individual Regions

Bremsstrahlung emission is usually weakly polarized while gyroresonance sources are often strongly polarized, therefore those regions that have highly polarized emission are suspected gyroresonance sources. In Figure 4.5 the observed regions are categorized based on the peak polarization brightness temperature. Regions with a peak polarization brightness temperature $T_B \geq 10^5$ K at 2.783 GHz

are deemed to have strong polarization and all lie well above the bremsstrahlung line, therefore confirming that they have significant gyroresonance contribution. Regions with $5 \times 10^4 \leq T_B \leq 10^5$ K are classified as weakly polarized, possibly containing gyroresonance sources, while regions with $T_B \leq 5 \times 10^4$ K are deemed to be insufficiently polarized and are unlikely to contain significant gyroresonance sources. These weakly polarized and unpolarized regions all have fluxes very close to the bremsstrahlung predictions, with only two (regions 5 and 9) showing significant observed radio excess. The total radio excess which is interpreted as the gyroresonance contribution (although this could also be due in part to the bremsstrahlung becoming optically thick) is 5.6 ± 0.2 sfu in the regions with strong polarization, 0.3 ± 0.2 sfu in the weakly polarized regions, and 0.3 ± 0.2 sfu in the unpolarized regions. More than 60% of the total gyroresonance emission originates in region 3, the largest disk active region.

This analysis suggests that 6.2 ± 0.3 sfu or $8.1 \pm 0.5\%$ of the variable $F_{10.7}$ signal recorded on 2011 December 9 results from gyroresonance emission. While this is a small percentage it is well above the precision of the Penticton $F_{10.7}$ measurements and could be sufficient to account for the known $\sim 10\%$ density errors resulting from $F_{10.7}$ driven thermosphere models (Bowman et al. 2008). It is important to note that this gyroresonance emission, if it is constant (or even a constant fraction of the variable component), would have little impact on the use of $F_{10.7}$ as an EUV proxy. However, since the gyroresonance contribution is dominated by the largest active region, we speculate that it is likely to be a much larger fraction of $F_{10.7}$ at times of high solar activity and this could affect the use of $F_{10.7}$ as an EUV proxy.

4.4.2. Coronal Iron Abundance

A straightforward result of this analysis is confirmation that the iron abundance in the corona is $N_{\rm Fe}/N_{\rm H} = 1.26 \times 10^{-4}$, an enhancement of about a factor of 4 over the photospheric value. Two independent results that depend on the coronal value of $N_{\rm Fe}/N_{\rm H}$ confirm this conclusion: the total bremsstrahlung flux derived from the AIA data matches the coronal contribution to $F_{10.7}$ derived by subtracting the solar minimum flux from the measured $F_{10.7}$ flux during the observation; and the fluxes of the 17 GHz active regions, which are known to be well calibrated by matching the NoRH full-disk flux to the calibrated NoRP patrol measurement, are consistent with the predictions from AIA data. The inferred DEM of H, to which the predicted bremsstrahlung radio flux is proportional, depends inversely on the assumed iron abundance: if $N_{\rm Fe}/N_{\rm H}$ were to be photospheric, the $F_{10.7}$ prediction based on the AIA data for this day would be $67.2 + (4 * 77.7) = 378$ sfu, rather than the measured 143.5 ± 1.2 sfu. These results are consistent with White et al. (2000) who found an iron abundance of $N_{\rm Fe}/N_{\rm H} = 1.56 \times 10^{-4}$ with approximate 20% errors by comparing radio observations with bremsstrahlung predictions from EUV DEMs in a single active region. Note that the assumption that the solar minimum flux has no significant coronal contribution disagrees with the model of Zirin et al. (1991), but Landi & Chiuderi Drago (2003, 2008) carried out a careful comparison of the solar minimum radio spectrum with a DEM derived from UV and EUV data and in their results the $F_{10.7}$ solar minimum flux has only a small coronal contribution. This is discussed further in Chapter 6.3.2.

Features other than coronal emission from active regions, including flares (which may be dominated by evaporated chromospheric material) and energetic

particles, have shown different abundances, ranging from 1.2 (Meyer 1985) to 13.1 (Reames 1999) times the photospheric level. These results suggest that an iron enhancement of 4 is generally appropriate for coronal active regions, although we address this further in Chapter 6.4.1.

4.4.3. Uncertainties

It should again be noted that the systematic uncertainties involved in this analysis are much greater than the statistical errors quoted above. Systematics such as the iron abundance and improper calibration of the VLA 20 dB attenuators cause constant offsets and therefore affect the overall agreement of the disk fluxes (although this does not apply to the well-calibrated 17 GHz data). The effects of these constant offsets is minimized by normalizing each region to the local disk background as described in Chapter 4.3. However, based on the errors in coronal abundance studies as well as differences between the flux observed with the VLA and the official record measured at Penticton, we expect both of these error sources to be on the order of 20%.

Uncertainties in the DEM solutions could have spatially variable errors depending on the underlying plasma parameters. These errors are expected to be on the order of 10% or less but it is difficult to quantify the extent to which deviations between the derived DEM and the ground truth plasma parameters change the results due to the non-linear influence of the DEM on the bremsstrahlung prediction. However, the comparison of the bremsstrahlung prediction to the 17 GHz Nobeyama observation in Figure 4.5 shows no clear correlation of deviation with active region size. This suggests that there is no systematic bias and that

any pixel scale statistical errors in the DEM are washed out when integrating over an entire active region.

No attempt is made to account for the underestimation of gyroresonance emission because of the predicted bremsstrahlung emission originating from below the optically thick gyroresonance layer. If the most extreme case is assumed, that all of the observed radio emission from the strongly polarized regions results from gyroresonance emission (i.e., all of the predicted bremsstrahlung emission occurs below the optically thick gyroresonance layer), then the total gyroresonance flux from these regions would be 10.9 ± 0.1 sfu. This is a generous upper limit which, while it does allow a possible factor of two difference in the gyroresonance flux, still restricts the total gyroresonance to less than 15% of the variable $F_{10.7}$ component.

4.5. Results

Understanding the sources of the solar $F_{10.7}$ flux is important if it is to be used reliably as an EUV proxy in thermosphere/ionosphere models. By comparing a full disk VLA observation with the $F_{10.7}$ bremsstrahlung emission predicted from DEMs calculated with AIA images, $8.1 \pm 0.5\%$ of the variable $F_{10.7}$ flux on 2011 December 9 can be attributed to the gyroresonance mechanism. This gyroresonance contribution does not directly correlate with solar EUV flux and therefore should be removed from $F_{10.7}$ when it is used as an EUV proxy. While this is a small fraction of the $F_{10.7}$ signal, it is commensurate with the density errors in current ionospheric modeling efforts.

Unexpected occultation due to the optically thick chromosphere of $F_{10.7}$ flux originating from behind the solar limb is also identified. It appears that this

effect could cause systematic errors in $F_{10.7}$ time series at the active region scale (on the order of 10 sfu) over one day time scales. This effect is not commonly considered as a possible complication when comparing $F_{10.7}$ to EUV emission. For this observation, the on-disk gyroresonance excess (6.2 ± 0.3 sfu) almost perfectly cancels the off disk paucity (minimum of 5.9 ± 0.3 sfu). There is no reason for these two effects to be correlated except in the general sense that both are likely to vary with the general level of activity, and consequently it seems unlikely that they will generally offset each other as well as they do here.

The details of these results depend strongly on the coronal iron abundance which is inherent in the calculation of the DEM. Comparing the bremsstrahlung prediction with the Nobeyama 17 GHz images and the coronal contribution to the $F_{10.7}$ measurement confirms a coronal iron abundance of $N_{\mathrm{Fe}}/N_{\mathrm{H}} = 1.26 \times 10^{-4}$ (the standard coronal abundance in the CHIANTI database; Dere et al. 1997; Landi et al. 2013) which is used in the calculation of AIA temperature response functions. These results are subject to various potential systematic error sources which are difficult to quantify, but have estimated accuracies on the order of 20%.

No general statements about the effects of gyroresonance and limb corrections on the $F_{10.7}$ index can be made from this observation because a single measurement is insufficient to characterize their temporal variability. These questions are addressed in detail in Chapter 6. Additionally, based on the untested systematic biases from the VLA calibration complications and the confusion regarding the altitude of optically thick gyroresonance layers, caution should be taken when considering these results.

5. DEMS OF THE SLOWLY VARYING CORONA

As described in Chapter 1, the solar corona (the outer layer of the Sun's atmosphere) plays an important role in solar activity and the Sun's impact on the Earth's atmosphere. The high (million degree kelvin) temperatures found in the corona result from a still unidentified (but likely magnetic field dominated, e.g., Zirker 1993; Walsh & Ireland 2003; Klimchuk 2006) heating mechanism that must be a fundamental process, since it is known to occur across a wide range of stellar types. The distribution of energy with temperature in the corona presumably reflects the nature of this mechanism and the way that energy is redistributed through the corona from the locations where heat is deposited. It is through the DEM (described in detail in Chapter 3) that the thermal structure of the corona is studied.

The *Solar Dynamics Observatory* (*SDO*), launched in 2010 (Pesnell et al. 2011), has led to greatly improved understanding of the solar corona, including determination of coronal DEMs with both images at several EUV passbands from the Atmospheric Imaging Assembly (AIA; Lemen et al. 2012) and spectral irradiance measurements from the EUV Variability Experiment (EVE; Woods et al. 2012). This has been accomplished for studies of solar flares (e.g., Hock 2012; Fletcher et al. 2013; Kennedy et al. 2013; Warren et al. 2013; Caspi et al. 2014; Warren 2014; Zhu et al. 2016), active regions (e.g., Warren et al. 2012; Aschwanden et al. 2013; Del Zanna 2013; Petralia et al. 2014), coronal loops (e.g., Aschwanden & Boerner 2011; Del Zanna et al. 2011; Warren et al. 2011), the full Sun (e.g., Nuevo et al. 2015, , and Chapter 4), and even the entire corona over a complete Carrington rotation (Vásquez 2016). Major advances provided by *SDO* include

consistent, high temporal resolution, long-term, full-Sun observations.

Here is described a study of the long-term coronal DEM variability leveraging the uniform EVE spectral data set over a significant fraction of the solar cycle. Considering the corona in such a holistic sense provides perspectives lost in narrowly focused active region studies. EVE spectra are particularly well suited to this task because extra effort has been made to provide in-flight calibration thanks to sounding rocket under-flights with an identical instrument (Hock et al. 2010). Additionally, the ability to identify individual emission lines in EVE spectra allows for the selection of diagnostics representing a wide range of coronal conditions. This work was published in Schonfeld et al. (2017)

5.1. EVE MEGS-A Coronal Spectra

EVE includes a suite of instruments designed to observe the solar EUV irradiance from 1 to 1050 Å with high cadence, spectral resolution, and accuracy. Within this suite, the Multiple EUV Grating Spectrographs (MEGS)-A grazing-incidence spectrograph observed the solar irradiance over the wavelength range 50–370 Å with better than 1 Å resolution and greater than 25% irradiance accuracy (Woods et al. 2012). MEGS-A operated nearly continuously from 2010 April 30 until 2014 May 26, when it suffered a CCD failure (Pesnell 2014). There were four CCD bake-out procedures during this period when no data were collected[1].

This study uses the MEGS-A spectra collected every day between 19:00 and

[1]Bake-outs occurred in the periods 2010 June 16–18, 2010 September 23–27, 2012 March 12–13, and 2012 March 19–20.

20:59 UT[2] to compute a representative "daily" spectrum. In practice, the median in each 0.2 Å MEGS-A wavelength bin over the 2 hr period (comprising 720 spectra taken at 10 s intervals) is used to create a median spectrum. Use of the median minimizes the effects of short-timescale variability, including flares, during the observation window. Long-duration flares will still perturb the median values. No attempt is made to remove such events, or global coronal changes on hour-long timescales, from the spectra because they are considered important aspects of the long-term coronal evolution. All of the analysis is performed using these daily median spectra.

As an example of typical daily median MEGS-A data, Figure 5.1 shows the EVE spectrum in the wavelength range 165–215 Å, which contains a large number of strong coronal emission lines. Important to note here is that the resolution of the EVE spectra does not resolve the intrinsic width of the coronal lines. The typical full-width at half-maximum (FWHM) of lines measured in the MEGS-A spectra is ~ 0.75 Å (although the instrument line width was found to be ~ 0.85 Å by Hock et al. 2012), while the actual intrinsic line widths are of order 0.1 Å (Feldman & Behring 1974). Nonetheless, strong coronal lines such as those labeled in Figure 5.1 are usually clearly visible in the spectra. Version 8.0.2 of the CHIANTI atomic line database (Dere et al. 1997; Del Zanna et al. 2015) is used for line identification.

In order to generate accurate and consistent DEMs from MEGS-A spectra, a list of suitable candidate lines is identified, i.e. strong features in the spectra believed to be dominated by individual spectral lines. For the purpose of deriving

[2]This interval is chosen to match the timing of the daily $F_{10.7}$ measurement at 20 UT.

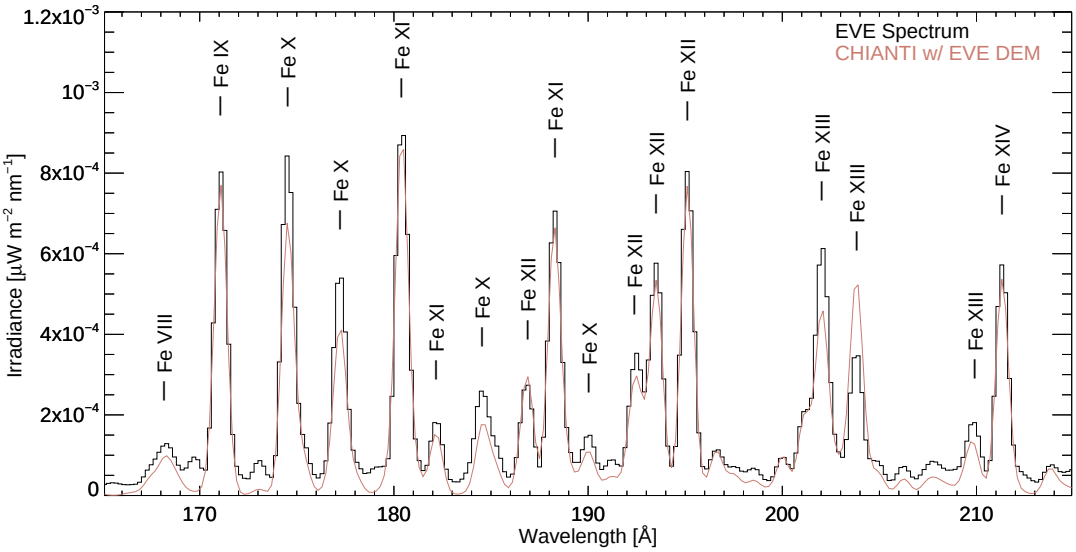

Fig. 5.1.— Portion of the observed EVE spectrum on 2011 November 6 (black histogram) along with the CHIANTI model spectrum (red line) calculated using the DEM computed as described in Chapter 5.2. The CHIANTI lines have been convolved with a 0.75 Å FWHM Gaussian to generate the model spectrum. This rich region of the spectrum contains many strong emission lines from Fe VIII – XIV that originate in the corona. Note that the synthetic CHIANTI spectrum is believed to lack a large number of weak unresolved lines that appear in the EVE spectra as an offset, which partly explains why some of the lines appear stronger in the EVE spectrum than in the CHIANTI spectrum.

a complete census of coronal emission as a function of temperature, lines covering the broadest possible temperature range above about 0.3 MK are required. In view of the lingering debate surrounding coronal abundances in relation to the first ionization potential (FIP) effect (Feldman 1992; White et al. 2000; Asplund et al. 2009), the analysis is restricted to Fe emission lines (most of the strong lines in the MEGS-A spectra) in order to minimize the number of elemental abundances required for the calculations. Further details regarding the effects of elemental abundance are discussed in Chapter 5.2.3.

MEGS-A spectra contain strong lines for all Fe charge states in the range VIII – XVI, as well as XVIII. The peak temperatures of the responses of this

set of Fe charge states cover the range 0.6–7.1 MK, i.e., they sample the bulk of the non-flaring corona. The list of strong, relatively isolated MEGS-A emission features dominated by the emission from a single stage of Fe, with their primary contributing transitions, peak temperature, and relative strength determined from CHIANTI, is given in Table 5.1. For each line the features blended within the FWHM of the target transition are also identified. All of the EVE features are almost pure Fe emission, with the exception of Fe XVI 335 Å which has a significant Mg VIII line 0.15 Å blueward of the primary line.

To extract the flux of each primary line, the emission features in the median daily spectra are fit with three Gaussian functions (four in the case of Fe XVIII), one at the primary wavelength and one each in the red and blue wings to account for the flux from neighboring emission features. The wavelength, width, and strength of each Gaussian component are allowed to vary in the fitting process, although the allowed wavelength range is constrained in some cases (notably for Fe VIII 168 Å), and the width of the wing features is constrained to the width of the primary feature when the wings lack identifiable peaks. A characteristic set of line fits are shown in Figure 5.2. For each line the observed flux is taken as the integrated flux in the primary Gaussian, with the exception of the Fe VIII 168 Å feature, which is actually a complex of six Fe VIII lines. For Fe VIII 168 Å the flux in the blue-wing Gaussian is added to the flux in the primary line since the wing is also dominated by Fe VIII emission. The uncertainties in the fitted fluxes are determined from the uncertainties in the line amplitude and width found during the fitting procedure.

The line fits also include a constant background component. This is included to account for weak lines that are not included in the CHIANTI database but

Table 5.1. Analyzed EUV mission lines

Ion	Wavelength Å	Peak $\log(T)$	Relative $G(T)$	Lower State	Upper State
Fe VIII	131.2400	5.75	2.372×10^{-25} 0.047	$3s^2\ 3p^6\ 3d\ ^2D_{5/2}$	$3s^2\ 3p^6\ 4f\ ^2F_{7/2}$
Fe VIII	130.9410	5.75	0.668	$3s^2\ 3p^6\ 3d\ ^2D_{3/2}$	$3s^2\ 3p^6\ 4f\ ^2F_{5/2}$
Fe VIII	*168.1720*	5.75	1.315×10^{-24} 0.260	$3s^2\ 3p^6\ 3d\ ^2D_{5/2}$	$3s^2\ 3p^5\ 3d^2\ ^2D_{5/2}$
Fe VIII	167.4860	5.75	0.626	$3s^2\ 3p^6\ 3d\ ^2D_{3/2}$	$3s^2\ 3p^5\ 3d^2\ ^2D_{3/2}$
Fe VIII	167.6540	5.75	0.060	$3s^2\ 3p^6\ 3d\ ^2D_{3/2}$	$3s^2\ 3p^5\ 3d^2\ ^2D_{5/2}$
Fe VIII	168.0030	5.75	0.051	$3s^2\ 3p^6\ 3d\ ^2D_{5/2}$	$3s^2\ 3p^5\ 3d^2\ ^2D_{3/2}$
Fe VIII	168.5440	5.75	0.599	$3s^2\ 3p^6\ 3d\ ^2D_{5/2}$	$3s^2\ 3p^5\ 3d^2\ ^2P_{3/2}$
Fe VIII	168.9290	5.75	0.312	$3s^2\ 3p^6\ 3d\ ^2D_{3/2}$	$3s^2\ 3p^5\ 3d^2\ ^2P_{1/2}$
Fe IX	*171.0730*	5.95	5.048×10^{-24} 1.000	$3s^2\ 3p^6\ ^1S_0$	$3s^2\ 3p^5\ 3d\ ^1P_1$
Fe X	174.5310	6.05	2.348×10^{-24} 0.465	$3s^2\ 3p^5\ ^2P_{3/2}$	$3s^2\ 3p^4\ 3d\ ^2D_{5/2}$
Fe XI	*180.4010*	6.15	1.760×10^{-24} 0.349	$3s^2\ 3p^4\ ^3P_2$	$3s^2\ 3p^3\ 3d\ ^3D_3$
Fe X	180.4410	6.05	0.106	$3s^2\ 3p^5\ ^2P_{1/2}$	$3s^2\ 3p^4\ 3d\ ^2P_{1/2}$
Fe XI	188.2160	6.15	8.619×10^{-25} 0.171	$3s^2\ 3p^4\ ^3P_2$	$3s^2\ 3p^3\ 3d\ ^3P_2$
Fe XI	188.2990	6.15	0.602	$3s^2\ 3p^4\ ^3P_2$	$3s^2\ 3p^3\ 3d\ ^1P_1$
Fe IX	188.4930	5.95	0.277	$3s^2\ 3p^5\ 3d\ ^3F_4$	$3s^2\ 3p^4\ 3d^2\ ^3G_5$
Fe XII	*195.1190*	6.20	1.298×10^{-24} 0.257	$3s^2\ 3p^3\ ^4S_{3/2}$	$3s^2\ 3p^2\ 3d\ ^4P_{5/2}$
Fe XIII	202.0440	6.25	6.936×10^{-25} 0.137	$3s^2\ 3p^2\ ^3P_0$	$3s^2\ 3p\ 3d\ ^3P_1$
Fe XI	201.7340	6.15	0.091	$3s^2\ 3p^4\ ^1D_2$	$3s^2\ 3p^3\ 3d\ ^3S_1$
Fe XI	202.4240	6.15	0.097	$3s^2\ 3p^4\ ^3P_2$	$3s^2\ 3p^3\ 3d\ ^3P_2$
Fe XIII	203.8260	6.25	5.251×10^{-25} 0.104	$3s^2\ 3p^2\ ^3P_2$	$3s^2\ 3p\ 3d\ ^3D_3$
Fe XII	203.7280	6.20	0.201	$3s^2\ 3p^3\ ^2D_{5/2}$	$3s^2\ 3p^2\ 3d\ ^2D_{5/2}$
Fe XIII	203.7950	6.25	0.402	$3s^2\ 3p^2\ ^3P_2$	$3s^2\ 3p\ 3d\ ^3D_2$
Fe XIII	204.2620	6.25	0.125	$3s^2\ 3p^2\ ^3P_1$	$3s^2\ 3p\ 3d\ ^1D_2$

Table 5.1 (continued)

Ion	Wavelength Å	Peak $\log(T)$	Relative $G(T)$	Lower State	Upper State
Fe XIV	*211.3172*	6.30	9.191×10^{-25} 0.182	$3s^2\ 3p\ ^2P_{1/2}$	$3s^2\ 3d\ ^2D_{3/2}$
Fe XV	284.1630	6.35	2.518×10^{-24} 0.499	$3s^2\ ^1S_0$	$3s\ 3p\ ^1P_1$
Fe XVI	*335.4090*	6.45	1.123×10^{-24} 0.222	$3s\ ^2S_{1/2}$	$3p\ ^2P_{3/2}$
Mg VIII	335.2530	5.90	0.122	$2s^2\ 2p\ ^2P_{1/2}$	$2s\ 2p^2\ ^2S_{1/2}$
Fe XVIII	93.9322	6.85	1.436×10^{-25} 0.028	$2s^2\ 2p^5\ ^2P_{3/2}$	$2s\ 2p^6\ ^2S_{1/2}$
Fe VIII	93.4690	5.80	0.068	$3s^2\ 3p^6\ 3d\ ^2D_{3/2}$	$3s^2\ 3p^6\ 7f\ ^2F_{5/2}$
Fe XIV	93.6145	6.30	0.177	$3s^2\ 3d\ ^2D_{3/2}$	$3s^2\ 4p\ ^2P_{1/2}$
Fe VIII	93.6160	5.80	0.102	$3s^2\ 3p^6\ 3d\ ^2D_{5/2}$	$3s^2\ 3p^6\ 7f\ ^2F_{7/2}$
Fe XX	93.7811	7.00	0.064	$2s^2\ 2p^3\ ^2D_{5/2}$	$2s\ 2p^4\ ^2P_{3/2}$
Fe X	94.0120	6.05	0.292	$3s^2\ 3p^5\ ^2P_{3/2}$	$3s^2\ 3p^4\ 4s\ ^2D_{5/2}$

Note. — Emission lines identified for analysis in EVE MEGS-A spectra. Each observed emission feature includes the primary line (the first line listed in each section), as well as all other "secondary" lines within the FWHM of the primary line that have line strengths $> 5\%$ of the primary line. Those features with the primary line and wavelength in italics are used to compute DEMs, while the other emission features (excluding Fe XVIII) are used for contextual comparison. For the primary line in each emission feature the "Relative $G(T)$" column gives the peak intensity per emission measure (erg cm^3 sr^{-1} s^{-1}) corrected for the elemental abundance (but not weighted by a DEM), as well as the ratio of this value to the Fe IX value. For the "secondary" lines only the ratio relative to the associated primary line is given.

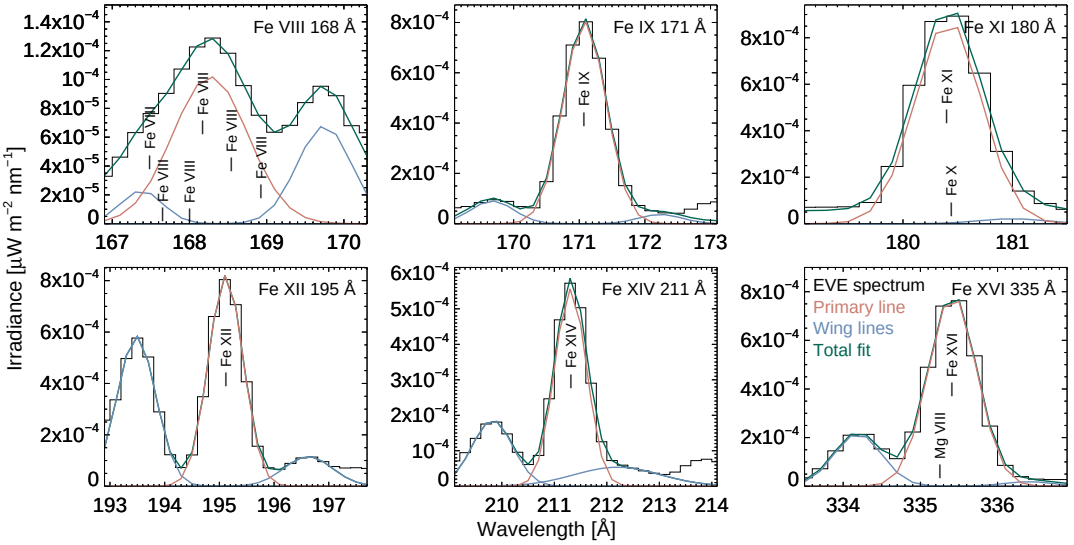

Fig. 5.2.— The EVE spectrum and associated Gaussian fits on 2011 November 6 for the italicized lines in table 5.1 used in the DEM calculations. The black histogram is the observed median EVE spectrum. The red and blue lines are the Gaussian fits for the primary line and the wing features, respectively. The green line is the total spectral fit, including the three Gaussians and a constant background. The associated contributing lines listed in table 5.1 are also indicated at the proper wavelength and relative strength.

that must be present in the spectrum to account for the offsets in the minimum flux level observed in MEGS-A spectra. The most obvious example of this is the Fe XVIII 94 Å line explored in Appendix A. True continuum emission in this region of the EUV spectrum is negligible for the non-flaring Sun, accounting for well less than 1% of the emission in any individual line.

5.2. DEM Assumptions and Calculation

The DEM with units of $\mathrm{cm}^{-3}\ \mathrm{K}^{-1}$ is defined as

$$\mathrm{DEM}(T) = \int_V \frac{d}{dT}\left(n_\mathrm{e} n_\mathrm{H}\right) dV \tag{5.1}$$

where n_e and n_H are the electron and proton number densities, respectively, T is the coronal electron temperature, and the integral is over the visible coronal volume V. This deviates from the the presentation of equation 3.3 by integrating over the emitting volume rather than path length. For spatially resolved DEMs this is equivalent to multiplying the observed DEM by the physical area (the angular size projected to the Sun) of an individual pixel. EVE measures the irradiance (W m^{-2} nm^{-1}) while CHIANTI performs calculations natively using radiance (erg cm^{-2} s^{-1} sr^{-1}). EVE's field of view is several degrees wide, and it has no spatial resolution; hence, it does not measure the actual solid angle of the solar emission. To provide CHIANTI its native radiance units the observed EVE irradiance must be divided by the solid angle occupied by the solar disk at 1 au, 6.78×10^{-5} sr, conveniently giving quantities comparable to spatially resolved DEM analysis. CHIANTI then returns the averaged column DEM $\left(cm^{-5}\ K^{-1}\right)$, which is just the total volume emission measure $\left(cm^{-3}\ K^{-1}\right)$ of the Sun divided by the area of the solar disk. Multiplying this column DEM by the area of the solar disk directly cancels the arbitrary division by the solid angle of the solar disk described above and yields the volume-integrated DEM of the solar corona.

5.2.1. Choice of Lines for DEM Fitting

Selection of suitable lines for DEM analysis is critical because the detailed atomic characteristics associated with the chosen emission lines must be fully characterized in order to properly calculate the DEM. Therefore only those emission lines that are most well characterized are used for this analysis.

Since the lines of a given charge state in Table 5.1 have essentially identical

contribution functions (emission as a function of temperature), the use of more than one line per charge state does not add more information in the DEM analysis. Use of multiple lines from the same charge state can overweight the corresponding temperature range compared to states with a single line available, and in addition this may hinder the fitting procedure if the lines have different density dependencies. Therefore, only a single line for each charge state is used in the DEM fitting. On the basis of line strength Fe VIII 168 Å is preferred to Fe VIII 131 Å and Fe XI 180.4 Å to Fe XI 188.2 Å for the DEM fits.

Pursuant to the discussion of Chapter 3.1.1, it is necessary to consider the density sensitivity of the lines used to compute the DEM. Ideally, the lines used for DEM fitting will all have similar density dependence, but in practice the limited number of lines available to choose from means that this is not generally possible. Not surprisingly, using a combination of lines with very different density dependencies typically produces poor DEM solutions. Figure 5.3 shows the density variation of the lines in Table 5.1 over the plausible coronal range 10^8–10^{10} cm^{-3}. The Fe VIII, XV, and XVI (and XVIII, not shown) lines all have essentially no density dependence over this range, while Fe IX, X, XI, XII, and XIV all show some variation with density but have very similar behavior, with increased emission at lower density. Both Fe XIII lines, however, show a dramatic change in emission with density, and in practice the inclusion of these Fe XIII lines produces very poor DEM solutions. For this reason they are excluded from the DEM calculation, but they provide a useful density diagnostic that is discussed further in Chapter 5.2.2 and 5.3.2.

The Fe X 175 Å and Fe XV 284 Å lines are both strong, relatively isolated emission features that could be expected to be valuable in constraining the DEM.

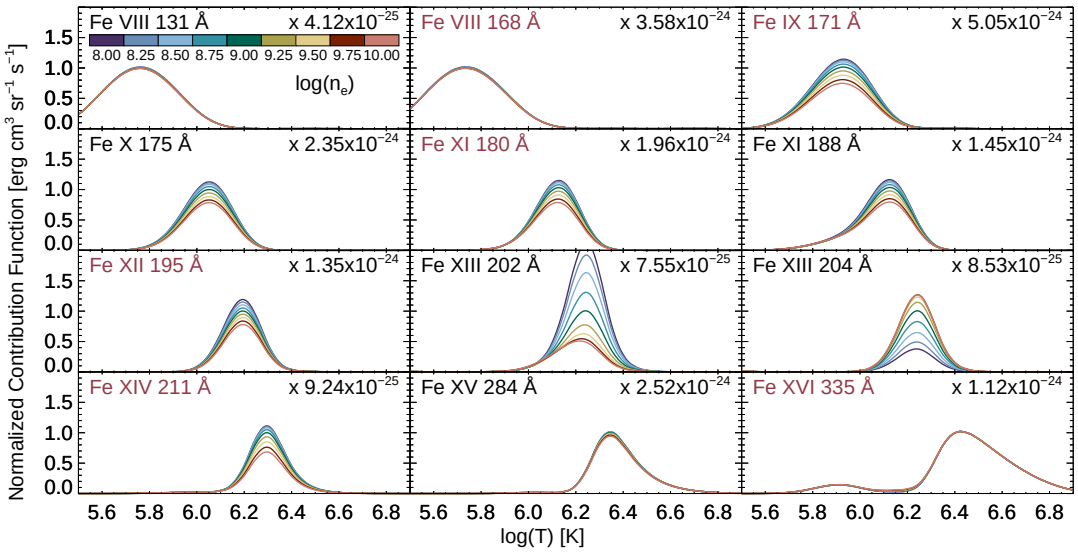

Fig. 5.3.— Contribution functions (intensity per emission measure as a function of temperature) with units of erg cm^3 s^{-1} sr^{-1} of the features in Table 5.1 (excluding Fe XVIII). Curves are plotted for nine different values of coronal density in the range 10^8–10^{10} cm^{-3} and normalized to the peak emission at 10^9 cm^{-3}. Lines labeled in red are used to compute the DEMs.

However, the inclusion of either of these lines leads to dramatic fluctuations in the DEM calculations, including the appearance of sharp reductions of emission measure at 1 MK and 2.5 MK (log(T) = 6.0 and 6.4) and generally poor reproduction of the input data. Sharp features in the DEM can be regarded as unphysical because the radiative loss functions (discussed further in Chapter 5.4) are smooth functions of temperature and there is no evidence that coronal heating favors narrow temperature ranges. Additionally, as discussed in Chapter 5.3.2, the Fe X 175 Å line shows evidence of systematic errors in its representation in CHIANTI. The Fe X 175 Å and Fe XV 284 Å lines are, therefore, excluded from the DEM fitting procedure.

The Fe XVIII line at 94 Å can provide an important constraint on the DEM at high temperatures (up to 10 MK), but it is found (in agreement with, e.g.,

Aschwanden & Boerner 2011; Reale et al. 2011; Testa et al. 2012; Aschwanden et al. 2013) that CHIANTI currently does not represent the relevant region of the EUV spectrum sufficiently well to rely on the Fe XVIII line. This issue is discussed specifically for EVE spectra in more detail in Appendix A, including the discovery of a proxy for the non-Fe XVIII component in this wavelength range.

The DEM fits are derived here using the Fe VIII, IX, XI, XII, XIV, and XVI lines marked in italics in Table 5.1. These lines span the non-flaring coronal temperature range from 0.3 to 5 MK with sufficient sensitivity over the whole range to suitably represent the solar coronal DEM.

The corresponding contribution functions (intensity per emission measure as functions of temperature) used to calculate the DEMs are shown in Figure 5.4. These are generated by summing the contribution from each CHIANTI emission line (of which the strongest contributors are listed in Table 5.1) within the FWHM centered on the wavelength of each individual EVE feature, assuming coronal elemental abundances (Feldman 1992).

5.2.2. Coronal Density

Based on the discussion of Chapter 3.1.1, a coronal density must be chosen to calculate the DEM in cases when the observed emission does not have identical density dependence. The strongest density-sensitive lines in the EVE MEGS-A range are the Fe XIII 202 Å and 204 Å lines, as shown in Fig. 5.3. Using CHIANTI to determine the density corresponding to the fluxes in these two lines in typical EVE daily spectra suggests a density of $10^{8.5-9}$ cm^{-3}. Noting the fact that EUV emission is proportional to density squared and therefore will always

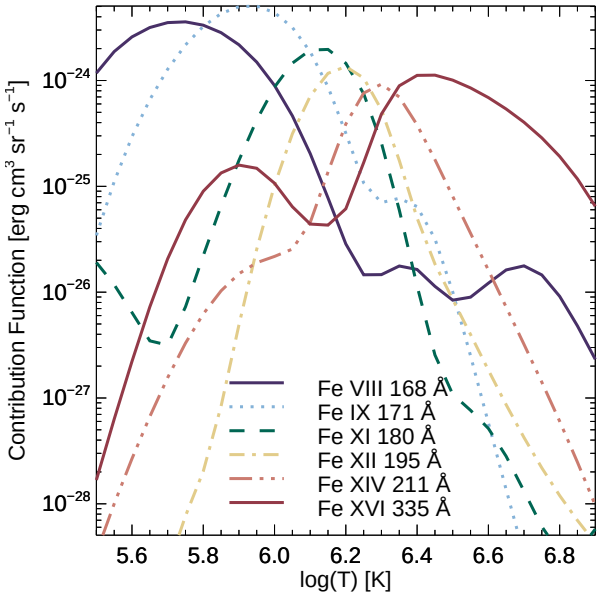

Fig. 5.4.— Contribution functions of the lines in Table 5.1. This shows the temperature sensitivity of the individual emission lines and the combined sensitivity of the DEM. Notice that even though these lines (except for Fe XVI 335 Å) can be considered isothermal, they have significant emission over a range of temperatures.

be biased toward higher densities, it is best to adopt $10^{9.0}$ cm^{-3} as the density for the DEM calculation. In order to account for the effect of this density choice on the results, the DEM can also be calculated using $10^{8.5}$ and $10^{9.5}$ cm^{-3}, and the resulting variation in the DEMs is a measure of the uncertainty in the final DEMs. It is also likely that the average coronal density will change with the solar activity level. However, the single pair of density-sensitive Fe XIII lines does not provide sufficient constraint on the temporal density evolution to vary the assumed coronal density with time in the DEM calculations.

5.2.3. Abundances

Using purely Fe emission lines to compute the DEM actually results in the DEM of Fe. This is converted into the total DEM by multiplying by $N_{\mathrm{H}}/N_{\mathrm{Fe}}$, the inverse Fe abundance (as pointed out in Chapter 3.1.2). This neglects the influence of secondary emission from other elements (such as the Mg VIII contribution to the Fe XVI line), but as these contributions are quite small, their influence is likely negligible. This means that the total DEM calculated from purely Fe emission lines scales inversely with the Fe abundance, assuming that the abundance is constant throughout the solar corona. This analysis uses the standard "coronal" iron abundance of $N_{\mathrm{Fe}}/N_{\mathrm{H}} = 1.26 \times 10^{-4}$, four times that of the photosphere (Feldman 1992), the same as Chapter 4 demonstrated to be suitable for full disk coronal analysis with emission dominated by active regions.

5.2.4. DEM Calculation

The line fluxes and uncertainties extracted from the median MEGS-A spectra are used to generate daily full-Sun-integrated coronal DEMs. These DEMs are derived using Version 8.0.2 of the CHIANTI database. The regularized-inversion DEM solution method from Hannah & Kontar (2012) is used as implemented in CHIANTI, restricting the solutions to the temperature range $5.5 \leq \log(\mathrm{T}) \leq 6.9$ with bins of $\log(T) = 0.05$. Positivity is enforced in the DEM solutions to prevent nonphysical negative emission measures, but in practice the solutions obtained using the six chosen EVE features are uniformly positive without this constraint (which is not the case when other lines in Table 5.1 are included). The full 4 yr DEM time series resulting from this analysis is shown in Figure 5.5.

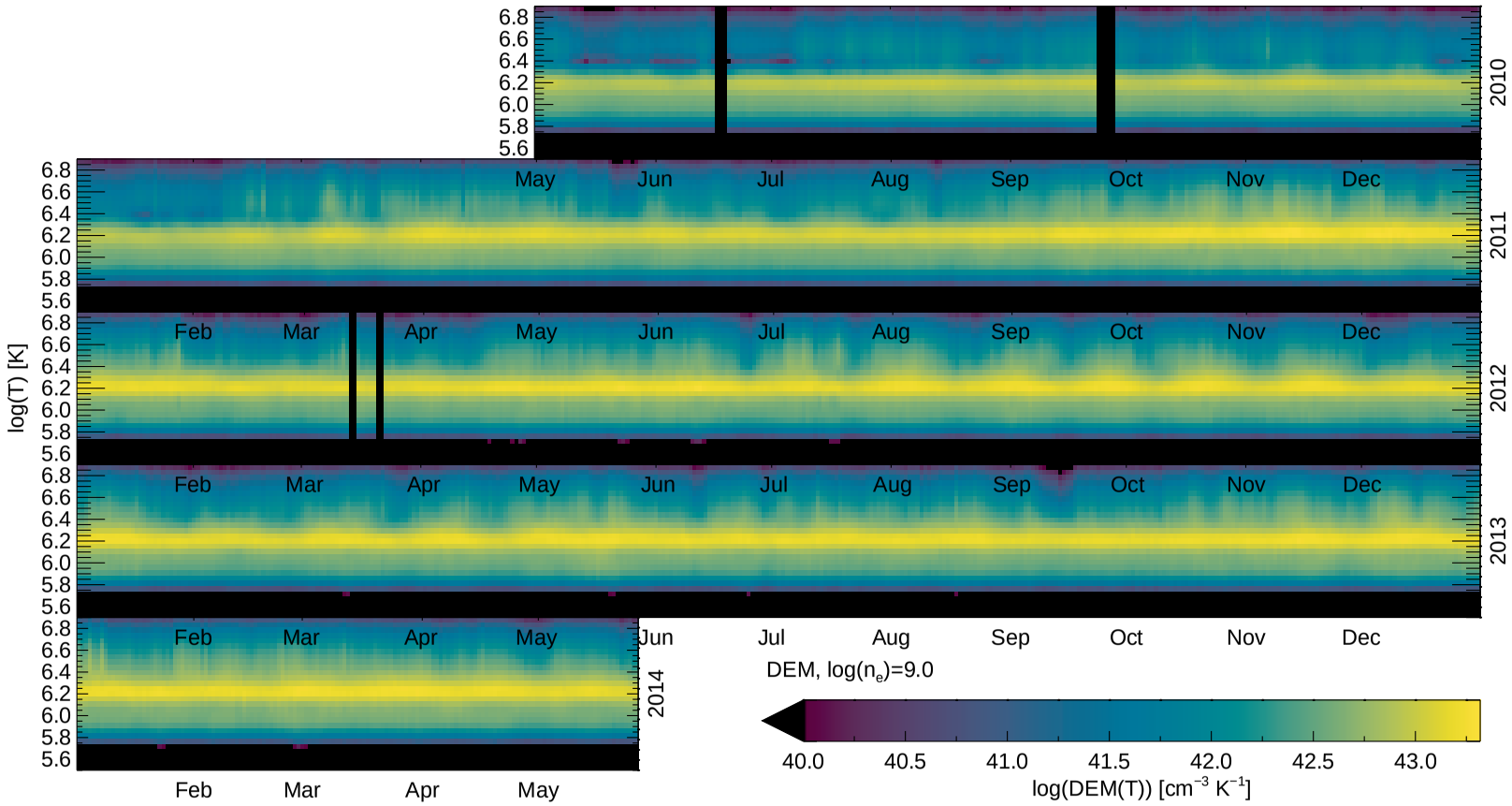

Fig. 5.5.— DEM time series calculated for the complete EVE data set. The vertical black bands in 2010 and 2012 are the result of data gaps explained in Chapter 5.1. The plot shows an increase in high-temperature plasma ($\log(T) \geq 6.3$) associated with solar maximum (2011–2014). Rotational modulation is evident throughout the observations, most clearly in the period 2012 July–2013 April.

5.3. DEM Validation

The DEMs show a clear increase in coronal activity from near solar minimum in 2010 to solar maximum in 2011–2014, including a slight increase in the peak temperature. During solar maximum, there are times when a pronounced and consistent rotational modulation signal is present (particularly 2012 July–2013 April), indicating a relatively stable corona with strong active regions in fixed longitude ranges regularly rotating on and off the visible disk. However, there are also times when the solar activity loses that regularity and the rotational signal becomes obscured, such as during 2013 June–November.

5.3.1. Uncertainty Estimates

The DEM fitting procedure involves a χ^2-minimization in which the emission measure in each temperature bin is adjusted such that convolving the DEM with the temperature responses of each of the six EVE features (Figure 5.4) produces model line fluxes that match the input line fluxes to within the specified measurement uncertainties. For completeness, the derived DEMs are used to compute daily synthetic EVE spectra with an example shown in Figure 5.1. This is done by summing the contribution from each individual emission line in the spectral range using the calculated DEM. These synthetic spectra are then fit with the same procedure as was used to fit the original EVE spectrum, but this time without the constant background component (since that was only added to account for lines not included in CHIANTI). A comparison of these derived output fluxes using the three chosen densities with the input EVE fluxes is shown in Figure 5.6. The residual plots show that for $10^{9.0}$ cm^{-3}: Fe XIV is reproduced to about 5%;

Fe VIII, Fe IX, Fe XI, and Fe XII to about 10%; and Fe XVI to better than 20%. The systematic and consistent values of these offsets over a wide range of solar activity levels suggest that they are dominated by inconsistencies in the atomic data used to derive the response of each line and/or fundamental precision errors in the EVE MEGS-A calibration. We conclude from these results that the overall uncertainty associated with the DEM fitting is of order 10%. This is consistent with the uncertainties reported by the fitting procedure, which for the individual $\log(T) = 0.05$ bins with significant emission measure (i.e., bins above $\log(T) = 5.8$) are of order 10%.

This algorithmic uncertainty associated with the line fitting and DEM calculation ignores many subtle complications in the analysis. The following additional sources of uncertainty contribute to the final estimation of the accuracy of the DEMs:

1. The time variability of the spectra within the 2 hr window used to determine the median daily spectrum. The standard deviations in each wavelength bin over the 2 hr daily window are typically about 1% for the relatively cool and consistently strong lines (Fe IX 171 Å, Fe XI 180 Å, and Fe XII 195 Å) that should represent temporal variability.

2. The calibration of the EVE MEGS-A irradiance spectra. Hock et al. (2012) discuss the calibration of MEGS-A in detail: the responsivity (conversion of detector counts to irradiance) is estimated to have an uncertainty better than 1% for most of the wavelength range of the lines used, but possibly worse in the range 150–170 Å where the A1 and A2 slit responses overlap. The irradiance calibration precision is in the range of ±5–7% for the strong

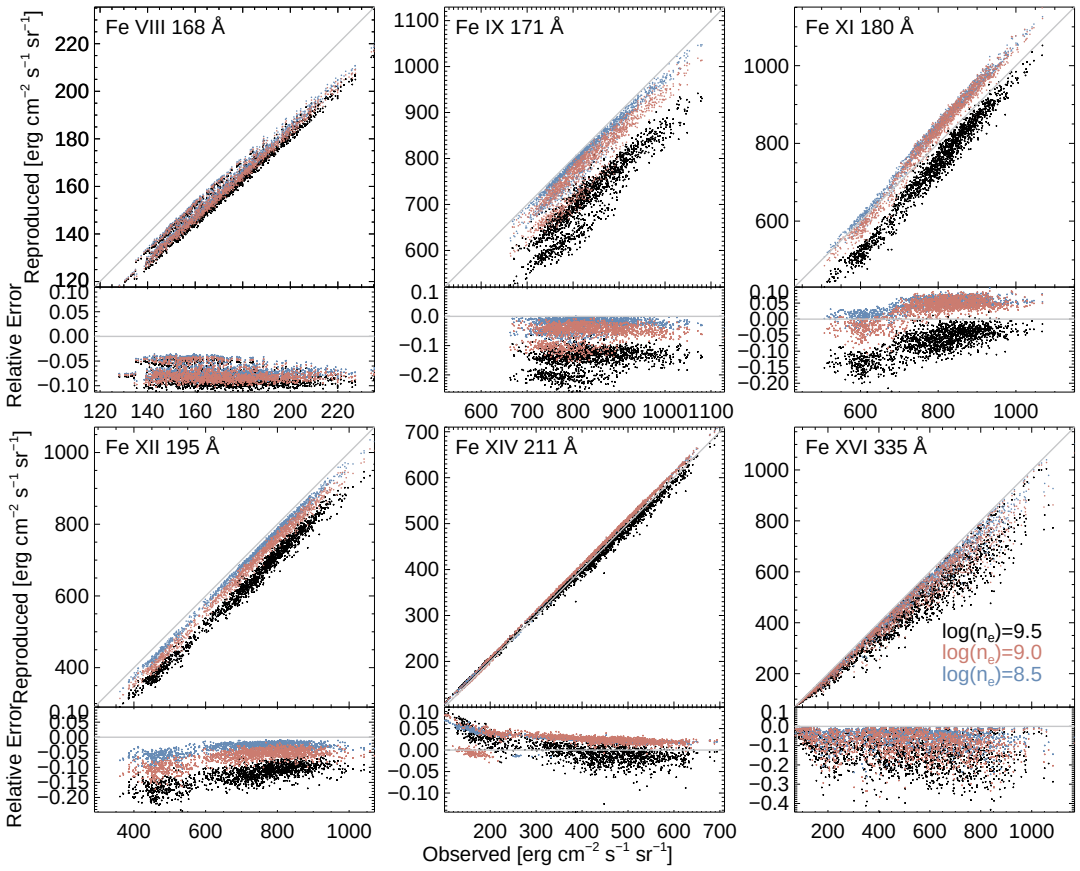

Fig. 5.6.— Fluxes reproduced by the calculated DEMs vs. the observed flux for the lines used to compute the DEMs. The diagonal gray lines indicate where the reproductions equal the observations. A clear trend of reduced reproduced line flux with increased density is seen across all lines. At $10^{9.0}$ cm^{-3}, all of the lines are reproduced to better than 20%.

MEGS-A lines considered.

3. The determination of line fluxes by fitting Gaussians to the EVE spectra. The formal uncertainties in these fits are a few percent, depending on the line.

4. Uncertainty due to the need to choose a density in calculating the temperature responses of each line. Figure 5.7 shows the total emission measure (the

integral of the DEM over temperature) for three different values of density for which calculations were carried out. The spread in the resulting emission measures is ±5%, which is taken to be the uncertainty associated with the choice of density.

5. Uncertainties in the atomic data used by CHIANTI to derive the emissivity and temperature response of the lines used for the DEM determination. As discussed in Chapter 5.3.2, there are clear discrepancies between the lines used and other strong lines in the EVE spectra. Assigning a formal uncertainty for the specific lines used to obtain the DEMs is nontrivial and not addressed here.

6. Uncertainty in the chosen abundance of Fe. As described in Chapters 3.1.2 and 5.2.2, a change in this value results in a scale change in the DEMs rather than an uncertainty. It is possible that the appropriate value of the abundance may vary with solar activity levels, but resolving that effect is beyond the scope of this study.

In summary, the overall uncertainty in the DEMs is of order 15%, with the recognition that uncertainties in the atomic data and the assumed Fe abundance are additional factors not well represented in that number.

5.3.2. DEM Testing

As a test of the DEM accuracy, Figure 5.8 gives comparisons similar to those shown in Figure 5.6 for the emission lines listed in Table 5.1 (excluding Fe XVIII 94 Å, which is discussed in detail in Appendix A) that are not used to calculate the

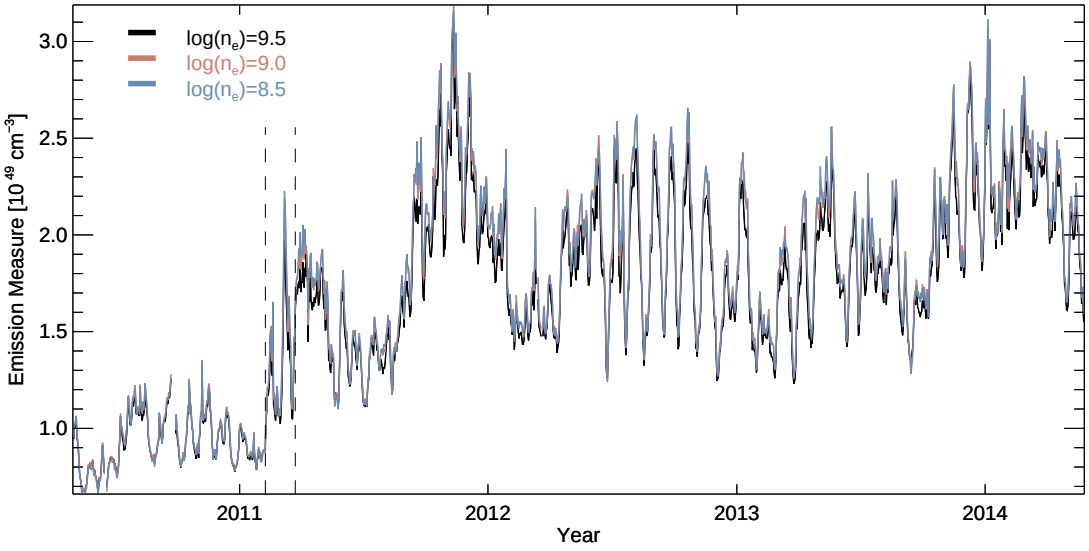

Fig. 5.7.— Total emission measure series for the complete EVE data set for each of the three tested plasma densities. The deviation of $10^{8.5}$ and $10^{9.5}$ from $10^{9.0}$ cm^{-3} is typically less than 5%, with the largest deviation during periods of maximum activity. The dashed vertical lines indicate the period of transition from solar minimum to solar maximum discussed in Chapter 5.4.1: they indicate the dates 2011 February 7 and 2011 March 23.

DEMs. As with Figure 5.6, the lines in the CHIANTI synthetic spectra resulting from the derived DEMs are fit using three Gaussians. The reproduction of these test lines is not expected to show the same level of agreement since they have no impact on the calculated DEMs, but they do reveal interesting trends that lend context to the results.

The Fe VIII 131 Å feature is composed of two similar-strength Fe VIII lines 0.3 Å apart. While it is a weak feature, there is no evidence for any significant contaminating lines within the blended feature. In particular, it does not show a response to flares seen in the nearby Fe XXIII (133 Å) feature that would suggest contamination by an unidentified hotter line. It should therefore have a response similar to the Fe VIII 168 Å line, but with much lower amplitude. Figure 5.8

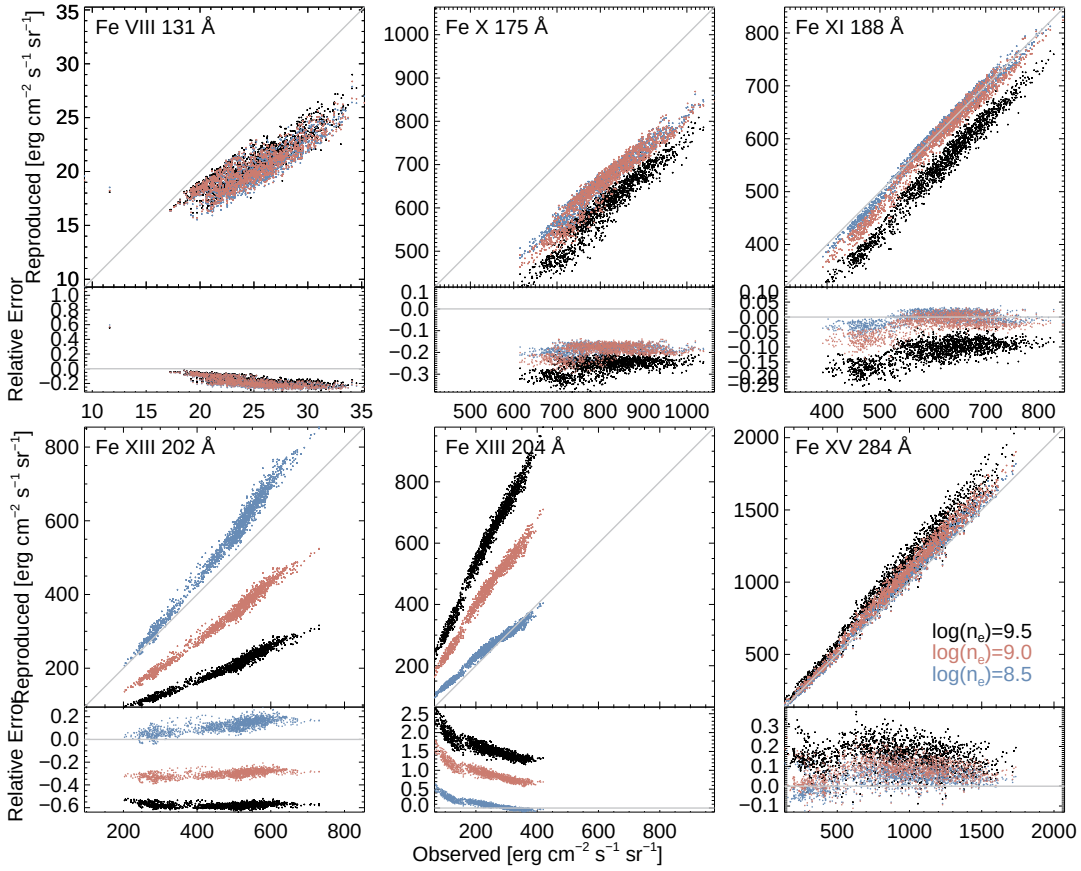

Fig. 5.8.— Same as Figure 5.6 but for the lines in Table 5.1 not used to compute the DEMs (excluding Fe XVIII). Fe VIII, Fe X, and Fe XV all show some level of consistent deviation, with Fe X being particularly striking given the high precision but low accuracy of the flux reproductions. Fe XI is reproduced extremely well. Both Fe XIII lines show clear variation with density, as expected, and are consistent with the tested density range.

shows that the DEMs reproduce the Fe VIII 131 Å feature to about 30%, with very small variation with density. Given the good reproduction of Fe VIII 168 Å, this clear trend to poorer agreement with increased flux suggests that there is a non-flare high-temperature contribution to the line not included in CHIANTI.

The Fe X 175 Å line reproduction shows relatively small spreads for the lower densities ($10^{8.5}$ and $10^{9.0}$ cm^{-3}), but the trend is depressed about 20% below the

observations. This could indicate a consistent underestimation of the emission measure near $\log(T) \sim 6.05$, but the overlapping temperature coverage of Fe IX and Fe XI (Figure 5.4) and the excellent reproduction of the Fe XI 188 Å test line (Figure 5.8) that was not used in the DEM calculation suggest instead that the CHIANTI database is incomplete in this region of the spectrum.[3]

As discussed in Chapter 5.2.1 and 5.2.2 and shown in Figure 5.3, the Fe XIII 202 and 204 Å lines have strong and opposite dependencies on density, with the 202 Å line intensity decreasing and the 204 Å line increasing, respectively, as density increases. The effects of the density sensitivity are obvious in Figure 5.8 where the reproduced flux in these lines changes as expected with density. As noted in Chapter 5.2.2, each of these lines suggests a density in the range $10^{8.5}$–$10^{9.0}$ cm^{-3}.

The strong Fe XV 284 Å line tends to be overpredicted (between 0% and 25% depending on density) during periods of increased activity. This line dominates its region of the spectrum and therefore has very little contamination. It is unlikely that the calculated DEMs have excess emission measure at the peak response of Fe XV ($\log(T) \gtrsim 6.35$) since this temperature is also well sampled by the responses of the strong Fe XIV 211 Å and Fe XVI 335 Å lines (Figure 5.4). It has been suggested that resonance scattering can affect the intensities of strong EUV lines such as Fe XV 284 Å by spatially dispersing photons (e.g., Schrijver & McMullen 2000; Wood & Raymond 2000), but Brickhouse & Schmelz (2006)

[3]Note that the MEGS-A instrument has two slits, A1 and A2, optimized for the 60–180 Å and 160–370 Å wavelength ranges, respectively, and 175 Å is close to the region (away from 171 Å) where the A1 and A2 spectra are merged. The responsivity of MEGS-A2 has an edge at 175 Å, suggesting that this might cause issues for the Fe X line, but calibration data (Hock et al. 2012) show a very smooth transition in the response of the merged spectra at 175 Å, and the excellent reproduction of strong lines on either side of this wavelength argues against an instrumental problem.

argued that the optical depth of Fe XV 284 Å is unlikely to be high enough, and in any case spatial redistribution by resonance scattering should not affect full-Sun irradiance measurements such as those made by EVE. The reconstruction of the Fe XV 284 Å line intensities is consistent with the stated uncertainty.

Overall the test lines demonstrate both the difficulty of this analysis, given its reliance on incomplete EUV emission data, and the robustness of the DEM results to within the stated uncertainty. The results for those lines reproduced most poorly (Fe VIII, Fe X, and Fe XIII) can only be explained through systematic effects, while the Fe XI and Fe XV lines are reproduced with fidelity similar to the lines used in the DEM calculations.

5.4. The Energy and Evolution of the Solar Corona

To show quantitatively how the DEMs evolve with solar activity, the DEMs from three different solar activity levels are plotted in Figure 5.9. The peak temperature of the DEM is very similar in all cases, just below 1.6 MK ($\log(T) = 6.2$) during solar minimum and just above during solar maximum. Additionally, while the low-temperature side of the DEMs are similar on all three dates, there are dramatic differences in the high-temperature sides of the DEM. During solar minimum, there is very little material above the peak in the temperature distribution, with almost none above 2.5 MK ($\log(T) = 6.4$). During solar maximum, the bulk of the emission measure lies at temperatures greater than the peak, and there is significant emission from plasma up to 6 MK ($\log(T) = 6.8$). This compares well with previous work examining the spatial distribution of the DEM (Orlando et al. 2001) and the long-term evolution of the global DEM (Orlando et al. 2004;

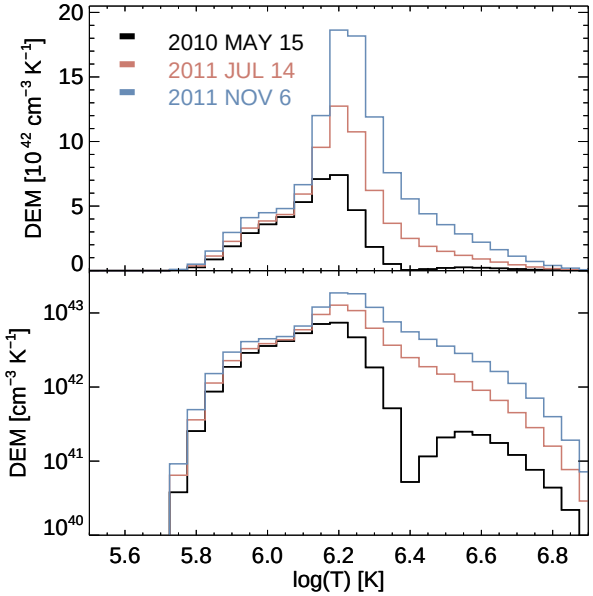

Fig. 5.9.— DEM solutions (top: linear scale; bottom: logarithmic scale) for a density of 10^9 cm^{-3} at three different activity levels: a solar minimum DEM (black, 2010 May 15), a "typical" solar maximum (with frequent B flares) DEM (red, 2011 July 14), and a high activity solar maximum (two M- and and nine C-class flares, all outside the observation window) DEM (blue, 2011 November 6). These show that the DEM remains relatively consistent at temperatures below $\log(T)$=6.1 but that the plasma content of the corona at higher temperatures changes dramatically with solar activity. The dip at $\log(T)$=6.4 in the 2010 May 15 DEM is likely an artifact of the fitting process when the high-temperature lines are weak.

Argiroffi et al. 2008). These studies used observations from the *Yohkoh* Soft X-ray Telescope that are sensitive to much higher temperatures than explored here but are less accurate at the low-temperature end of the DEMs(Orlando et al. 2000).

To further illustrate this variation in the DEMs, Figure 5.10 shows the time series of the DEM-weighted average temperature of the solar corona and the DEMs binned into three different temperature ranges: below the temperature peak of the DEM ("cool," $5.5 \leq \log(T) < 6.1$), around the temperature peak ("warm," $6.1 \leq \log(T) < 6.3$), and above the temperature peak ("hot," $6.3 \leq \log(T) < 6.9$). The "cool" corona appears to be almost independent of the solar cycle,

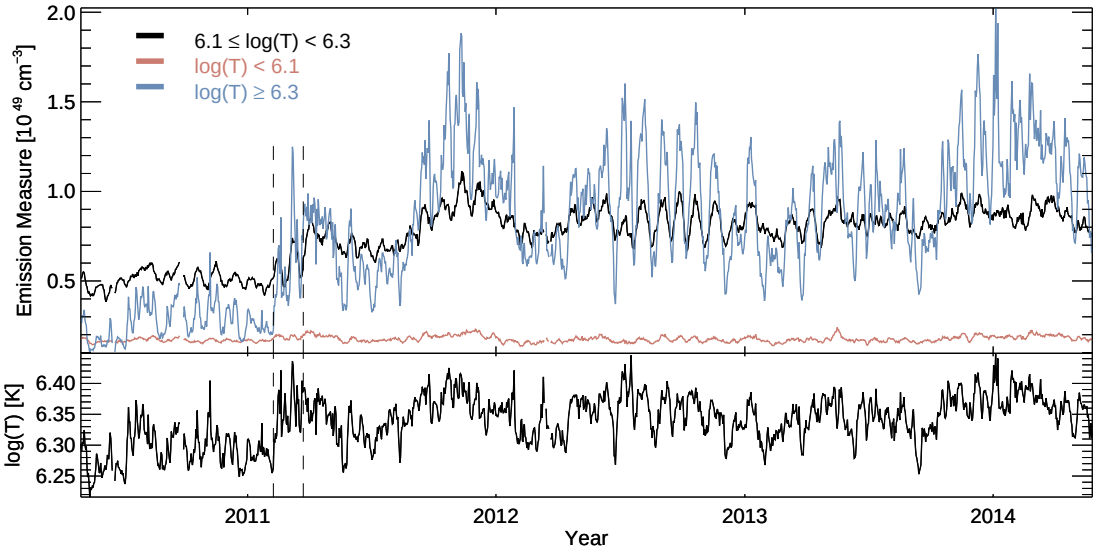

Fig. 5.10.— Top: emission measure from Figure 5.5 in the "cool" (red, $\log(T) < 6.1$), "warm" (black, $6.1 \leq \log(T) < 6.3$), and "hot" (blue, $\log(T) \geq 6.3$) temperatures. Bottom: emission-measure-weighted mean temperature for the complete EVE data set. The dashed vertical lines indicate the period of transition from solar minimum to solar maximum discussed in Chapter 5.4.1. This plot shows the consistency of the low-temperature corona, while the high-temperature corona changes dramatically over the solar cycle.

with little change due either to solar rotation or to the activity level over the 4 yr of observation. On the other hand, the "warm" and "hot" coronas vary by a factor of two and an order of magnitude, respectively. These results are consistent with observations that solar activity is manifested primarily through increased hot plasma in active regions, and confirm that there is very little change in the quiet-Sun corona throughout the solar cycle. The increase in high-temperature plasma causes the DEM-weighted average temperature to rise from a minimum of 1.6 MK ($\log(T) = 6.2$) during solar minimum to above 2.5 MK ($\log(T) = 6.4$) during high activity periods at solar maximum.

This additional "hot" plasma does not appear as additional emission measure cooling through the <1 MK range, in part due to the temperature dependence

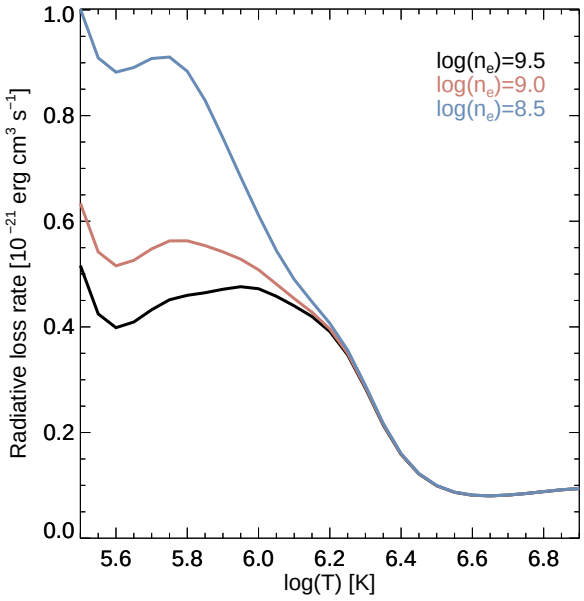

Fig. 5.11.— Radiative loss functions per unit volume emission measure as a function of temperature for the three coronal densities considered here. These are calculated using the `rad_loss.pro` function in CHIANTI 8.0.2 (see the corresponding plot from CHIANTI 6 in Dere et al. (2009)) assuming Feldman (1992) coronal abundances. This shows that coronal emission is strongly weighted toward the "cool" and "warm" corona below $\log(T) = 6.3$.

of the radiative loss function shown in Figure 5.11. The loss rate is significantly greater below 1 MK ($\log(T) = 6.0$) than at higher temperatures, especially at lower densities. This means that "hot" plasma (which experiences significant cooling through conduction to the lower atmosphere; Antiochos & Sturrock 1976, 1978) will remain so for a long time, and once it drops to sufficiently low temperature, it will tend to cool out of the "warm" and "cool" temperature range quickly. This effect has been termed "catastrophic cooling" (Reale et al. 2012; Reale & Landi 2012; Cargill & Bradshaw 2013) and involves draining of cool plasma back into the lower atmosphere (Bradshaw & Cargill 2010) in addition to radiative cooling.

5.4.1. A Two-state Corona?

The emission from the corona can be described as a combination of the emission from the quiet Sun, coronal holes, and active regions (and trace contributions from smaller features such as filament channels, prominences, etc.). Each of these distinct features has its own characteristic emission spectrum determined by its unique plasma parameters, and the total solar spectrum is the sum of these spectra weighted by their respective covering fractions of the visible solar disk (e.g., Fontenla et al. 2017). With this description it is clear that the total solar spectrum will change as a function of solar activity as is observed. A priori this variation is expected to be continuous as features evolve and rotate on and off the disk and the overall level of activity changes with the solar cycle. However, the data suggest that this is not the case: a rapid transition is observed between the early period of EVE data, near solar minimum conditions, and the later period around solar maximum that suggests a fundamental bifurcation in the DEM over the solar cycle.

This discontinuity is shown in Figure 5.12 for four sets of observed line fluxes, three AIA bands, and the calculated DEMs. Panels (a)–(d) show the relationship over the 4 yr of EVE data comparing the Fe XIV 211 Å and Fe IX 171 Å lines with the Fe VIII 168 Å and Fe XII 195 Å lines. Both Fe VIII 168 Å and Fe IX 171 Å have their strongest responses at temperatures below the DEM peak, whereas Fe XII 195 Å and Fe XIV 211 Å contribute at or above the temperature peak (see Figure 5.4). Panels (a) and (d) show general linear trends between the line pairs that cluster into two distinct sets, one for the solar minimum conditions before 2011 February 8 (blue points) and one for the solar maximum conditions

after 2011 March 23 (black points), although these dates are chosen somewhat arbitrarily. For example, a given observed flux in Fe IX 171 Å implies two very different Fe XII 195 Å fluxes, depending on the level of solar activity. The most obvious explanation for such a sharp transition in the observed fluxes would be a calibration error in the EVE MEGS-A data. However, while the calibration of MEGS-A spectra is updated with rocket underflights (including one on 2011 March 23, near the division between solar minimum and maximum identified here; Hock et al. 2012), these calibrations are applied in a continuous fashion specifically designed to prevent the kind of discontinuity observed here. Panels (b) and (c) show that for lines originating from plasma of similar temperature, the linear trends are uniform, with the transition points (red crosses) clearly connecting the solar minimum and maximum trends. The fact that this activity discontinuity is seen across multiple, but not all, line pairs strongly suggests that it is a true feature of the emission and not a result of calibration errors. Additionally, panels (e) and (f) compare observations from the AIA and are nearly identical to their EVE counterparts in panels (b) and (d).

The same discontinuity appears in panels (g) and (h) of Figure 5.12, which show a similar linear relationship and coronal activity clustering but for the total "hot" versus "cool" and "warm" versus "cool" emission measure, respectively. This indicates that the shape of the DEM changes discontinuously between solar minimum and solar maximum, with almost no increase in the "cool" plasma after activity turns on. If the three sets of points formed a single linear feature with a gap during the transition (like panel (b)), it would simply indicate a rapid turn-on of activity; instead, the fact that the black and blue sets of points both have similar slopes but are offset relative to one another appears to indicate a

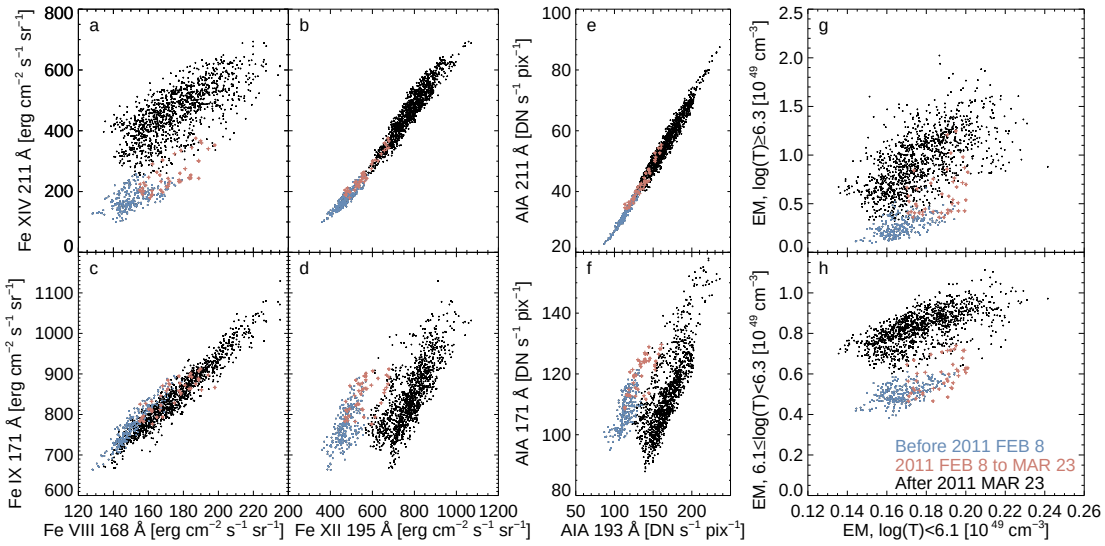

Fig. 5.12.— Observed emission in the EVE line pairs: (a) Fe XIV 211 Å vs. Fe VIII 168 Å, (b) Fe XIV 211 Å vs. Fe XII 195 Å, (c) Fe IX 171 Å vs. Fe VIII 168 Å, (d) Fe IX 171 Å vs. Fe XII 195 Å, the AIA band pairs (e) 211 Å vs. 193 Å and (f) 171 Å vs. 193 Å, and the calculated (g) "hot" vs. "cool" and (h) "warm" vs. "cool" emission measure. In all plots, the blue points indicate solar minimum (before 2011 February 8) and the black points indicate solar maximum data (after 2011 March 23), while the red crosses indicate measurements during the intervening transition (see also Figures 5.7 and 5.10). Panels (b) and (c) compare lines originating from similar temperature plasma that have a simple linear relationship. Panels (a) and (d) compare lines originating from different temperature plasma with a clear difference between the solar minimum and maximum trends. Panels (e) and (f) are equivalent to panels (b) and (d), respectively, but with the disk-integrated AIA observations. The AIA measurements are the mean values derived from the AIA "light-curve" data files provided in the SDO "SunInTime" daily directories. Panels (g) and (h) demonstrate that the "cool" plasma is nearly decoupled from the "warm" and "hot" plasma with different solar minimum and maximum trends.

fundamental change in the shape of the DEM. The timing of this transition period in 2011 February–March is of interest because the first X-class flare of cycle 24 occurred on 2011 February 15, during the transition period. It also coincides with the equatorial termination of the magnetic activity bands associated with cycle 23 identified in McIntosh et al. (2014), which they suggest defines the start of the ascending phase of cycle 24. The correlation of the change in coronal behavior with $F_{10.7}$ and the photospheric magnetic field is addressed in Chapter 6.1.2.

5.4.2. The Coronal Thermal Energy Content

The total thermal content of the corona is of interest for understanding the energetics of the solar atmosphere and the role of heat transfer in the temperature structure of the corona. To my knowledge, this quantity has not previously been addressed in any detail. The EVE DEMs derived here can be used to estimate the coronal thermal content.

The dominant components of the corona are protons, alpha particles, and electrons. Accordingly, the thermal energy can be expressed as

$$\begin{aligned} E &= \frac{3}{2} \int_V \int \frac{d}{dT} \big(n_{\rm e}(T) + n_{\rm H}(T) + n_{\rm He}(T) \big) \times k_{\rm B} T \; dT \; dV \\ &= 3.375 \; k_{\rm B} \int_V \int \; \left(\frac{d}{dT} \; n_{\rm H}(T) \right) T \; dT \; dV, \end{aligned} \tag{5.2}$$

where $k_{\rm B}$ is Boltzmann's constant, $n_{\rm e} = n_{\rm H} + 2n_{\rm He}$ for the assumed fully ionized corona, and the standard value $n_{\rm He}/n_{\rm H} = 0.085$ (Asplund et al. 2009) is adopted. Using Equation 3.3 and noting the assumed constant coronal density, the total energy relates to the DEM by

$$E = \frac{3.375 \; k_{\rm B}}{n_{\rm e}} \int \; {\rm DEM}(T) \; T \; dT. \tag{5.3}$$

A large uncertainty arises from the division by $n_{\rm e}$ in Equation 5.3. Since the DEM is density squared and Figure 5.7 shows that the density assumption has only a small effect on the derived DEM, the calculated coronal energy is essentially inversely proportional to the density used in the DEM calculation. Thus, for the assumed density range $10^{8.5}$–$10^{9.5}$ cm^{-3}, the energy can vary by a factor of about

three from the value obtained using the central 10^9 cm^{-3}.

Assuming a constant density for this energy calculation is fundamentally different from the constant density assumption made in Chapter 5.2.2, where an order-of-magnitude change in density typically caused only a 50% change in emission. Here, the constant-density assumption allows the density to be pulled out of the integral and is equivalent to assuming that the DEM results only from variations in the emitting volume with temperature. This means that all the caveats mentioned in Chapter 3.1.1 relating to a spatially and temporally variable coronal density can have an even larger distorting effect when calculating the coronal thermal energy. Nonetheless, this approach yields an order-of-magnitude estimate of coronal energy that is useful for discussing trends with solar activity.

From equation 5.3 the visible coronal volume contains on the order of 10^{31} erg of thermal energy, suggesting that the total coronal volume contains less energy than a typical X-class solar flare (Sun et al. 2012; Tziotziou et al. 2013; Aschwanden et al. 2014). This thermal energy increases by just under an order of magnitude at periods of peak activity, compared to the low-activity levels early in the *SDO* mission, due to both the general increase in emission measure and the specific increase in "hot" plasma seen in Figure 5.10. Due to the factor of T inside the integral in Equation 5.3, the "hot" corona disproportionately influences the total thermal energy, containing the majority of the energy during solar maximum. Conversely, the "cool" corona contains only a very small fraction of the thermal energy, even at low activity levels.

Total radiative energy output from the corona is calculated by integrating the product of the DEM with the radiative loss curve for 10^9 cm^{-3} shown in

Figure 5.11. This result is shown in Figure 5.13, with the contributions from the three temperature regimes discussed in Chapter 5.4 plotted individually. It is striking that the total radiative energy loss varies by only a factor of three over the wide range of coronal conditions observed in the 4 yr period. This results from the shape of the radiative loss curve and the fact that radiation is much more efficient from plasma with temperatures below 2 MK ($\log(T) = 6.3$) than from hotter plasma. This means that most of the emission results from the relatively low variability "cool" and "warm" components even though they contain the minority of the energy. If it is assumed that the radiative loss is from a single hemisphere (even though a fraction of visible off-limb plasma will always be beyond the solar limb and therefore above the far hemisphere), the hemisphere-averaged coronal radiative energy loss can be calculated. The typical 3×10^{27} erg s^{-1} solar minimum rate from Figure 5.13 corresponds to an average radiative flux of 1×10^5 erg cm^{-2} s^{-1}, exactly matching the traditional estimate for quiet-Sun regions. A typical solar maximum value of 6×10^{27} erg s^{-1} corresponds to 2×10^5 erg cm^{-2} s^{-1}, well below the typical radiative loss rate of an individual active region, 5×10^6 erg cm^{-2} s^{-1} (e.g., Withbroe & Noyes 1977).

Dividing the total energy by the radiative energy loss rate produces the coronal energy turnover timescale, the time needed to radiate away the total energy at the calculated loss rate. The resulting timescale is about an hour, and typically longer during solar maximum than solar minimum. The timescale is shorter during solar minimum conditions both because the total coronal energy is lower and because the "cool" and "warm" components, which radiate more rapidly, contain a larger fraction of the total energy. This timescale only accounts for radiative losses and does not include heat conduction into the lower (and cooler) solar at-

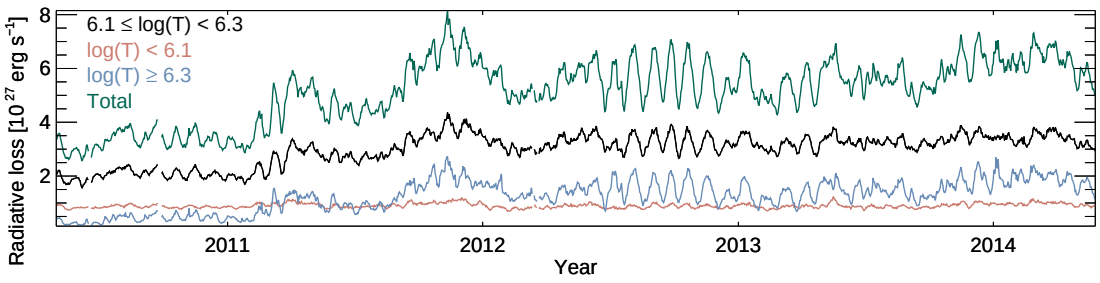

Fig. 5.13.— Total radiative energy loss rate from the corona derived from the EVE DEMs assuming a density of 10^9 cm^{-3} and coronal abundances. The total energy loss rate is shown in green, and the contributions from plasma in the temperature ranges from Figure 5.10 are also plotted: "cool" (red, $\log(T) < 6.1$), "warm" (black, $6.1 \leq \log(T) < 6.3$), and "hot" (blue, $\log(T) \geq 6.3$).

mosphere, meaning that the actual energy replacement timescale for the solar corona will be significantly shorter than estimated here (e.g. Rosner et al. 1978; Klimchuk et al. 2008). This is a characteristic timescale for the global corona; as discussed in Chapter 3.1.1 the density variation between environments in the corona (coronal holes, quiet Sun, active regions, etc.) will result in greatly varying energy replenishment times in different coronal features.

5.5. Results

I have used EVE median spectra to generate daily DEM distributions for the entire 4 yr period of operation of the EVE MEGS-A detector. This resulted in DEMs derived from a uniform data set beginning in 2010 at near-solar-minimum conditions and continuing through the maximum of solar cycle 24. The DEMs are calculated using six emission features dominated by Fe lines of charge states VIII, IX, XI, XII, XIV, and XVI that adequately sample the quiet-Sun coronal temperature range 0.3–5 MK ($\log(T) = 5.5$–6.7). Other strong lines are investigated and found to lead to poorer DEM solutions. In particular, it can be demonstrated

(see Appendix A) that CHIANTI does not currently reproduce EVE spectra in the wavelength range near the Fe XVIII line at 93.9 Å, making it unsuitable as a constraint on high-temperature quiet-Sun emission.

In order to generate the temperature responses, a quiet-Sun coronal abundance for Fe and density have to be specified. The standard Feldman (1992) coronal Fe abundance and a density of $10^{9.0}$ cm^{-3} are adopted, with the results for $10^{8.5}$ and $10^{9.5}$ cm^{-3} serving as a measure of the density uncertainty. The short-term daily variability, uncertainties in the atomic data, calibration of EVE, and spectral fitting also contributed to the overall uncertainty in these results, estimated to be no better than 15%. Future improvements in the relevant atomic data and better understanding of coronal abundances will alter the results. Therefore, the trends evident in the DEM results should be considered more robust than their absolute values.

The behavior of the coronal DEM over the 4 yr period is consistent with an intuitive understanding of a corona consisting of two primary components: the quiet Sun and active regions. The quiet-Sun DEM component with a peak temperature of 1.6 MK ($\log(T) = 6.2$) and little emission measure above 2 MK ($\log(T) = 6.3$) is present and relatively constant throughout the solar cycle. This suggests that, outside of active regions, there is little difference in the quiet Sun between solar minimum and solar maximum. The active region DEM component with a peak temperature above 2 MK ($\log(T) = 6.3$) varies by more than an order of magnitude with the solar cycle. Plasma in the 1.25–2 MK ($\log(T) = 6.1$–6.3) range varies by a factor of three over the 4 yr and alternates with the hotter component as to which is (quantitatively) dominant during solar maximum.

The total energy of the visible solar corona, its radiative energy loss rate, and the corresponding energy turnover timescale are also estimated. During solar maximum, the higher-temperature component dominates the energy content of the corona. The coronal radiative energy loss rate varies by only a factor of three over the solar cycle, due to the fact that the more stable cooler coronal material has a loss rate much higher than the highly variable "hot" component. The energy turnover timescale is on the order of an hour, but results for the total energy and the energy turnover timescale are very uncertain due to the strong dependence of both the total energy and the turnover timescale on density. Additionally, a discontinuity is identified in the behavior of coronal diagnostics in 2011 February–March, around the time of the first X-class flare of cycle 24, that suggests fundamentally different behavior in the corona under solar minimum and maximum conditions.

6. EVALUATING THE COMPONENTS OF THE $F_{10.7}$ TIME SERIES

Modern $F_{10.7}$ measurements are performed three times daily at the Dominion Radio Astrophysical Observatory in Okanagan Falls, British Columbia. Measurements are made using two redundant flux monitors each consisting of a 1.8 m paraboloid with a dual receiver system containing both low and high sensitivity channels connected by waveguide. $F_{10.7}$ observations are made in a 100 MHz band centered on 2.800 GHz averaged over an hour with a repeated observation pattern designed for stability and repeatability used to make each measurement. For a history of the Solar Radio Monitoring Program and the specifics of $F_{10.7}$ observations and calibration see Tapping (2013).

The continued use of $F_{10.7}$ as a primary input to empirical models of solar EUV irradiance (Tobiska 1996; Girazian & Withers 2015) and ionosphere-thermosphere models (Bowman et al. 2008; Truhlik et al. 2012; Qian et al. 2014) even as new proxies are developed (Tobiska et al. 2008) is a testament to the robust relationship between EUV and $F_{10.7}$. However, acknowledged shortcomings in the EUV-$F_{10..7}$ connection, particularly their decoupling during the last solar minimum (Chen et al. 2011) and observed nonlinearity at high activity levels (Chen et al. 2012), have motivated the development of proxies directly from UV and EUV observations (Suess et al. 2016).

As discussed in Chapters 1.3 and 2.3, one of the primary complications involved in relating $F_{10.7}$ to solar EUV emission is the relative contribution of the gyroresonance and bremsstrahlung mechanisms in the production of $F_{10.7}$. In Chapter 4, gyroresonance emission only contributed $8.1 \pm 0.5\%$ of the variable

$F_{10.7}$ on the observed day. However, based on a blind source separation analysis comparing various radio time series, on page one Dudok de Wit et al. (2014) claim that gyroresonance emission accounts "for 90% of the rotational variability in the $F_{10.7}$ index" and suggest that longer wavelengths (specifically 30 cm, 1 GHz) should be used instead because a larger fraction of the signal is due to bremsstrahlung emission. In this chapter, the DEMs derived and analyzed in Chapter 5 are used to directly compute the bremsstrahlung component of $F_{10.7}$ and the corresponding expected gyroresonance emission.

6.1. Bremsstrahlung and Gyroresonance Emission in $F_{10.7}$

This analysis uses the 20 UT $F_{10.7}$ measurements adjusted to 1 AU (to match the choice of EVE spectra in Chapter 5.1) except in cases where they are unavailable, or when the 20 UT $F_{10.7}$ is unrepresentative of the daily average (such as when the measurement was taken during a flare). In these cases, the average of the other $F_{10.7}$ measurements (either 17 and 23 or 18 and 22 UT, depending on the season) is used instead.

The bremsstrahlung component of $F_{10.7}$ (and in fact any microwave frequency, subject to the optical depth complications discussed in Chapter 4.4) is calculated, using the DEM time series presented in Chapter 5, to directly split the contribution from the two emission mechanisms. This is done using equation 2.3 for the complete four year data set and plotted compared to the observed $F_{10.7}$ in Figure 6.1. The bremsstrahlung prediction accounts for most of $F_{10.7}$ at the beginning of the observations near solar minimum, but once the activity turns on in early 2011 (see Chapter 5.4.1) the bremsstrahlung component is clearly insufficient to

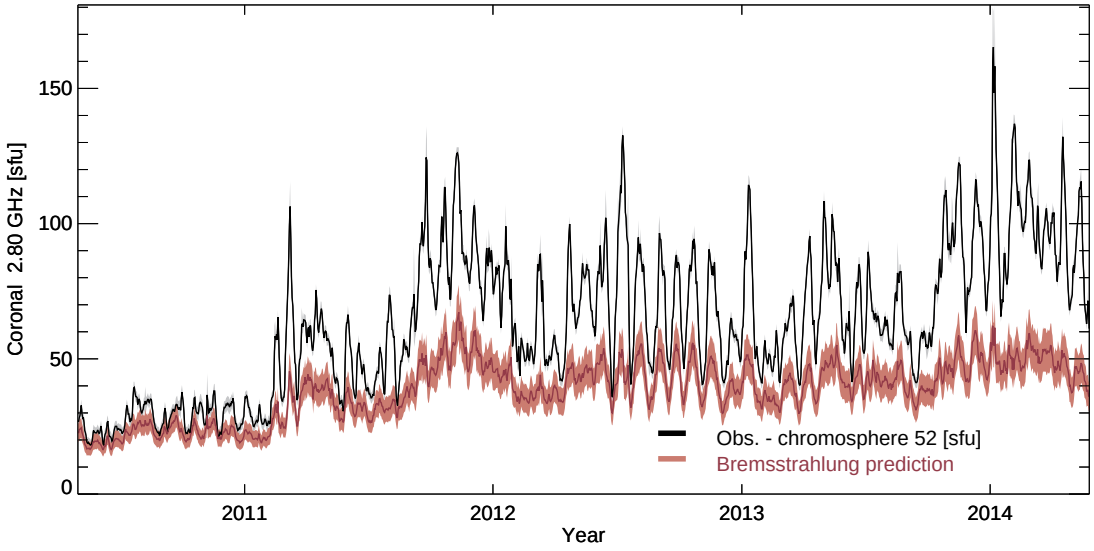

Fig. 6.1.— Time series of the observed $F_{10.7}$ (black) and the predicted bremsstrahlung component of this observation (red). A constant chromospheric component has been subtracted from the observed series as described in Chapter 6.3.2. The difference between these two series is the gyroresonance component of $F_{10.7}$.

explain the observed $F_{10.7}$.

In Figure 6.2 all three components of the observed $F_{10.7}$ series are plotted along with the observation. In Figure 6.3 the fractional contribution of these same components relative to the total observation is shown. The best-fit chromosphere is a constant determined from the procedure described in Chapter 6.3.2. The gyroresonance series is calculated as the difference between the observation and the combined bremsstrahlung prediction and chromospheric background, i.e.

$$F_{10.7} = F_{chromosphere} + F_{bremsstrahlung} + F_{gyroresonance}. \quad (6.1)$$

Notably, this analysis shows that for most of the series, the chromosphere contributes more to $F_{10.7}$ than does the coronal bremsstrahlung emission, and both contribute more than coronal gyroresonance. During the two most active periods (near the end of 2011 and the beginning of 2014) there is approximate equipar-

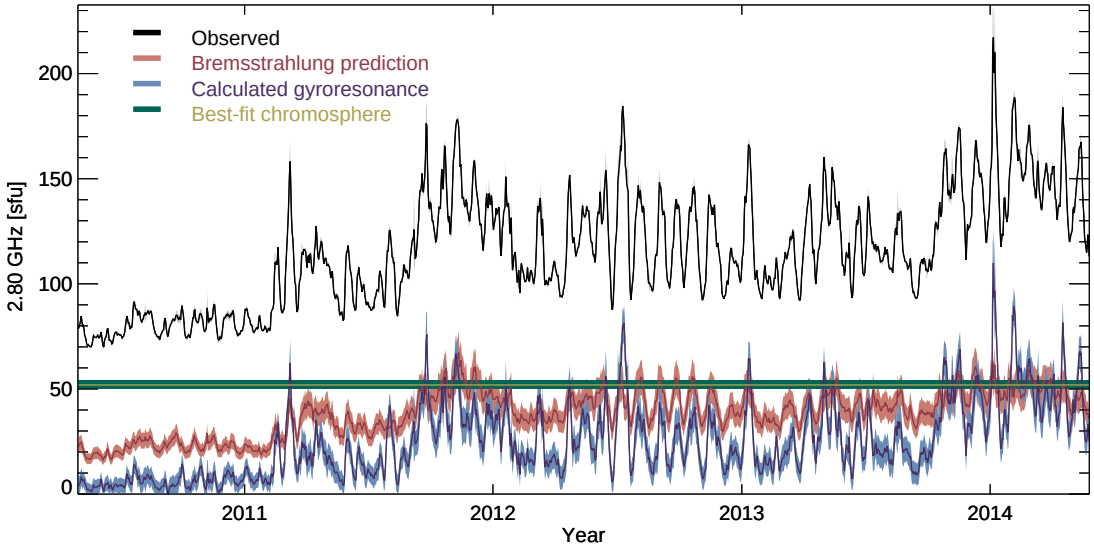

Fig. 6.2.— Time series of the observed $F_{10.7}$ and the contribution of each emission component. The chromosphere series is the best-fit constant chromospheric component as described in Chapter 6.3.2. The gyroresonance component is defined as the difference between the observation and the combined bremsstrahlung prediction and chromospheric contribution.

tition between the three components. Because this plot is made with a constant chromosphere, comparison between the bremsstrahlung and gyroresonance components shows that bremsstrahlung usually dominates the total coronal signal. In the most extreme case of January 2014, the gyroresonance contribution is about twice the bremsstrahlung component. Solar cycle 24 has been significantly weaker than previous cycles (e.g. Huang et al. 2016) and it is possible that the gyroresonance contribution is greater during more active cycles. That said, the bremsstrahlung component is actually a very stable fraction of the total $F_{10.7}$, 20–40% over all levels of solar activity. The gyroresonance fraction on the other hand changes dramatically, between 0% during solar minimum to more than 40% during solar maximum.

These findings are somewhat in conflict with the Dudok de Wit et al. (2014)

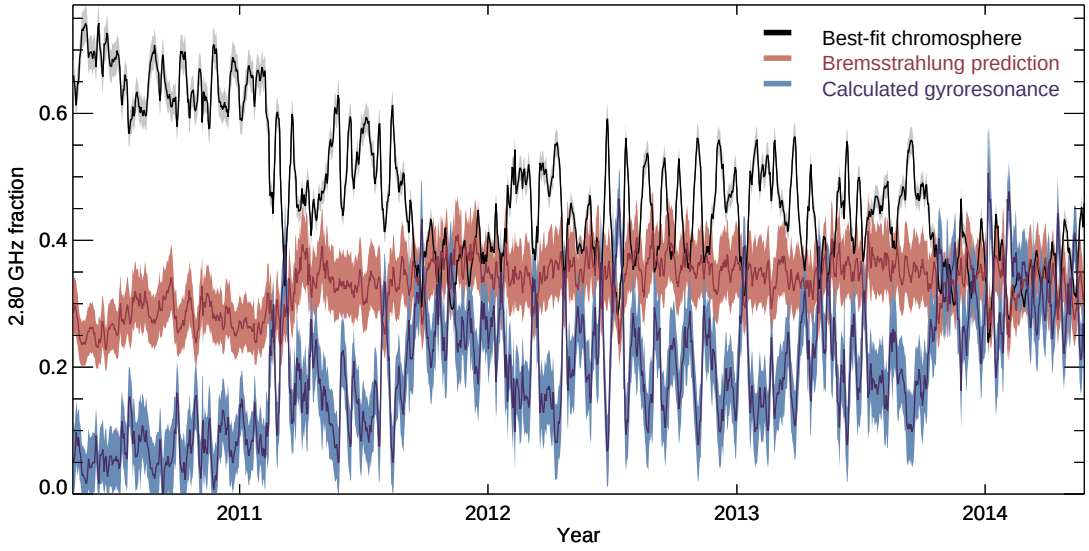

Fig. 6.3.— Time series of the fractional contribution of each emission component of the observed $F_{10.7}$. The chromosphere series is the best-fit constant chromospheric component as described in Chapter 6.3.2. The gyroresonance component is defined as the difference between the observation and the combined bremsstrahlung prediction and chromospheric contribution.

result that rotational variability is dominated by gyroresonance emission. However, Dudok de Wit et al. (2014) define the rotational variability more narrowly than the definition used here, the excess over the solar minimum level, which may explain their very large gyroresonance fraction. They use a 21-day Gaussian smoothing on the 21-day sliding minimum series to determine the background component (Dudok De Wit & Bruinsma 2011) and define the variable component as the difference between the observations and this background. This naturally selects for only the rotational modulation component of $F_{10.7}$ that is dominated by large active regions. This will tend to remove the bremsstrahlung contribution from active regions since it is more evenly distributed in the corona than gyroresonance emission from active region cores directly above sunspots. Their data processing will tend to highlight the gyroresonance contribution, even though

Figure 6.2 suggests there is more bremsstrahlung most of the time.

In Chapter 4 the bremsstrahlung and gyroresonance emission for the single imaging observation was found and it is instructive to compare those results with the findings for that same day from this disk-integrated analysis. The predicted bremsstrahlung component calculated from AIA images is 77.7 ± 0.1 sfu[1] while the prediction from the MEGS-A spectra is 52 ± 8 sfu. This is a large discrepancy. Despite the spatially resolved nature of the AIA DEMs, the MEGS-A DEMs are much more reliable since they are based on the resolved spectral data rather than the narrow band (and spectrally complex) AIA images. This overestimation of the bremsstrahlung images suggests that the Chapter 4 results may underestimate the gyroresonance contribution. As expected, the spectral time series predicts 35 ± 8 sfu of gyroresonance compared to the 6.2 ± 0.3 sfu found from the imaging analysis. It is important to note that the imaging analysis disregards any chromospheric contribution to $F_{10.7}$ and attempts to remove its contribution by performing a background subtraction from each active region. This step, coupled with the constant chromosphere assumption made here, could also lead to underestimation of the gyroresonance emission observed in the $F_{10.7}$ image.

6.1.1. Rotational Modulation of the $F_{10.7}$ Bremsstrahlung Component

One of the interesting results from Chapter 4 is the diminished $F_{10.7}$ from active regions on the limb. This is interpreted as an optical depth effect, with microwave emission from behind the limb blocked by interceding chromospheric

[1]Recall from the discussion in Chapter 4.4.3 that the true uncertainty is much larger than the quoted value since there are $\sim 20\%$ systematic effects that aren't included. This suggests a true uncertainty of ~ 16 sfu.

and transition region plasma that remains optically thin in the EUV. Measurements of the EUV limb suggest that it is 1300 ± 650 km (Zhang et al. 1998) or 0.0019 ± 0.001 $R_\odot$ above the photosphere near the equator (and more at the poles). The microwave limb is frequency dependent due to the quickly changing optical depth caused by the solar atmospheric density profile. At 17 GHz, the solar limb is $16 \pm 1''$ or 0.017 ± 0.001 $R_\odot$ above the photosphere with a cycle amplitude of about $4''$ increase during solar maximum over solar minimum (Selhorst et al. 2011). At 2.8 GHz this limb extension is quite variable with a minimum of about $30''$ (Gary 1996) or 0.031 $R_\odot$.

It is a simple geometric problem to determine the signal delay from a coronal source on the Sun between when it becomes visible in the EUV and in $F_{10.7}$. A schematic of the viewing geometry is shown in Figure 6.4. The time delay between when a source becomes visible in the EUV and $F_{10.7}$ is given by

$$\Delta t = \frac{P\Delta\theta}{2\pi} = \frac{P\left(\theta_1 - \theta_2\right)}{2\pi} \tag{6.2}$$

where P is the rotation period. From the top-down schematic it is clear that

$$\cos\left(\theta_1\right) = \frac{r_{\mathrm{EUV}}}{r_{\mathrm{s}}} \qquad \text{and} \qquad \cos\left(\theta_2\right) = \frac{r_{\mathrm{F10.7}}}{r_{\mathrm{s}}} \tag{6.3}$$

and therefore

$$\Delta t = \frac{P}{2\pi}\left(\arccos\left(\frac{r_{\mathrm{EUV}}}{r_{\mathrm{s}}}\right) - \arccos\left(\frac{r_{\mathrm{F10.7}}}{r_{\mathrm{s}}}\right)\right). \tag{6.4}$$

This expression is true for sources with latitude $\phi = 0$ (above the equator) and the face-on view suggests how this changes for $\phi \neq 0$. In this case, what matters is not the radius of the solar disk but the projection of that radius along the radius

of the source. These projections are

$$r_{\mathrm{EUV}\ \phi} = \sqrt{r_{\mathrm{EUV}}^2 - \left(r_{\mathrm{s}} \sin\left(\phi\right)\right)^2} \qquad \text{and} \qquad r_{\mathrm{F10.7}\ \phi} = \sqrt{r_{\mathrm{F10.7}}^2 - \left(r_{\mathrm{s}} \sin\left(\phi\right)\right)^2}. \tag{6.5}$$

Substituting these into equation 6.4 yields

$$\Delta t\left(\phi\right) = \frac{P}{2\pi}\left(\arccos\left(\frac{\sqrt{r_{\mathrm{EUV}}^2 - \left(r_{\mathrm{s}} \sin\phi\right)^2}}{r_{\mathrm{s}} \cos\phi}\right) - \arccos\left(\frac{\sqrt{r_{\mathrm{F10.7}}^2 - \left(r_{\mathrm{s}} \sin\phi\right)^2}}{r_{\mathrm{s}} \cos\phi}\right)\right). \tag{6.6}$$

This equation assumes a constant rotation period and that the solar rotation axis is perpendicular to the Earth-Sun line, i.e. $B_0 = 0$. In fact, the differential rotation of the Sun is stratified by latitude and B_0 reaches $\pm 7.23\,\mathrm{deg}$ during a year. These will only cause $\sim 10\%$ corrections to equation 6.6 and can be ignored for this analysis.

Equation 6.6 can predict the time delay as a function of source height for various latitudes shown in Figure 6.5. This plot is made assuming solid body rotation with a synodic period of 27.2753 days (i.e. Carrington rotation) and setting $r_{\mathrm{EUV}} = 1.0025\ \mathrm{R}_\odot$ and $r_{\mathrm{F10.7}} = 1.03\ \mathrm{R}_\odot$. Moving to higher latitudes causes longer delays as the effective difference between EUV and $\mathrm{F}_{10.7}$ optically thick disks increases at higher latitudes. At low latitudes increasing the source altitude causes a monotonically decreasing delay time because of the increased lever arm of rotation. At higher latitudes this increasing altitude actually reverses the trend, eventually leading to increased delay times as the source approaches an altitude where it is never occulted by the EUV disk. Fundamentally, this analysis shows that the relatively small difference between the EUV and $\mathrm{F}_{10.7}$ limb altitudes leads to delay times of less than a day.

In order to investigate this signal in the time series sampled daily, the five

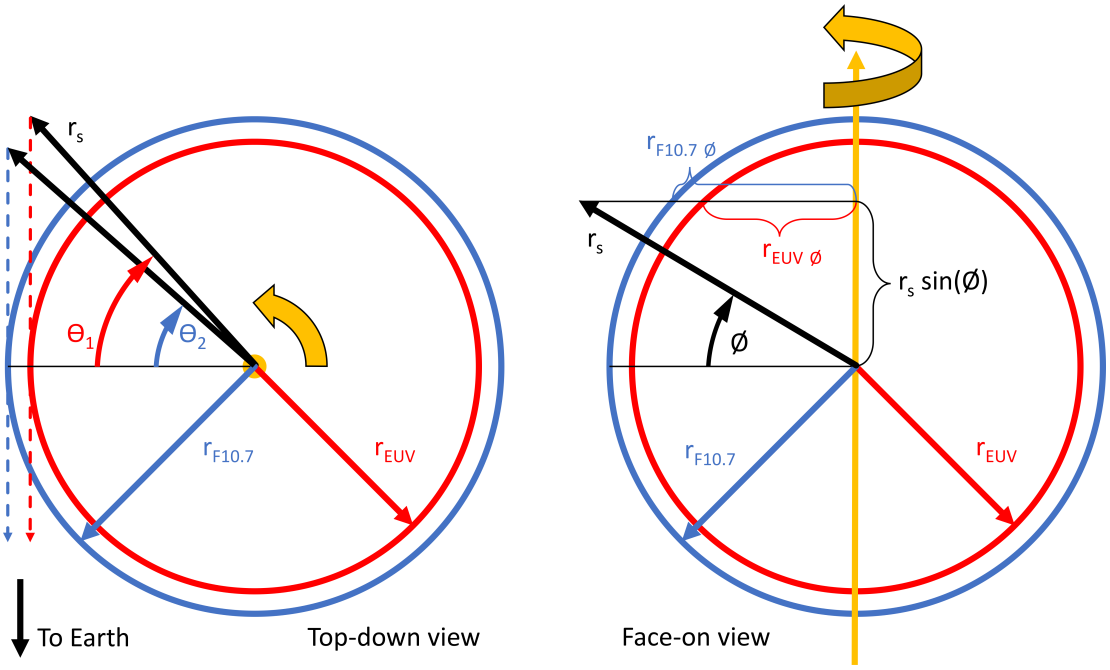

Fig. 6.4.— Geometric schematics describing the EUV-$F_{10.7}$ signal delay for *left:* a top-down view (from the solar north pole) and *right:* a face-on view from the Earth. In each schematic the gold arrow indicates the direction of solar rotation. The EUV and $F_{10.7}$ optically thick disks are $r_{\rm EUV}$ and $r_{\rm F10.7}$, respectively, and the radius of an arbitrary $F_{10.7}$ and EUV source is $r_{\rm s}$. The top-down view shows how a source rotating from behind the Sun will become visible in the EUV at time t_1 with corresponding rotation angle θ_1 before it becomes visible in the microwave at time t_2 and angle θ_2. The face-on view shows how the latitude ϕ of the source influences the effective EUV and $F_{10.7}$ projected disk radii, $r_{{\rm EUV}\ \phi}$ and $r_{{\rm F10.7}\ \phi}$.

most stable solar rotations are plotted in Figure 6.6. These series have been scaled to the same variation amplitude to facilitate comparison. The delays identified above suggest a systematic trend where there should be more bremsstrahlung emission predicted than is actually visible on the disk at all times because there is always more plasma visible in the EUV than at $F_{10.7}$. This might be observable because the bremsstrahlung series should be systematically greater during the transition between the minimum and maximum of each rotation (when bright sources are actively rotating around the limb) leading to narrower minima and broader maximum than are observed in the $F_{10.7}$ series. Unfortunately, the relatively larger

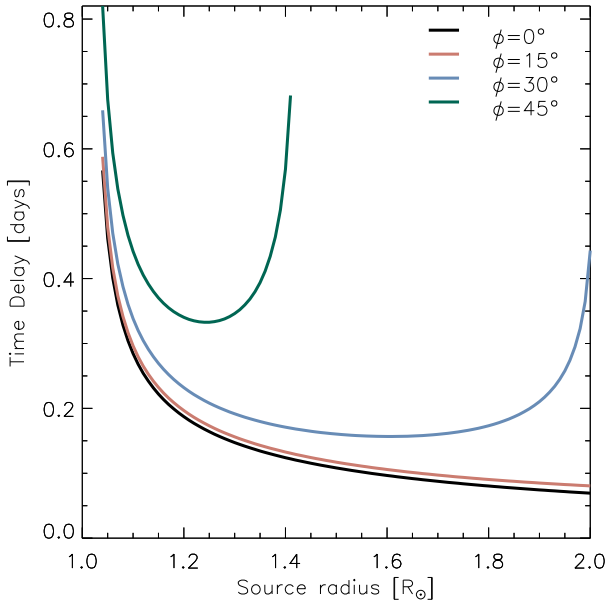

Fig. 6.5.— Theoretical relationships between the height of an emission source and the time delay between its visibility in the EUV and in $F_{10.7}$. This plot is made using equation 6.5 with $P = 27.2753$ days, $r_{\rm EUV} = 1.0025$ $R_\odot$, and $r_{\rm F10.7} = 1.03$ $R_\odot$ and is plotted for four different source latitudes: $\phi = 0°$, 15°, 30°, and 45°. The low altitude cutoff is set by $r_{\rm F10.7}$ (the height of the $F_{10.7}$ limb) and the high altitude cutoff is set by the altitude at which the source is never behind the EUV limb.

errors in the bremsstrahlung prediction coupled with the sub-resolution nature of the expected effect means that it is not visible in this data. It is possible that averaging over the entire time series might reveal a systematic time delay, but it would be difficult to disentangle this effect from other sources of solar variability. This systematic delay will likely only be observable with sub-day temporal resolution and spatially resolved measurements to identify individual source regions unambiguously.

6.1.2. $F_{10.7}$ Components and Photospheric Magnetic Fields

Henney et al. (2012) developed a method to predict $F_{10.7}$ based on pho-

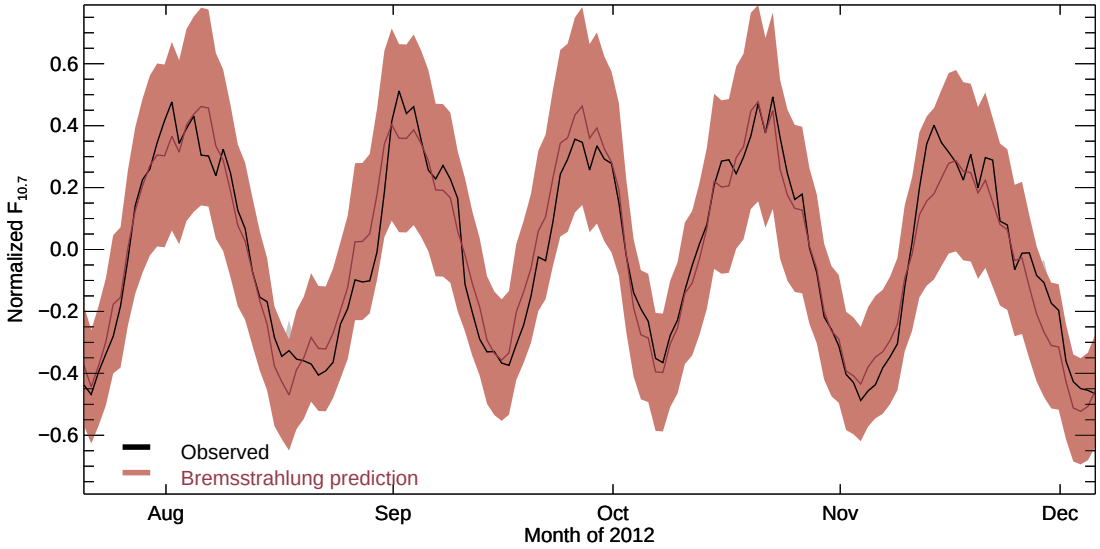

Fig. 6.6.— The observed $F_{10.7}$ and predicted bremsstrahlung time series during the five month period with the most regular rotational modulation. These series have been scaled to a mean of zero and normalized to a maximum variation of one.

tospheric unsigned radial magnetic fields. This involved parameterizing $F_{10.7}$ based on the area of photosphere covered by plage associated magnetic fields ($25 < \mathbf{B_r} < 150$) and sunspot fields ($\mathbf{B_r} \geq 150$). It is reasonable to expect that this parameterization would naturally separate the bremsstrahlung and gyroresonance components since bremsstrahlung emission is associated with active regions and their surroundings above chromospheric plage magnetic fields while gyroresonance is caused by the strong magnetic fields above sunspots in active region cores. They found temporally variable but approximately equal contribution from each of the two components, slightly more potentially gyroresonance associated emission than the findings of Chapter 6.1.

The bremsstrahlung and gyroresonance components identified through this analysis are compared with the Henney et al. (2012) magnetically identified plage and active region $F_{10.7}$ in Figure 6.7. The top-left plot is a measure of how

well this magnetic field parameterization characterizes the observed $F_{10.7}$. The parameterization during this period is good, but not at the R$\sim$ 0.97 level found for the earlier 17 year period analyzed in Henney et al. (2012). All other panels except the center and bottom right should show relatively poor correlations since they compare the wrong component of the emission with the underlying magnetic fields.

The center and bottom right plots are expected to correlate very well if the plage and active region magnetic fields are actually related to bremsstrahlung and gyroresonance emission, respectively. The correlation of the bottom right plot is very good, matching the slope and amplitude of the emission well. This means the gyrorenance emission is largely determined by the presence of strong magnetic fields. However, the scatter of the outliers, especially at higher activity levels is quite large, suggesting that there is some decoupling between the underlying magnetic fields and the actual gyroresonance emission. The relationship between the bremsstrahlung prediction and the plage fields has very little scatter at all activity levels, but is offset significantly, with more predicted bremsstrahlung emission than expected based on the plage fields. However, the parameterization used by Henney et al. (2012) assumed a solar constant level of 65 sfu, significantly more than the 52 sfu constant chromospheric component determined in Chapter 6.3.2. If the difference between these constant backgrounds is entirely due to bremsstrahlung emission (which is likely given the stable solar minimum bremsstrahlung emission shown in Figure 6.1) it would shift this distribution to the right directly onto the line of equality.

It is also valuable to investigate a larger magnetic field strength range given the properties of gyroresonance emission. Gyroresonance emission requires coronal

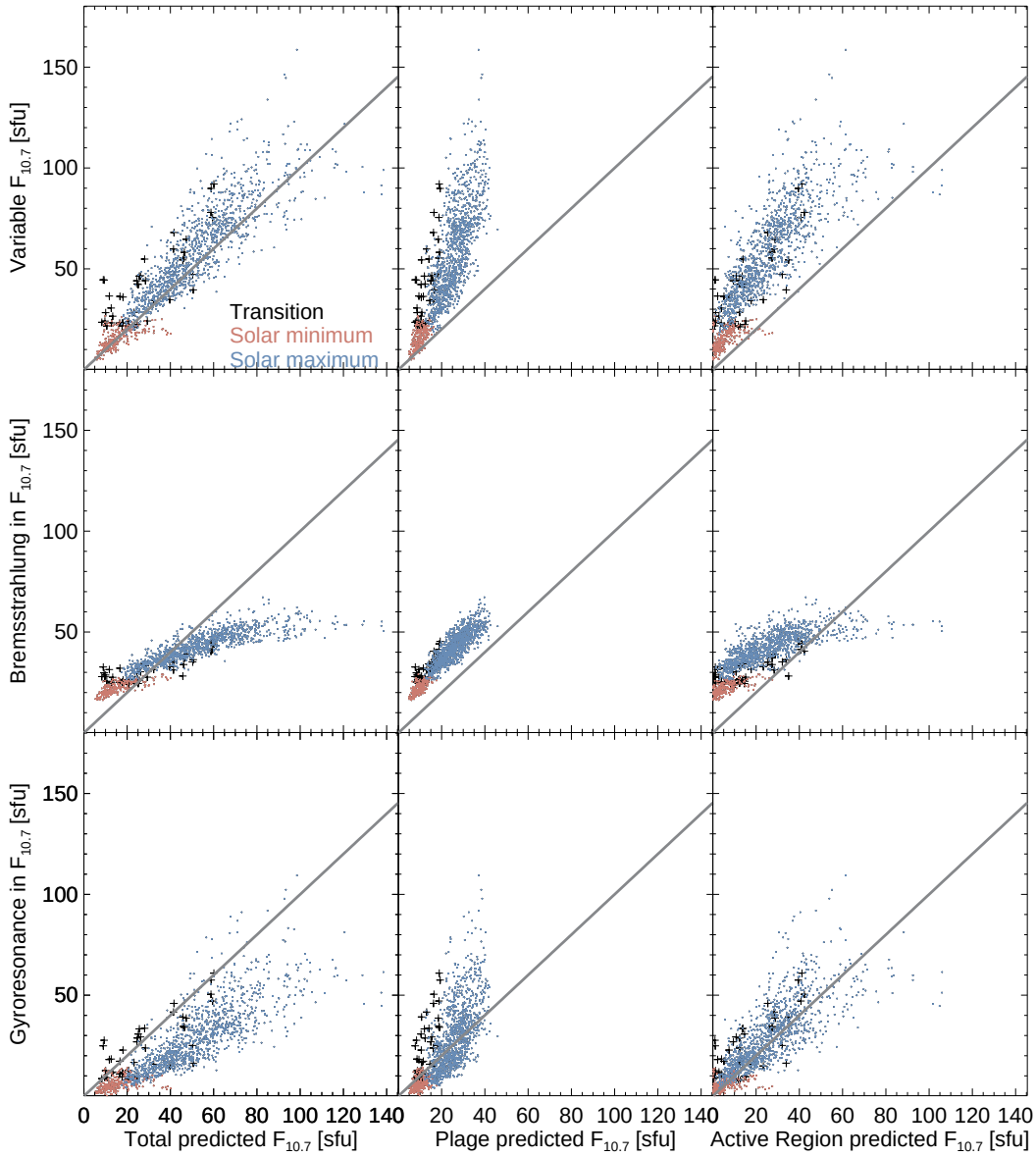

Fig. 6.7.— The observed *top:* variable $F_{10.7}$, *middle:* bremsstrahlung, and *bottom:* gyroresonance components vs. the predicted *left:* total, *center:* plage, and *right:* active region components of the $F_{10.7}$ predictions from Henney et al. (2012). The diagonal gray line in each panel indicates where the observation equals the prediction. The plage component is calculated from the area of photospheric magnetic fields with magnitudes of $20 < B_r < 150$ G while the active region component is calculated from the area of fields with $B_r \geq 150$. The plots on the diagonal (top left to bottom right) should show good agreement while the others are expected to deviate from the gray lines. The point colors indicate the time series splitting identified in Chapter 5.4.1 and plotted in Figure 5.12.

magnetic field strengths of at least 250 G for emission from the fourth harmonic and 333 G from the third harmonic (see Chapter 2.2.2). Therefore the 150 G photospheric field cutoff is not the best threshold to uniquely identify gyroresonance emission. In Figure 6.8 the gyroresonance emission is plotted against the magnetic field parameters for four different field strength ranges that are more meaningful for identifying gyroresonance emission. The gyroresonance correlates most strongly with the area of field with strengths $150 \leq B_r < 500$. This photospheric strength range is likely to result in the coronal fields necessary for third and fourth harmonic emission. It is a little surprising that the correlation with the $300 \leq B_r < 500$ field isn't the largest since the field strength decays from the photosphere into the corona and fourth harmonic gyroresonance emission requires $B_r = 250$. However, the correlation between magnetic fields themselves (i.e. the presence of strong fields requires the presence of weak fields) likely causes the relatively similar correlations between gyroresonance and both stronger and weaker fields.

The same relationships but comparing the bremsstrahlung emission are plotted in Figure 6.9. This shows that, as expected, the bremsstrahlung emission correlates most strongly with the weakest magnetic fields. Interestingly, the bremsstrahlung component correlates nearly as well with the $300 \leq B_r < 500$ as does gyroresonance. This is likely due to the correlation between magnetic fields and the relative inconsistency of gyroresonance emission rather than the intrinsic relationship between bremsstrahlung emission and these relatively strong magnetic fields.

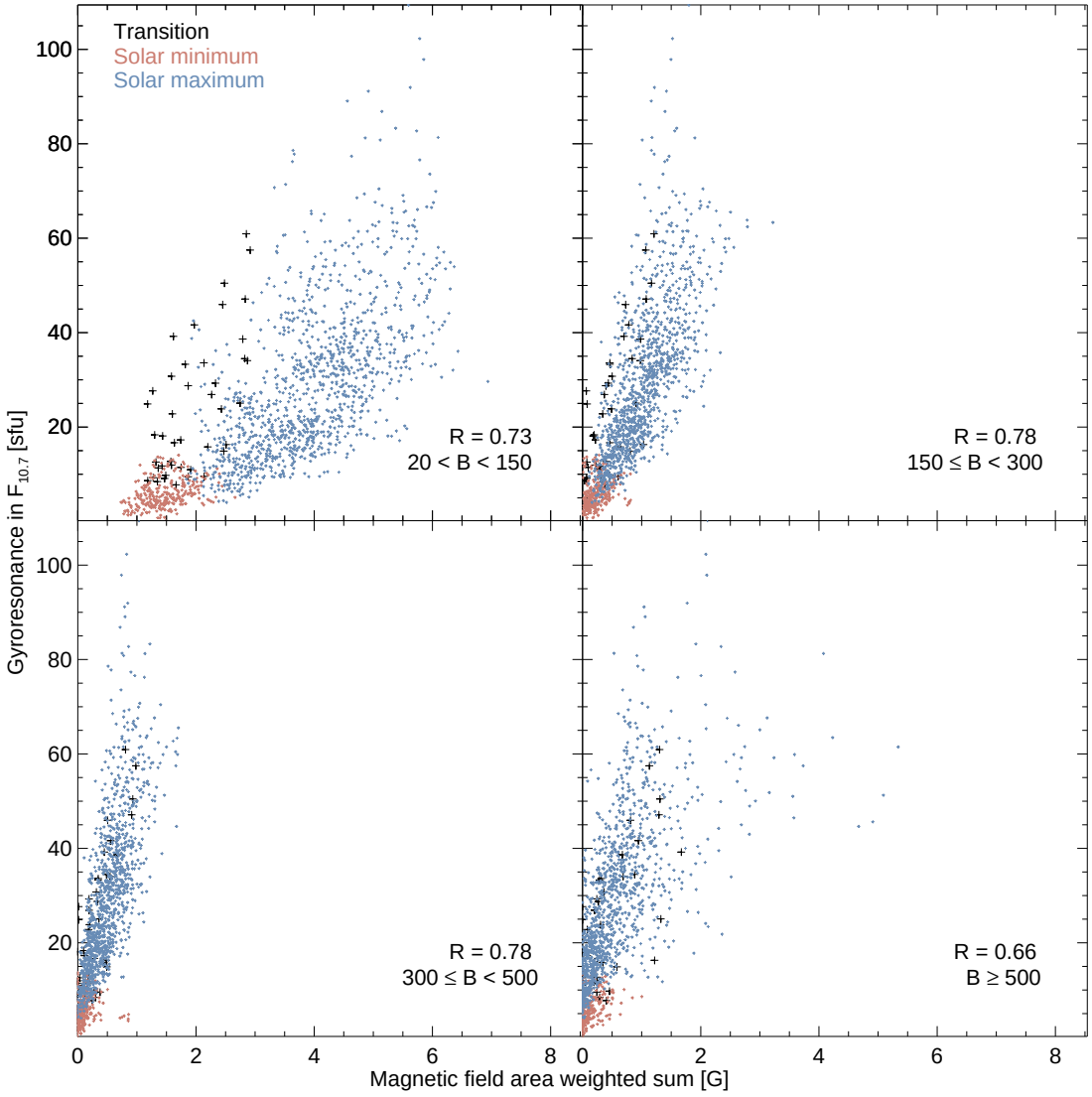

Fig. 6.8.— The correlation between the $F_{10.7}$ gyroresonance component implied by the MEGS-A DEMs with the photospheric magnetic fields from Henney et al. (2012). Each panel indicates the included magnetic field strengths and the linear correlation coefficient. The gyroresonance emission correlates most strongly with the $150 \leq B_r < 500$ G magnetic fields. The point colors indicate the time series splitting identified in Chapter 5.4.1 and plotted in Figure 5.12.

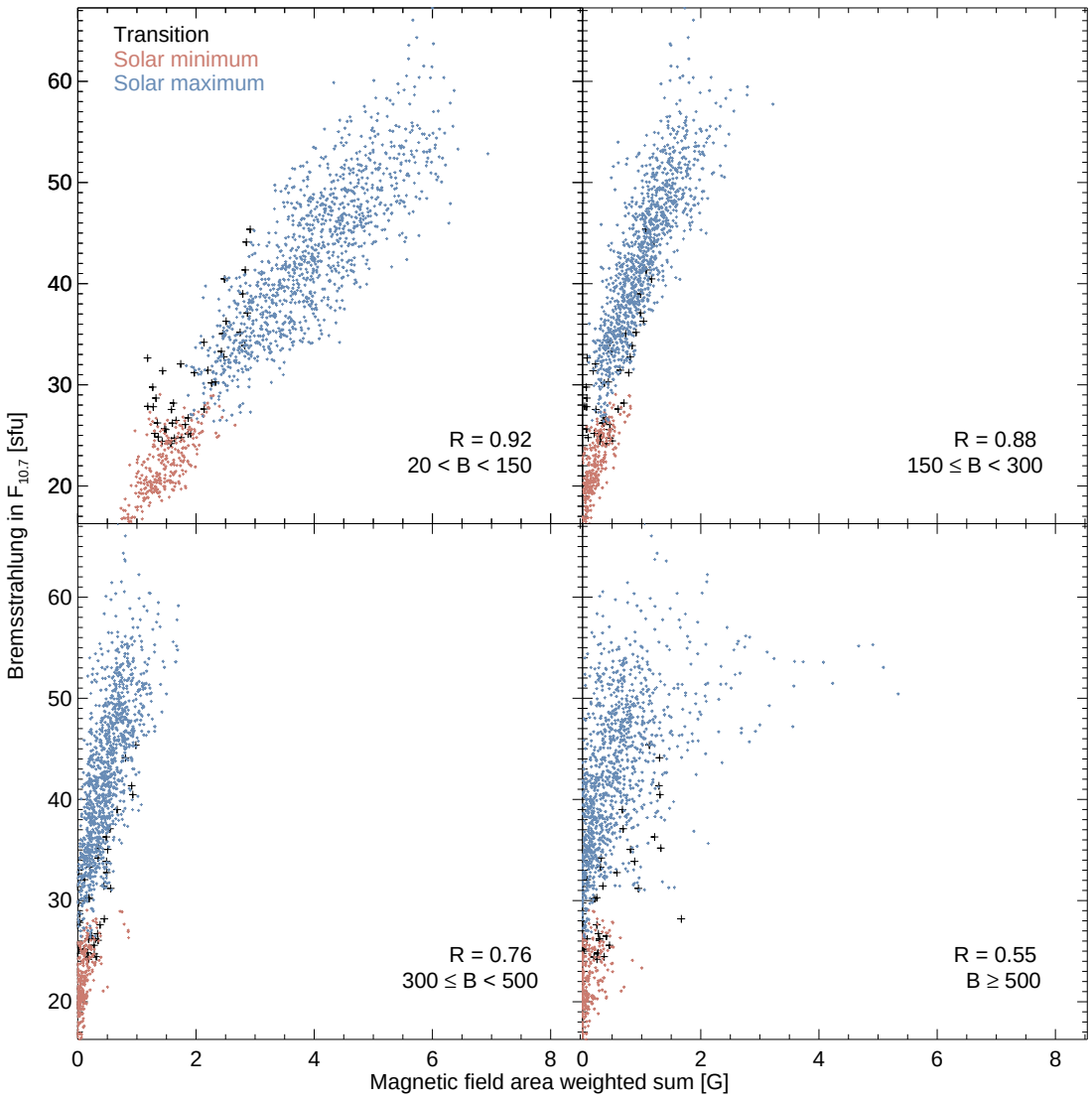

Fig. 6.9.— The same as Figure 6.8 but for the $F_{10.7}$ bremsstrahlung component computed from the MEGS-A DEMs. The bremsstrahlung correlates most strongly with the weaker magnetic fields associated with chromospheric plage on the outskirts of active regions.

6.2. Correlation of $F_{10.7}$ and the Bremsstrahlung Component

Previous work has identified that the relationship between EUV and $F_{10.7}$ becomes nonlinear during periods of intense solar activity (e.g. Balan et al. 1993), an observation termed the "saturation effect" (Girazian & Withers 2015). Since the bremsstrahlung component is calculated from DEMs derived from EUV data, this same nonlinearity at high activity levels should be present. Figure 6.10 shows that this is indeed the case. While the bremsstrahlung component has a tight linear relationship with the observed $F_{10.7}$ during periods of low activity, the scatter increases and the linearity is broken at high activity levels. This bremsstrahlung emission is fit with a smooth piecewise continuous function that is linear at low activity levels and a power law at high activity. This takes the form of

$$F_{Bremsstrahlung} = \begin{cases} a + bF_{10.7}, & \text{for } F_{10.7} < c \\ d\left(F_{10.7} - e\right)^{f}, & \text{for } F_{10.7} \geq c \end{cases} \tag{6.7}$$

where $a = -25.1 \pm 1.1$, $b = 0.592 \pm 0.013$, $c = 96$, $d = 13.9 \pm 1.2$, $e = 80$, and $f = 0.297 \pm 0.019$[2]. This is clearly different from the averaged $F_{10.7}$ that is typically used (the black points) and that closely approximates the canonical assumed linear relationship with EUV. Notice though that the scatter in these two formulations is similar. This means that the variability of the bremsstrahlung contribution at a constant activity level is about as large as the variability in the implied geoeffectivness of the 81-day averaged $F_{10.7}$ series.

[2]Requiring continuity and smoothness (continuous first derivative) in this functional form provides two constraints to the fit. This means that c and e are uniquely determined by the other best fit parameters and don't have errors

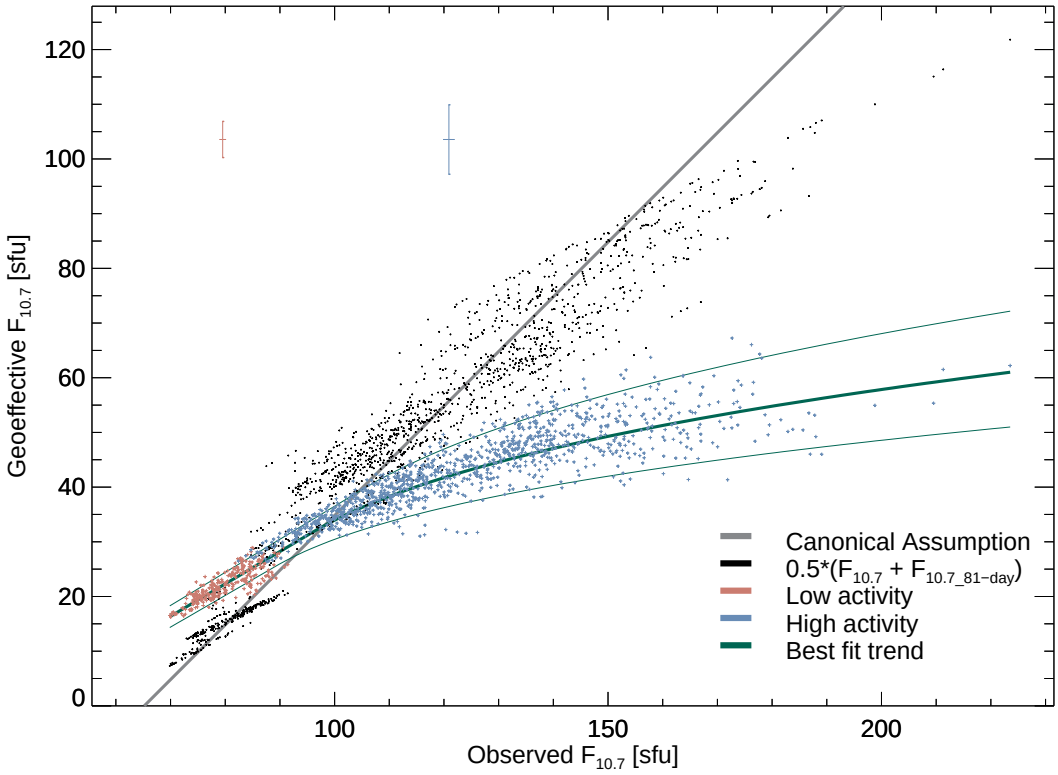

Fig. 6.10.— The relationship between the observed and geoeffective $F_{10.7}$. The red and blue points indicate the predicted bremsstrahlung component of $F_{10.7}$ color coded based on the time series splitting identified in Chapter 5.4.1 and plotted in Figure 5.12. The red and blue crosses are characteristic error bars for their corresponding points. The thick (thin) green line indicates the best fit (1σ error) model of this relationship, with a smooth piecewise continuous relationship between a linear trend at low activity and a power law at high activity. The black points indicate the typical formulation of $F_{10.7}$ used for atmospheric modeling, with an average of the daily observation with the 81-day centered average (equation 6.8). The gray line indicates the canonically assumed relationship, that $F_{10.7}$ above the observed solar minimum level is linearly related with solar EUV emission.

6.2.1. Parameterization of EUV

The fundamental purpose of this investigation is to better understand $F_{10.7}$ as an EUV proxy. It is valuable, therefore, to apply the above parameterization and compare its predictive capability with the standard implementation of $F_{10.7}$. One common use of $F_{10.7}$ is in the EUV flux model for Aeronomic Calculations (EUVAC, Richards et al. 1994). This model uses $F_{10.7}$ to linearly scale the EUV fluxes in 37 low resolution bins (called Stan Bands after Stan Solomon, Solomon & Qian 2005) between solar minimum and maximum observations. It uses the standard $F_{10.7}$ average such that

$$F^a_{10.7} = \frac{1}{2}\left(F_{10.7} + F_{81}\right) \tag{6.8}$$

where F_{81} is the 81-day centered average of the $F_{10.7}$ series. This parameterization tempers the large variability of the 27-day rotational modulation with the slowly varying 81-day average. Intuitively, this should tend to remove the contributions from the highly variable gyroresonance emission while keeping the majority of the relatively stable bremsstrahlung emission. However, this averaging also boosts the apparent $F_{10.7}$ during rotational minima which would overestimate the level of solar activity.

In order to evaluate the performance of the bremsstrahlung parameterization (equation 6.7) its correlation with the Stan Band measurements covering the MEGS-A spectral range is compared to the correlation of $F^a_{10.7}$ with those same measurements. This is shown in Figure 6.11. The different slopes of the two activity proxies simply indicate different proportionalities. The importance of these plots is the correlation quality that is nearly the same for these two activity proxies in each spectral band. This indicates that the bremsstrahlung parameterization

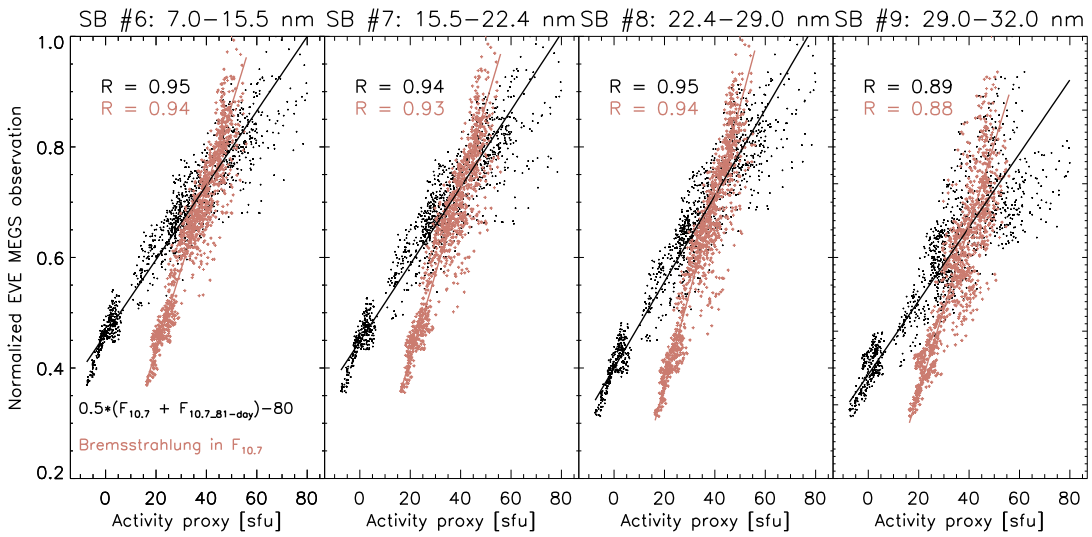

Fig. 6.11.— The comparisons between the normalized observed EUV flux and the $F^a_{10.7}$ (black) and bremsstrahlung (red) proxies for the four Stan Bands observed by the EVE MEGS-A spectrograph. The best-fit lines and linear correlation coefficients are indicated in each panel. $F^a_{10.7}$ slightly outperforms the prediction from the bremsstrahlung component in each band.

is about as good (although slightly worse) than the common $F^a_{10.7}$ series. This means that the intrinsic variability in the relationship between $F_{10.7}$ and EUV (i.e. the bremsstrahlung fraction in Figure 6.3) is large enough that it is captured just as well by the empirical $F^a_{10.7}$ averaging as by the physically motivated best fit bremsstrahlung component. Importantly though, the bremsstrahlung fit is much preferred from an operational space weather perspective as it requires only the daily observation rather than relying on averaging data 40 days into the future.

This comparison can also be expanded to a larger EUV spectral range by comparing with the Stan Bands observed by the Solar EUV Experiment (SEE) that makes spectral measurements between 1 and 195 nm (10–1950 Å) on the NASA Thermosphere, Ionosphere, and Mesosphere Energetics and Dynamics (TIMED) spacecraft (Woods et al. 2000). This allows for a comparison from the MEGS-

A spectral range all the way up to Lyman-α and these 16 bands are shown in Figure 6.12. In this spectral range $F^a_{10.7}$ performs marginally better than the bremsstrahlung proxy. This may partly be due to the fact that the bremsstrahlung series is derived from the MEGS-A data, so it should be expected to perform best when compared with that data set. Additionally, these longer wavelength EUV bands have significant contribution from chromospheric emission (e.g. H I and He I continua in Figure 2.2) that will still correlate with $F_{10.7}$ (see the discussion of Chapter 6.4.2) but less well with coronal bremsstrahlung emission. One interesting effect leading to the weaker correlation between the bremsstrahlung proxy and the TIMED/SEE Stan Bands is the apparent broadening of the distribution at low activity levels. This creates a double series similar to what is seen in Chapter 5.4.1. However, since each of these bands has a large spectral range there is no clear temperature difference between the EUV band and the bremsstrahlung prediction and hence no obvious explanation for this effect.

The result of this analysis is that while the bremsstrahlung proxy has the advantage of being derived from a single day of observation, the $F^a_{10.7}$ proxy performs marginally better, especially at longer EUV wavelengths. The reason they both perform so similarly can be seen from Figure 6.10. Even though the slopes of the distributions are different, the 81-day averaging smears the $F_{10.7}$ series and gives the two distributions very similar shapes.

6.3. Multi-frequency Considerations

The same analysis performed in Chapter 6.1 can be repeated for any microwave time series, and another prominent set of observations are those of the

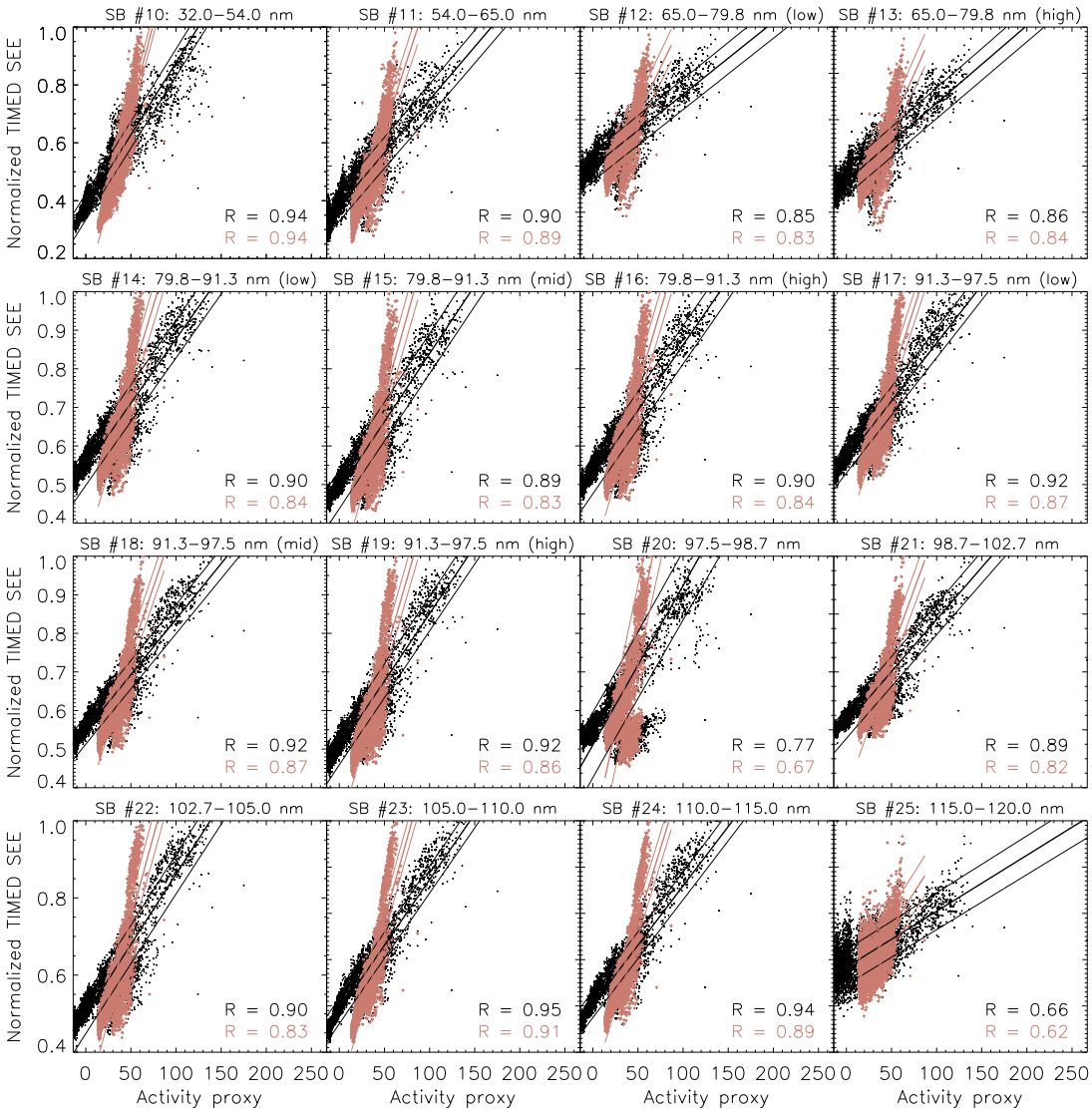

Fig. 6.12.— The same as Figure 6.11 but for the Stan Bands observed by the TIMED SEE instrument. In this longer wavelength EUV spectral range, the $F_{10.7}$ parameterization marginally outperforms the bremsstrahlung prediction in all bands. The bremsstrahlung proxy appears to saturate at high levels of activity in all bands.

Nobeyama Radio Polarimeters (NoRP, Tanaka & Kakinuma 1957; Torii et al. 1979). The NoRP record the solar irradiance daily at Japan local noon (3 UT) at 1.0, 2.0, 3.75, 9.4, 17.0, 35.0, and 80.0 GHz. For the three highest frequency observations, atmospheric absorption due to O_2 and H_2O vapor causes seasonal variations (Tsuchiya & Nagane 1965, Kazumasa Iwai private communication 6/6/2017) and therefore only the 1.0, 2.0, 3.75, and 9.4 GHz observations are suitable for a multi-year study. By interpolating these observations to 20 UT to match the EUV and $F_{10.7}$ series over the same time period, an analysis similar to what was done for $F_{10.7}$ can be performed at each frequency.

The observation, the constant chromosphere, the DEM bremsstrahlung component, and the corresponding gyroresonance emission are shown in Figure 6.13 for each of the four NoRP time series. The most notable feature is the strong frequency dependence of the observations that is largely caused by the increasing contribution of the optically thick chromosphere. This is due to the frequency dependence of blackbody radiation and is explained fully in Chapter 6.3.1. The predicted bremsstrahlung component of each series is nearly identical due to the very weak frequency dependence of optically thick bremsstrahlung emission, and this means that the difference in the shape of the time series observations at different frequencies is due almost entirely to the gyroresonance component.

The implied gyroresonance emission is re-plotted for all five frequencies in Figure 6.14 to highlight its statistical significance. This shows the calculated gyroresonance emission in black with the associated 1σ error region (calculated from the error in the observations, the bremsstrahlung prediction, and the determination of the chromospheric constant) plotted around zero. This shows a strong correlation between the gyroresonance emission at all frequencies, but the largest

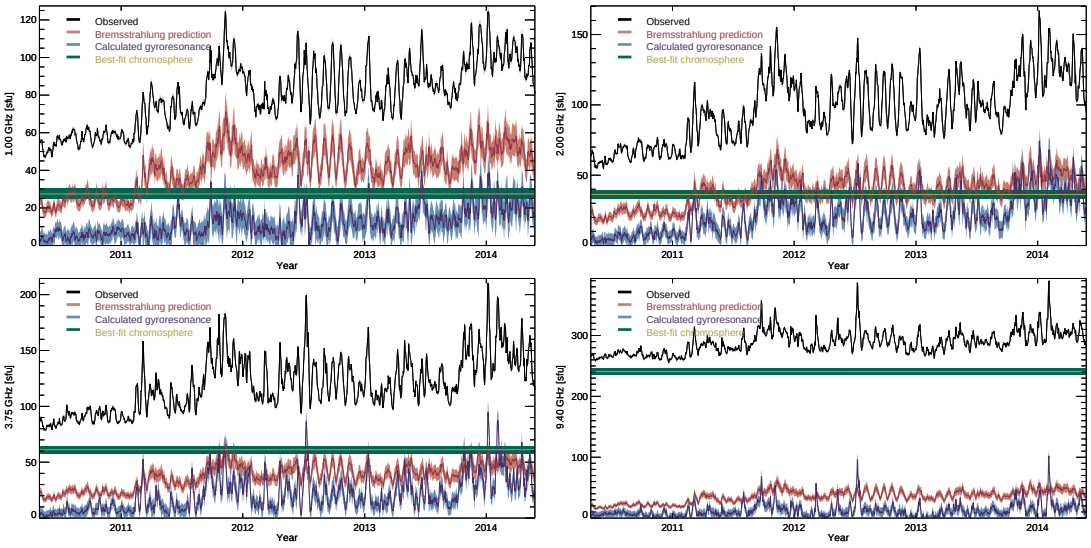

Fig. 6.13.— The same as Figure 6.2 but for the four NoRP frequencies. The chromosphere series are the best-fit constant chromospheric components as described in Chapter 6.3.2.

sustained amplitudes in the middle frequencies. This also shows that there is relatively little statistically significant gyroresonance near solar minimum (i.e. during 2010) but significant emission at all times during solar maximum, 2011–2014.

One important feature of gyroresonance emission is its spectral signature, a peak in the 1–5 GHz range (Piddington & Minnett 1951; Kundu 1965), in contrast to the $\nu^{-0.1}$ dependence of optically thin bremsstrahlung emission (from the Gaunt factor in equation 2.3). This has been used by Schmahl & Kundu (1995, 1998) to identify gyroresonance emission from low resolution irradiance microwave spectra observed with the NoRP. In the following sections a similar spectral analysis is performed to compare spectrally identified emission components to those found with the DEM analysis.

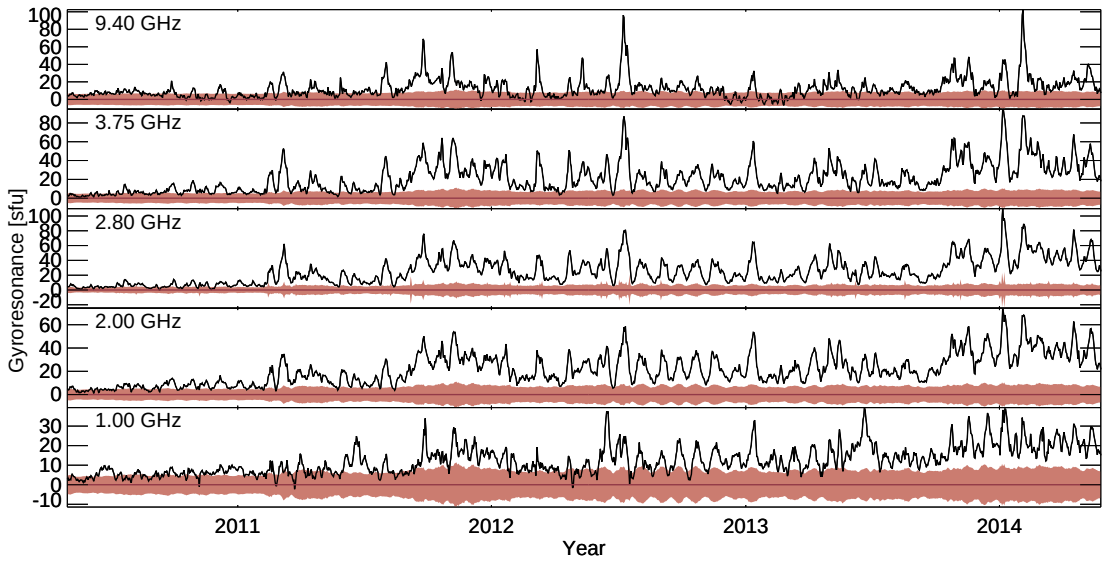

Fig. 6.14.— The time series of the gyroresonance component identified using the DEMs in black with the 1σ error regions highlightsed around the origin in red. Gyroresonance predictions consistently above error envelope (over a singele rotation) indicate a statistically meaningful gyroresonance emission component.

6.3.1. First-pass Spectral Fitting

Splitting the three emission mechanisms (optically thick bremsstrahlung emission from the chromosphere, optically thin coronal bremsstrahlung, and optically thick coronal gyroresonance) relies on the known spectral characteristics of the coronal emission sources. Additionally, the optically thick bremsstrahlung emission from the solar disk emits as a black body which, in the Rayleigh-Jeans approximation of the long-wavelength limit goes as

$$B_\nu\left(T\right) = \frac{2\nu^2 k_\mathrm{B} T}{c^2}. \tag{6.9}$$

Because of the strongly varying optical depth with frequency, each microwave observation becomes optically thick at a different height and therefore observes blackbody emission from different temperature plasma. Specifically, since the optical depth decreases with frequency, higher frequency observations are sensitive

to emission from deeper into the solar atmosphere and therefore observe cooler blackbody backgrounds. This means that it is not possible to fit the optically thick chromospheric component with a single blackbody spectrum. Because of the ν^2 dependence of blackbody emission, even though higher frequency observations observe cooler sources they contain a larger optically thick emission component.

It is therefore necessary to make some assumptions about the optically thick emission component to interpret the microwave spectra. For a first-pass analysis it is assumed that during solar minimum all the observed emission is from the constant, optically thick, chromospheric background. This assumption is inaccurate but it is a simple starting point to refine later. Since the only other emission component during solar minimum should be optically thin coronal bremsstrahlung emission with a nearly flat spectrum, this assumption should have little effect on the ability to isolate spectral components. However, if coronal bremsstrahlung emission contributes during solar minimum, this assumption will cause this spectral analysis to underestimate the bremsstrahlung component at all times. A characteristic solar minimum value is determined for each of the five microwave time series (the four NoRP frequencies and $F_{10.7}$, 2.8 GHz) using their complete observation history, more than three cycles at each frequency. Each series is filtered to the 5^{th} percentile in an 81-day rolling window (not the minimum so as to easily ignore outliers) and then the minima of this series (one value per solar minimum of the 11 year cycle) are averaged to determine the typical solar minimum level. The standard deviation of the cycle minima provides a good estimate of the uncertainty in this average. This solar minimum spectrum (given in Table 6.1) is then subtracted from each observed spectrum to facilitate the identification of the coronal sources. The spectral fitting then proceeds as follows:

1. If the spectrum is consistent with zero then the emission can be completely explained by the solar minimum chromospheric component. Because the observation series started after the absolute minimum conditions this is never the case for this data set.

2. Fit the spectrum as pure bremsstrahlung emission with

$$f_\nu = C\nu^{-0.1} \tag{6.10}$$

   where C is a constant scale factor. If this is a good fit then the observations are considered pure bremsstrahlung emission. If the observations are not well explained by this pure bremsstrahlung component then the maximum bremsstrahlung component consistent with the observations (i.e. the bremsstrahlung spectrum that zeroes a single frequency with the remaining residuals positive) is assumed.

3. If only a single frequency observation is inconsistent (based on observational noise) with this bremsstrahlung fit then it is assumed this is an observational error and the spectrum is classified as containing bremsstrahlung emission and an unidentified residual component with no gyroresonance emission.

4. Otherwise the bremsstrahlung spectrum is subtracted and the remaining unfit spectral component is then fit with a skewed Gaussian. If this is a good fit to the remaining spectrum (i.e. the peak is observed and not outside the spectrum, the spectrum isn't over-fit with a very narrow skewed Gaussian, and there are one or fewer observations that deviate by more than their observational noise) then the spectrum is classified as containing bremsstrahlung and gyroresonance emission.

5. If the skewed Gaussian is not a good fit then the spectrum is classified as containing bremsstrahlung, gyroresonance, and an unidentified residual component.

This method is rather ad hoc, but care has been taken to tune the method to minimize false positive identification of clean spectra. Additionally, while there is no reason to expect a skewed Gaussian spectral shape from gyroresonance emission, the low resolution (with only a handful of observations) means that the true spectral shape of the fit is unimportant because the true spectrum is fundamentally under sampled. The asymmetric nature of the skewed Gaussian allows it to more flexibly fit these peaked spectra while also identifying cases where the peaks are not clean.

For this first-pass spectral fitting only the four NoRP frequencies are used since there are well identified (but small) normalization issues between different microwave observatories (Tanaka et al. 1973). The results of this spectral fitting are shown in the left plot of Figure 6.15. Each column contains the spectra identified with one of the four different spectral tags. Notice that there are some spectra that have unidentified residual components that might by eye be identified as clean bremsstrahlung and gyroresonance emission. The reverse is not true however, as all spectra identified without significant residuals appear consistent with the expected spectral shape (bremsstrahlung slightly decreasing and centrally peaked gyroresonance) to within the few percent errors associated with the flux observations. It is also important to notice that all the days with most intense emission are identified as containing gyroresonance contributions. These show the expected spectral peak of a few GHz, but due to the low resolution of the

spectra (and the unknown true spectral shape) it is not possible to constrain the peak frequency to better than 2–9.4 GHz. There are also a few spectra that are monotonically increasing with frequency, suggesting either much higher frequency gyroresonance peaks (possibly greater than 9.4 GHz) or significantly increased chromospheric emission (although this explanation is disfavored since blackbody emission goes as ν^2 and the spectra appear to be flattening at higher frequencies).

6.3.2. Constant Chromosphere Determination

It is possible to combine the DEM predicted bremsstrahlung emission with these spectral classifications to improve the determination of the constant optically thick chromospheric contribution. This is done by investigating the DEM predicted bremsstrahlung emission on days that have been spectroscopically identified as purely bremsstrahlung emission. Figure 6.16 has the same predicted bremsstrahlung versus the total observed flux as shown in Figure 6.10 but this time the points are color coded by the spectral classification with red indicating days with only bremsstrahlung emission. These points create a clear linear relationship that spans both the low and high activity period identified in Chapter 5.4.1. Extrapolating the best fit line back to the solar minimum value in Table 6.1 (the vertical gray line) gives the expected coronal bremsstrahlung emission during solar minimum (the horizontal gray line). Subtracting this from the solar minimum value gives the true constant chromospheric level.

This same analysis can be performed with each of the frequencies and the results are shown in Table 6.1 and Figure 6.17. This reveals several interesting trends. While the best-fit bremsstrahlung line is at the top of the distribution for

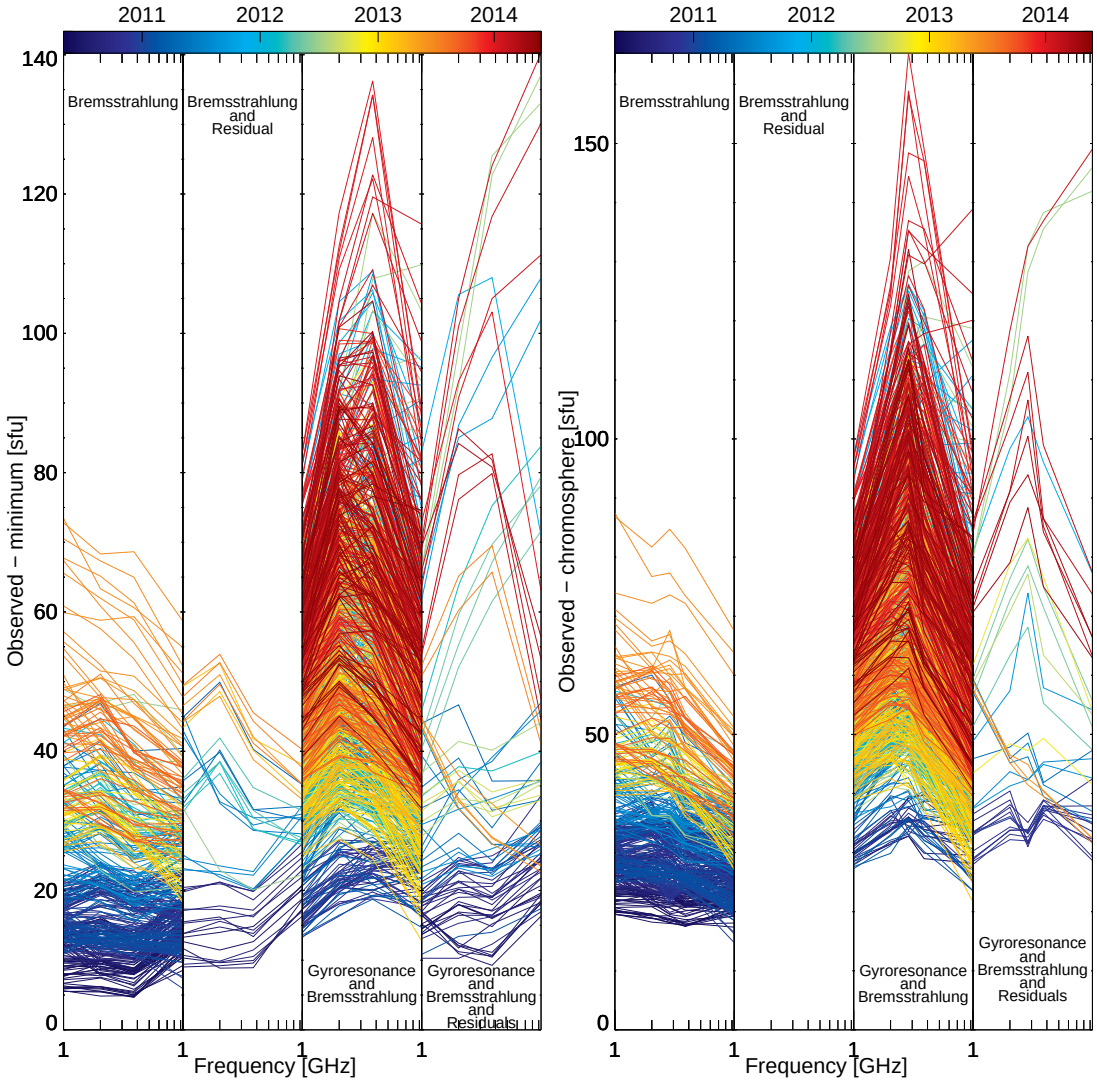

Fig. 6.15.— Microwave spectra identified based on their constituent components for *left:* subtraction of the solar minimum level using just the NoRP data and *right:* the best-fit chromospheric level using $F_{10.7}$ and the NoRP data. In each panel, each column identifies the constituent spectrally identified components. The color indicates the date of the observation. All the spectra from the most active periods (days with the most flux) contain gyroresonance emission.

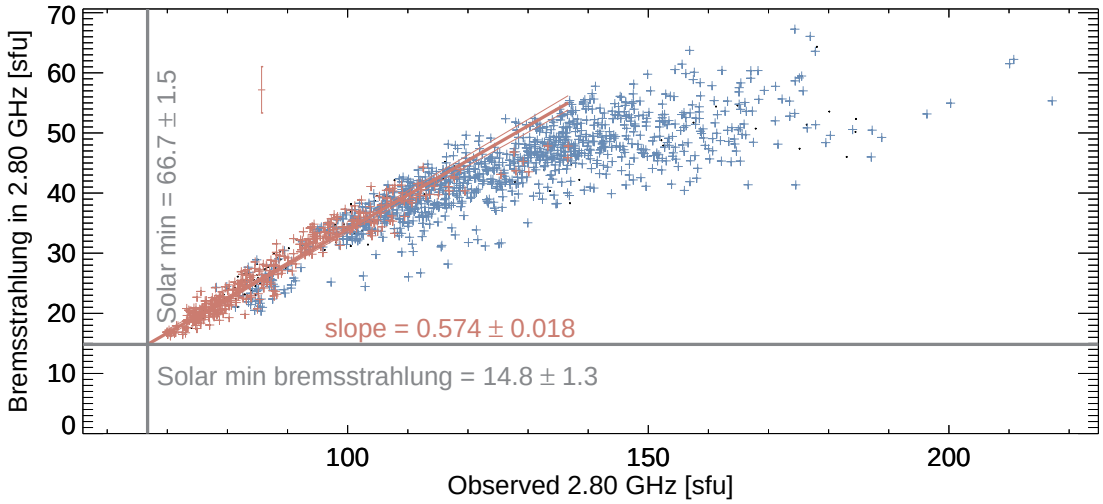

Fig. 6.16.— The predicted bremsstrahlung emission vs. the observed $F_{10.7}$. Points plotted in red are spectrally identified as purely bremsstrahlung, points in blue are spectrally identified as a combination of bremsstrahlung and gyroresonance, and points in black have residual unidentified emission components. The red cross indicates a characteristic error bar for the red points. The calculated solar minimum level, slope of the best linear fit to the bremsstrahlung only points, and the resulting solar minimum bremsstrahlung component are also shown.

Table 6.1. Microwave spectral time series parameters

Frequency [Hz]	Solar minimum [sfu]	Constant chromosphere [sfu]	Solar minimum bremsstrahlung [sfu]	Bremsstrahlung slope
1.0	41.5 ± 2.2	27.4 ± 2.9	14.0 ± 1.8	0.623 ± 0.020
2.0	49.7 ± 2.4	36.3 ± 3.1	13.4 ± 1.9	0.608 ± 0.019
2.8	66.7 ± 1.5	51.9 ± 2.0	14.8 ± 1.3	0.574 ± 0.018
3.75	74.0 ± 2.8	61.2 ± 3.6	12.8 ± 2.2	0.638 ± 0.021
9.4	249.6 ± 3.7	240.7 ± 5.1	8.8 ± 3.4	0.752 ± 0.029
Average	—	—	—	0.639 ± 0.067

Note. — Parameters of full-Sun microwave emission derived from long-term series observations and the DEM bremsstrahlung predictions.

the three central frequencies (as expected since points to the right of the line indicate gyroresonance emission and these central frequencies are near the peak of the gyroresonance emission), both the 1.0 and 9.4 GHz distributions show different trends. For 1.0 GHz, the bremsstrahlung points are actually at the bottom of the distribution and there is no clear non-linearity as expected for significant gyroresonance emission. One possible explanation for this is an optical depth effect. At 1.0 GHz, it is possible that the coronal bremsstrahlung emission becomes optically thick in large active regions. If this happens then the DEM bremsstrahlung prediction from EUV observations will be sensitive to plasma that is below the optically thick floor in the microwave and therefore it will suggest more bremsstrahlung emission than is actually observed. Additionally, this suggests that gyroresonance emission is rarely if ever observed at 1.0 GHz. At 9.4 GHz the bremsstrahlung trend cuts through the middle of the distribution until the very high activity level when the gyroresonance tail curves the distribution to the right. The points that show relatively more bremsstrahlung emission even on a day with gyroresonance emission might be due to the relatively small contribution of gyroresonance emission at 9.4 GHz coupled with possible chromospheric variability. This is discussed in Chapter 6.4.2. Additionally, the slopes of each of these distributions is similar but not one, a feature that is discussed in detail in Chapter 6.4.

Using these improved fits for the constant chromospheric component (instead of the observed solar minimum level) the microwave spectra are re-fit using the procedure described in Chapter 6.3.1. The observed $F_{10.7}$ is also included in the spectral fitting and the results are shown in the right plot of Figure 6.15. This time there are no spectra without gyroresonance emission that cannot be fit by a pure bremsstrahlung spectrum. Examining these spectra, it is clear that $F_{10.7}$ often

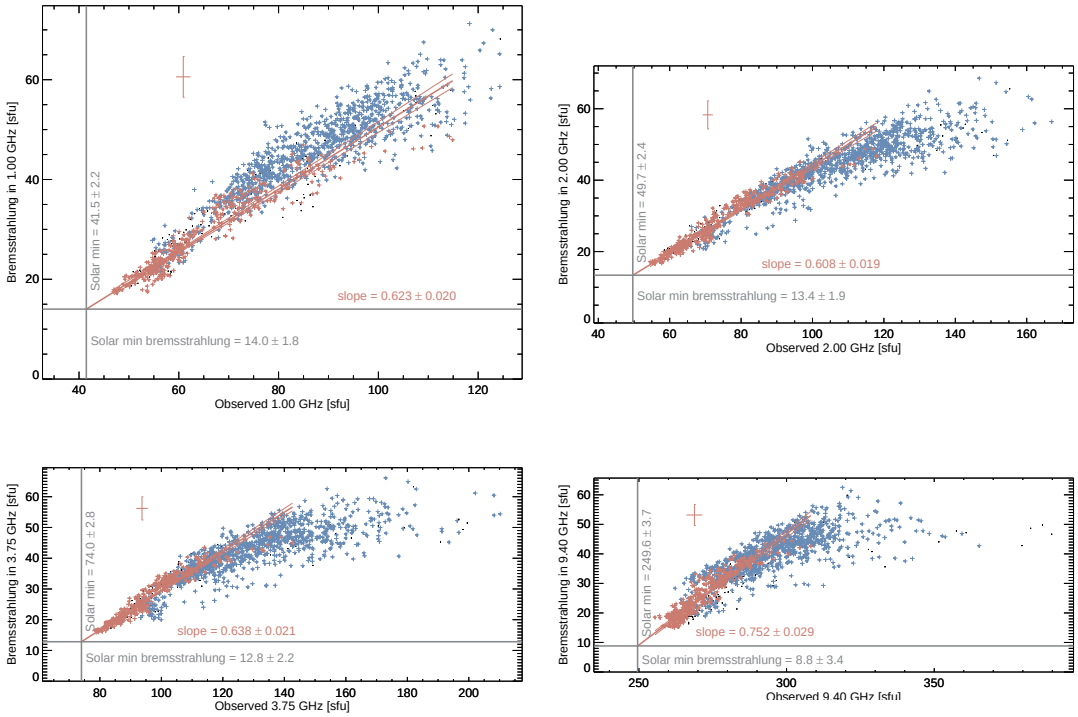

Fig. 6.17.— The same as Figure 6.16 but for the four NoRP frequencies.

deviates from the NoRP measurements, but since this deviation is both above and below the NoRP trends, it is not clear that including a correction factor would lead to better overall agreement. The spectral fitting with these five-point spectra is noisier than with only four points (spectra that are identified without a residual component do not look as clean as the original fits) suggesting that the method is tuned for best performance with the four point spectra. Nonetheless, the spectral classification still appears effective.

6.3.3. Comparing the DEM and Spectroscopically Determined Emission Components

With the more accurate chromospheric subtraction it is now possible to compare the bremsstrahlung and gyroresonance emission predicted from the spectral classification with the predictions from the DEM calculation. These are shown in Figure 6.18 for all five frequencies. There is a good linear relationship between the two bremsstrahlung predictions, and all five frequencies are consistent. However, the spectral determination consistently suggests more bremsstrahlung emission than the DEM method, and this offset is activity dependent, with larger deviations at higher activity levels. The gyroresonance predictions show a clear separation with frequency, as expected, but primarily in the spectral determination. The spectral identification method finds very little gyroresonance emission at both 1.0 and 9.4 GHz, but the DEM method often suggests significant (although less than the three central frequencies) gyroresonance contribution. Additionally, the DEM method consistently calculates more gyroresonance emission than the spectral method, which is expected given that it finds less bremsstrahlung. These signatures suggest a systematic problem in one of the two (or both) methods to determine the emission components.

6.4. Coronal Iron Abundance or a Variable Chromosphere?

The discrepancy between the bremsstrahlung and gyroresonance components determined by the DEM and spectral identification methods can be traced to the slopes of the bremsstrahlung fits in Figures 6.16 and 6.17. Since the slopes are determined by comparing the DEM bremsstrahlung component with the observations on days that are spectroscopically identified to be pure bremsstrahlung

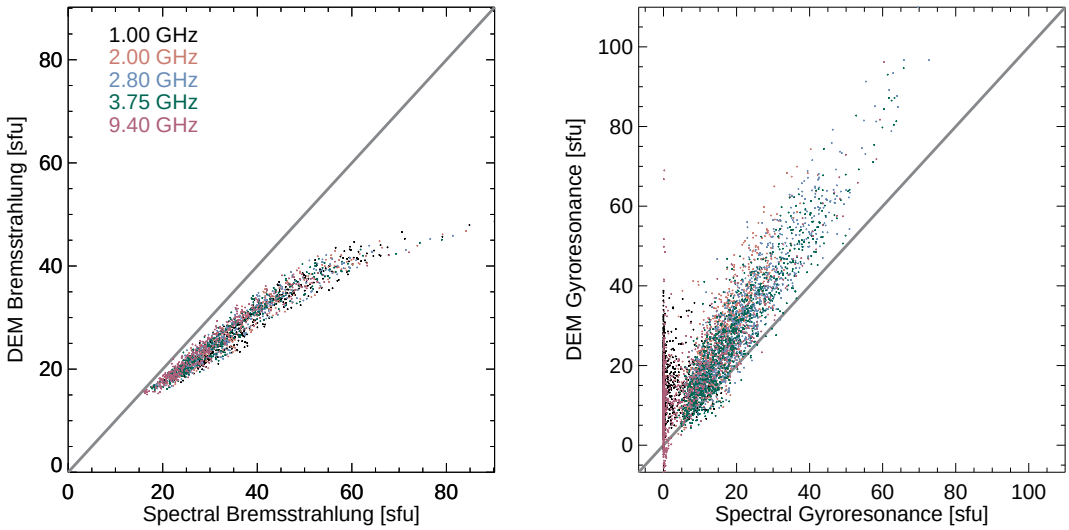

Fig. 6.18.— The comparison between the *left:* bremsstrahlung and *right:* gyroresonance components of the multi-frequency microwave observations. The component calculated from the DEM bremsstrahlung prediction is plotted on the y-axis versus the spectrally identified component on the x-axis. The gray lines indicate where the determinations from the two methods are equal. Each plot only includes the days identified as purely the relevant emission in the "Observed-chromosphere" plot of Figure 6.15, i.e. pure bremsstrahlung emission on the left and pure bremsstrahlung and gyroresonance on the right.

emission, they should be one. Put another way, all the increase in the observations above the solar minimum level should be due to the predicted bremsstrahlung emission. The fact that the DEM predicted bremsstrahlung component does not explain all of the emission on these days suggests one of two possible problems (or a combination of the two). A lower coronal iron abundance or a variable chromospheric contribution could lead to slopes being less than one as observed.

6.4.1. A Decreased Iron Abundance

As discussed in detail in Chapter 3.1.2, the elemental abundances are critical for scaling DEMs determined from EUV atomic line emission. In particular, for

a DEM determined from emission by a single element, the DEM scales inversely with the elemental abundance. The DEMs calculated in Chapter 5 used only iron emission lines and assumed an Fe abundance 3.89 times the photospheric level (as mentioned in Chapter 5.2.3) due to the FIP enhancement. However, the average slope of the bremsstrahlung relationships in Figures 6.16 and 6.17 suggests that the Fe abundance should be 0.64 times the canonical value used, or 2.5 times the photospheric level. This would cause the DEM bremsstrahlung predictions to increase by a factor of $1/0.64 = 1.56$. The corresponding gyroresonance emission can then easily be calculated using equation 6.1 and this new corrected bremsstrahlung series.

The results using this abundance corrected bremsstrahlung series compared to the spectrally identified emission components are shown in Figure 6.19. By construction, this correction brings the DEM predicted bremsstrahlung emission in line with the spectrally predicted bremsstrahlung component. However, this new series now causes the DEM method to under predict the gyroresonance emission significantly compared to the spectral identification, especially at low activity levels. This suggests that, while this corrected bremsstrahlung series is appropriate for days without gyroresonance emission (generally days with less activity), it overestimates the bremsstrahlung emission during high levels of activity.

Looking specifically at the gyroresonance emission in this abundance corrected scenario, Figure 6.20 shows that this reduction in gyroresonance emission dramatically reduces the amount of statistically significant emission. In fact, while the original series showed gyroresonance emission almost constantly during solar maximum (2011–2014), this abundance corrected series suggests that gyroresonance emission is only significant in isolated periods when the Sun is most active.

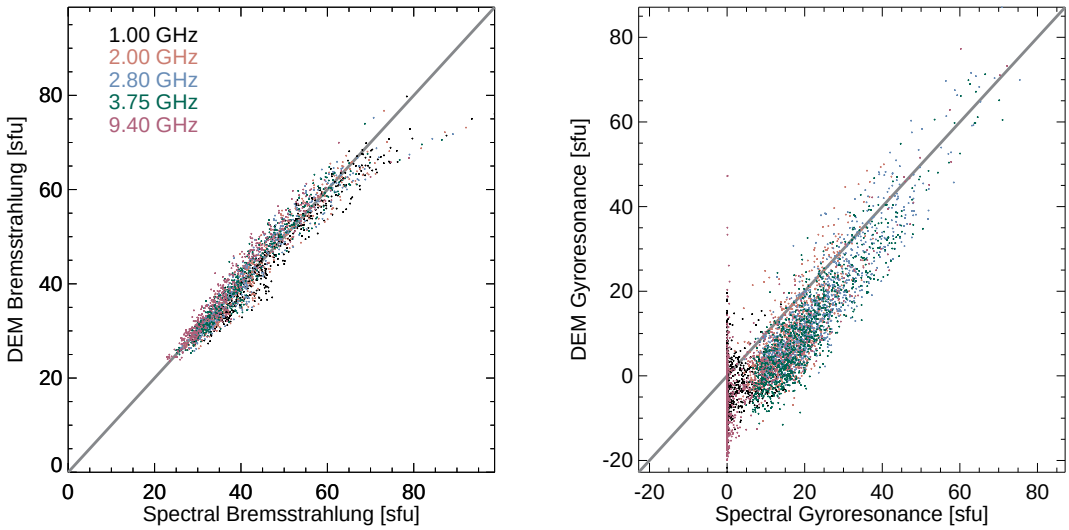

Fig. 6.19.— The same as Figure 6.18 but calculated using the corrected iron abundance of 2.5 times the photospheric abundance.

This corrected series predicts only 14.7 ± 15.3 sfu of gyroresonance emission in $F_{10.7}$ on 2011 December 9, in line with the determination of 6.2 ± 0.3 sfu from the imaging analysis. Additionally, in this corrected series there is almost never statistically significant gyroresonance emission at 1.0 GHz.

While this abundance correction does bring the DEM bremsstrahlung prediction in line with the spectroscopic results, it is unlikely that this correction is appropriate. This simple 1.5 times scaling of the DEMs is hard to reconcile with the results of Chapter 4. Additionally, if there is an abundance correction it is likely that it would be variable in time, and that is too complicated an effect to identify with this data.

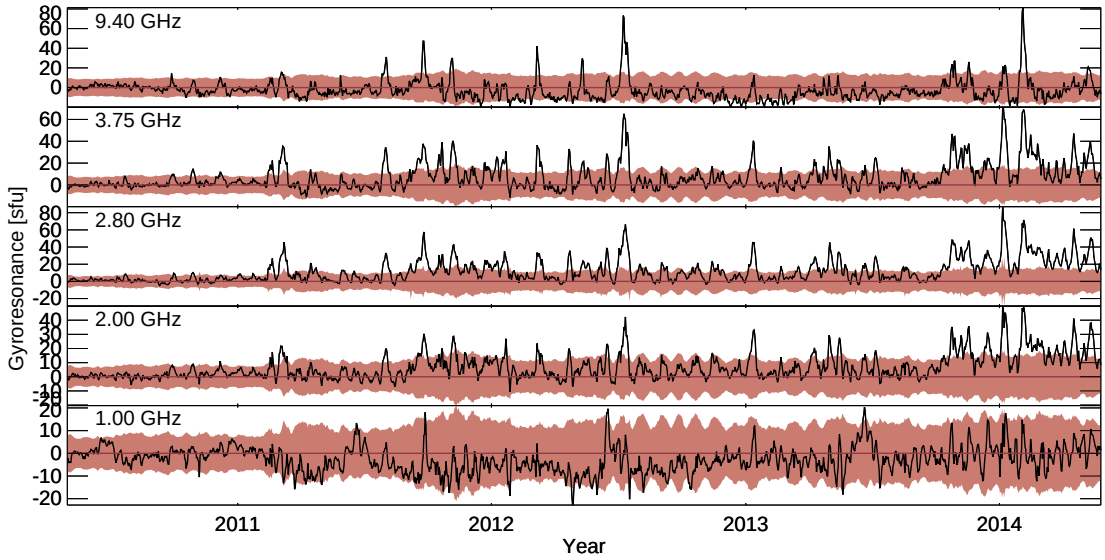

Fig. 6.20.— The same as Figure 6.14 but calculated using the corrected iron abundance of 2.5 times the photospheric abundance. Notice that a reduced iron abudance suggests significantly less gyroresonance emission. This also suggests significantly more negative gyroresonance emission (i.e. an overestimation of the bremsstrahlung component) but this is typically within the 1σ error envelope.

6.4.2. Chromospheric variability

An alternative explanation for the inability of the DEM bremsstrahlung component to account for the observed variability of the spectroscopically identified bremsstrahlung only emission days is the possibility of chromospheric variability. All analysis to this point has assumed that the chromospheric microwave emission is constant, but the chromosphere is known to exhibit variability similar to the corona. In fact, the chromospheric Mg II core-to-wing ratio in the h and k doublet emission lines is used as a solar activity proxy just like $F_{10.7}$ (e.g., Suess et al. 2016). Including a variable chromosphere in the analysis means that, even on days without gyroresonance emission, the bremsstrahlung variability only contributes to a portion of the enhancement over the solar minimum level.

To determine the chromospheric variability only those days that are spectroscopically determined to contain pure bremsstrahlung emission are considered. This chromospheric emission (the observation less the DEM bremsstrahlung component) is then correlated with the flux in the He II 304 Å emission line observed in the MEGS-A spectra discussed in Chapter 5. He II 304 Å emission peaks at temperatures of about 8×10^4 K from plasma in the transition region and upper chromosphere and it is the single brightest line in a non-flaring EUV spectrum, e.g. Figure 2.2. Because this line originates in the transition region and upper chromosphere it will tend to correlate better with the lower frequency microwave observations and the correlation with 9.4 GHz is so poor ($R < 0.5$) that this variable chromosphere component is not fit at 9.4 GHz.

Using the correlation between He II 304 Å and the chromospheric component of the microwave observations on bremsstrahlung only days, the chromospheric contribution can be estimated for every day. This variable chromosphere along with the other components and the observed $F_{10.7}$ is shown in Figure 6.21 and the fractional contribution of the three components is shown in Figure 6.22. It is clear that the variable chromosphere varies much like the coronal bremsstrahlung emission which is expected given both the linearity of the DEM bremsstrahlung predictions with the observed bremsstrahlung only variability and the coupling between the chromosphere and corona. Figure 6.22 highlights how attributing more emission to the chromosphere leads to reduced calculated gyroresonance emission. The same analysis is shown for the NoRP observations in Figure 6.23.

This variable chromosphere can also be used in the spectral identification process with the daily variable chromospheric component used to fit each observed spectrum. Figure 6.24 compares the DEM and spectrally determined

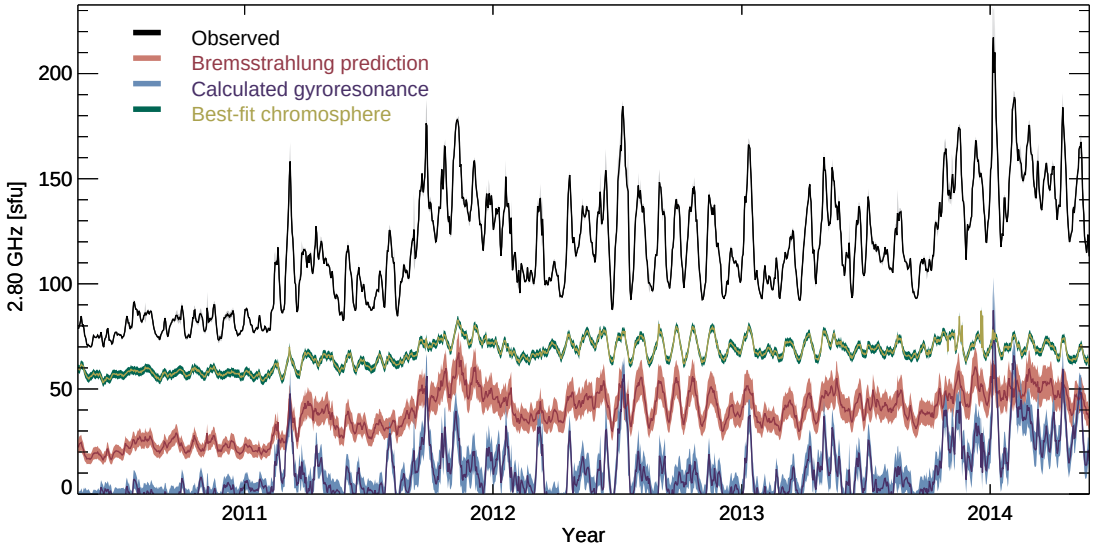

Fig. 6.21.— The same as 6.2 but with the chromospheric contribution calculated based on the correlation with the He II 304 Å line and the gyroresonance component calculated accordingly.

bremsstrahlung and gyroresonance emission components using the variable chromosphere. Again, this correction brings the bremsstrahlung relationship into good agreement, although this time by reducing the spectroscopically determined component. The DEM gyroresonance determination again over-corrects the original deviation and underpredicts the emission compared with the spectral gyroresonance component. However, the relationship is tighter than for the abundance corrected version in Figure 6.19. This suggests that the chromosphere is being over-predicted at high activity levels.

Investigating the gyroresonance emission in detail in Figure 6.25 shows that this reduction in gyroresonance is much more moderate than for the abundance correction shown in Figure 6.20. While this variable chromosphere again suggests very little gyroresonance emission at 1.0 GHz, there are now more periods with gyroresonance emission at higher frequencies, especially during 2011. In partic-

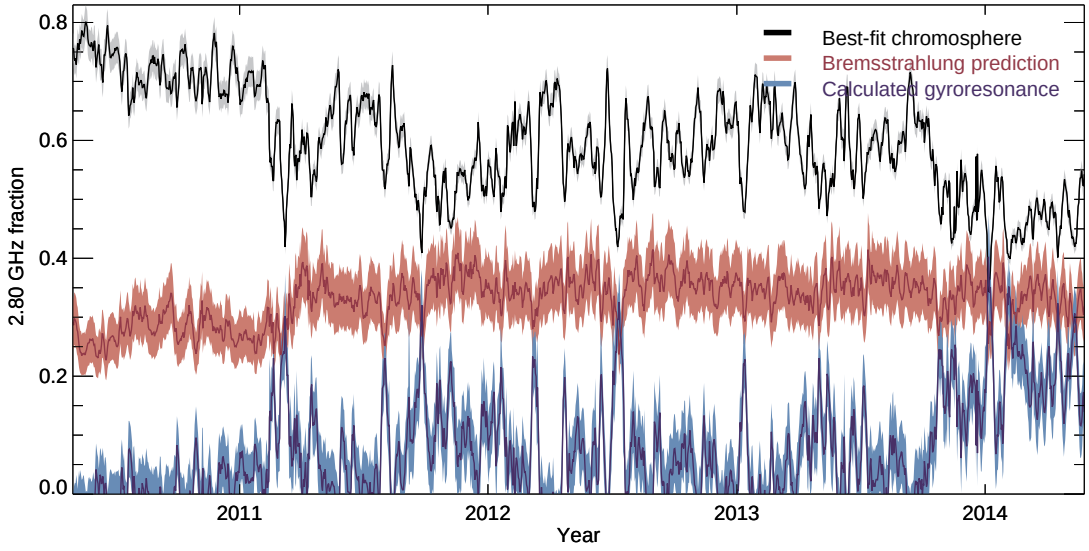

Fig. 6.22.— The same as 6.3 but with the chromospheric contribution calculated based on the correlation with the He II 304 Å line and the gyroresonance component calculated accordingly.

ular, this variable chromosphere series predicts 22.0 ± 8.1 sfu of gyroresonance emission in $F_{10.7}$ on 2011 December 9. This is within 2σ of the imaging determination of 6.2 ± 0.3 sfu and also a significant gyroresonance detection, unlike the results found using the modified iron abundance in Chapter 6.4.1.

6.5. Results

Using the full-Sun DEM time series computed in Chapter 5 the coronal bremsstrahlung component of the solar microwave emission is calculated. This allows for an investigation of how bremsstrahlung and the corresponding gyroresonance emission vary with the solar cycle. It is found that the bremsstrahlung emission accounts for a consistent 20–40% of the observed $F_{10.7}$ with generally a larger contribution during solar maximum. This analysis also suggests that gyroresonance emission is much more variable, between 0% contribution to $F_{10.7}$ at

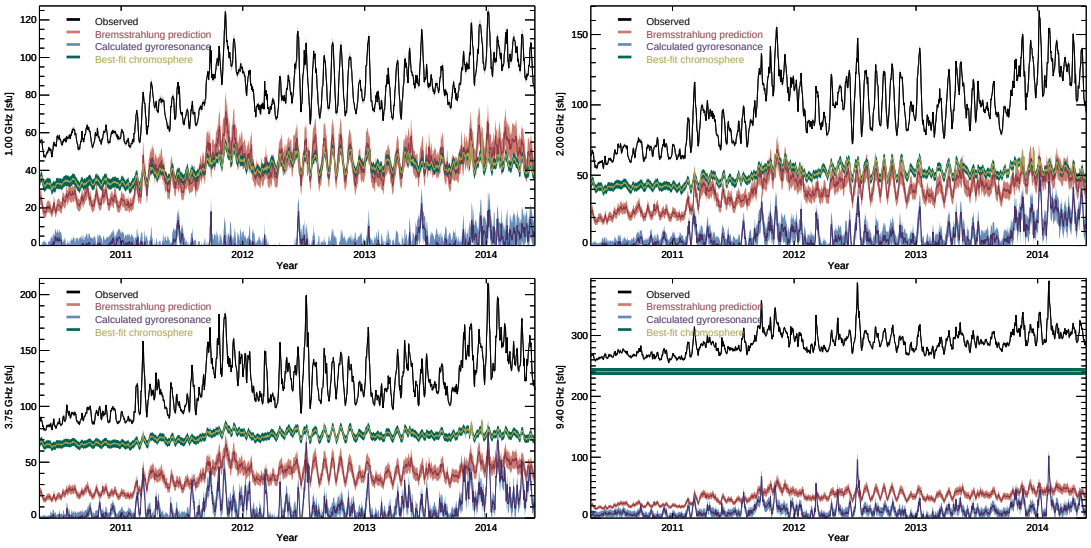

Fig. 6.23.— The same as Figure 6.13 but with the chromospheric contribution calculated based on the correlation with the He II 304 Å line (except at 9.4 GHz) and the gyroresonance component calculated accordingly.

solar minimum and over 40% for short times during the most active rotations of solar maximum.

It is simple to calculate that the solar limb optical depth effects identified in Chapter 4.4 will cause a signal delay of order half a day between the observation of EUV and $F_{10.7}$ sources rotating onto (or off of) the solar disk. This effect is very dependent on frequency since the apparent size of the Sun changes sharply with frequency in the microwave. The source altitude and latitude also influence the magnitude of this delay. However, the one days sampling of the series observed here means that even during the period of most regular solar rotation, there is no identifiable delay between the predicted bremsstrahlung and observed $F_{10.7}$ series.

Comparing the components of the $F_{10.7}$ series with magnetic field parameterizations described in Henney et al. (2012) suggests that bremsstrahlung emission

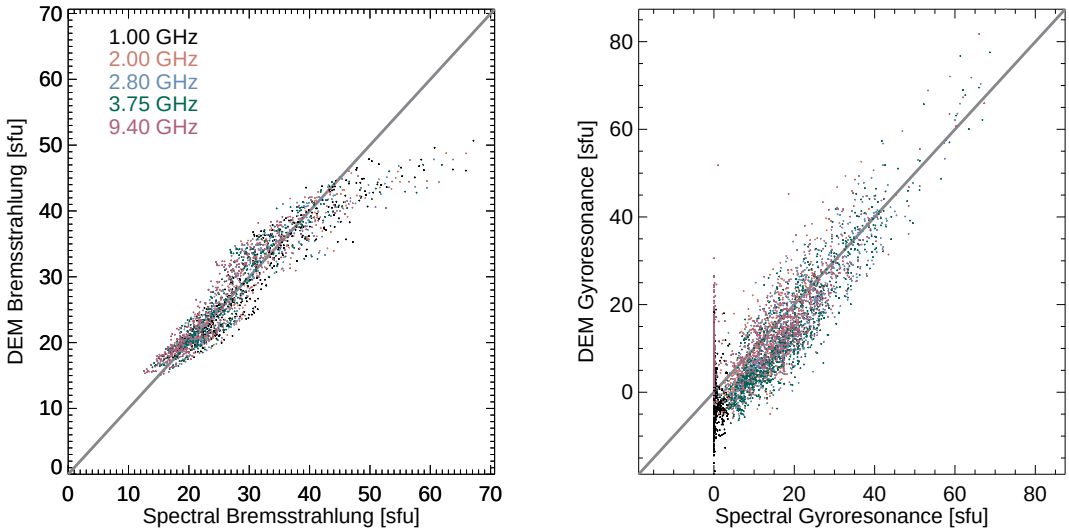

Fig. 6.24.— The same as Figure 6.18 but with the chromospheric contribution calculated based on the correlation with the He II 304 Å line (except at 9.4 GHz).

correlates well with weak to moderate magnetic fields while gyroresonance emission correlates with stronger magnetic fields. These correlations suggest that parameterizing $F_{10.7}$ emission by the underlying photospheric magnetic field strength does reasonably identify the source mechanism of the emission. However, the general correlation between all magnetic fields means that this relationship may not be causal. In particular, the fact that gyroresonance emission does not correlate any more strongly with the photospheric fields needed to excite third harmonic emission (commonly responsible for observed gyroresonance emission, White & Kundu 1997) than fourth harmonic emission suggests that the detection of these fields is not a direct indication of gyroresonance emission.

Relating the bremsstrahlung prediction with the observed $F_{10.7}$ shows a clear non-linear relationship that is fit with a piecewise linear and power law function. Using this relationship to parameterize low resolution EUV observations

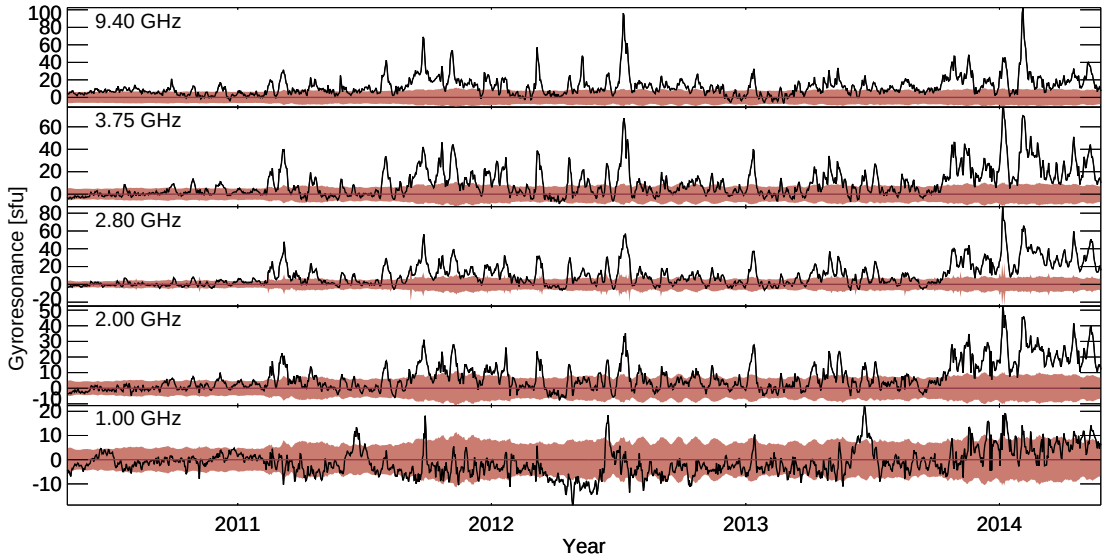

Fig. 6.25.— The same as Figure 6.14 but with the chromospheric contribution calculated based on the correlation with the He II 304 Å line (except at 9.4 GHz) and the gyroresonance component calculated accordingly. Notice that the increased chromospheric contribution suggests significantly less gyroresonance emission. This also suggests significantly more negative gyroresonance emission (i.e. an overestimation of the other two components) but this is typically within the 1σ error envelope.

shows that it performs no better than the common 81-day averaged $F^a_{10.7}$ formulation, and slightly worse at longer EUV wavelengths. This may be due to the bremsstrahlung insensitivity to chromospheric emission that contributes to EUV emission particularly at the longer EUV wavelengths. The bremsstrahlung parameterization does have an operational advantage, however, because it is derived from observations on a single day rather than an 81-day centered average.

The bremsstrahlung and gyroresonance component analysis is also performed at 1.0, 2.0, 3.75, and 9.4 GHz using observations from the NoRP. These are compared with the bremsstrahlung and gyroresonance components identified based on their spectroscopic signatures. The constant chromospheric component assumed for all the previous analysis is calculated using the classification of the daily spec-

tra and the identification of days without gyroresonance emission. One interesting finding from the spectra is that the bremsstrahlung component calculated from the DEMs does not account for all of the observed variability on days without gyroresonance emission. This means that just using the DEM prediction will over estimate the gyroresonance contribution.

This discrepancy can be explained either as a consequence of calculating the DEMs using an incorrect iron abundance or as an indication that the chromospheric emission component is variable, contrary to previous assumptions. Correcting the iron abundance down can force agreement between the DEM and spectral bremsstrahlung determinations, but it is in conflict with the findings of Chapter 4 and leads to a significant underestimation of the gyroresonance emission compared to the spectroscopic identification. On the other hand, allowing a variable chromospheric contribution corrects the spectrally identified bremsstrahlung component into agreement with the DEM determination while also coming more into line with known chromospheric variability. This method still underestimates the DEM determined gyroresonance emission compared to the spectroscopically identified component, but to a lesser degree and while still suggesting significant gyroresonance during most of solar maximum.

7. CONCLUSION

The investigations described herein used the methodology of EUV DEM analysis and applied it to the study of $F_{10.7}$ and other solar microwave emission. Bridging these high and low energy emission regimes enabled a more comprehensive understanding of the solar corona. Studying the corona in the EUV allowed for a detailed understanding of its thermal structure, while the microwave analysis helped constrain the densities and abundances of the emitting plasma. Combined they facilitated the determination of the source mechanisms responsible for the observed microwave emission and a better understanding of how $F_{10.7}$ should be used as an EUV proxy.

The goal of Chapter 4 was to investigate the spatial relationship between EUV and $F_{10.7}$ bremsstrahlung and gyroresonance emission using full-Sun DEMs. Utilizing the highest resolution $F_{10.7}$ image (at the time) recorded by the VLA, and DEMs computed by the AIA, the majority of the observed coronal $F_{10.7}$ signal was found to be due to bremsstrahlung emission and the prediction of this component from DEMs accurately reproduced the observed coronal active region structures. In concert with the polarization measurements in $F_{10.7}$, the DEMs were used to identify coronal gyroresonance emission directly above strong photospheric magnetic fields, including from a source above an isolated magnetic pore outside of an active region. In total, only $8.1 \pm 0.5\%$ of the observed variable $F_{10.7}$ was determined to result from gyroresonance emission. Finally, an optical depth effect was identified that led to a similar amount of $F_{10.7}$ from sources just beyond the solar limb being blocked by the optically thick (at 2.8 GHz) chromosphere.

Using the motivation of the positive results from the initial study, the next

step was to expand the analysis to a long time series to investigate how the contribution of bremsstrahlung and gyroresonance emission varied over the solar cycle. This study utilized the MEGS-A four year spectral data set to compute daily DEMs during the rise phase of solar cycle 24 as described in Chapter 5. These DEMs revealed an astonishing feature of the solar corona, it's apparent existence in either a solar minimum or solar maximum state, with almost no intermediary transition. The amount of low temperature plasma in the corona remained almost constant over the four years of observations (an important finding given that cooler plasma is disproportionately responsible for bremsstrahlung emission) while the mid and high temperature plasma associated with active regions transitioned one time over the course of a month and a half between low and high activity levels.

This work culminated in a multifaceted investigation of the implications of this DEM time series on the temporal evolution of bremsstrahlung and gyroresonance emission across the microwave spectrum presented in Chapter 6. Except during the most intense levels of solar activity when gyroresonance emission peaks, coronal $F_{10.7}$, and in fact all coronal microwave emission, is found to be dominated by the bremsstrahlung mechanism. Bremsstrahlung emission accounts for 20–40% of $F_{10.7}$ while gyroresonance accounts for 0–> 40%. Yet, despite the dominance of bremsstrahlung emission, the intrinsic variability between it and the total $F_{10.7}$ makes it difficult to isolate for use as an EUV proxy. In fact, the long used 81-day $F_{10.7}$ averaging seems to capture the correlation with EUV as well or better than the physics based connection with bremsstrahlung emission. In addition, use of the spectral features of gyroresonance emission helped identify the effect of chromospheric variability on the microwave time series. It was also determined that the two emission components are associated with the strength of photospheric

magnetic fields, with the magnetically activated gyroresonance emission responding to the presence of magnetic fields strong enough to activate the mechanism. However, the importance of the spatial relationship between the emission and the magnetic fields will necessitate further study.

7.1. Future Work

Much work remains to be done with the assembled data set. Further investigation of the split DEM effect is warranted as it may be responsible for some of the problems with the relationship between the bremsstrahlung predictions and the various low-resolution EUV observations. There is also much promise in detailed comparison between different spectral regions and the derived DEMs and microwave emission components. This could lead to improved proxy relationships or more descriptive relationships between specific EUV spectral ranges. For example, a line other than or in addition to the He II 304 Å chromosphere/transition region line may provide a better relationship with chromospheric emission. There may even be a self consistent way to use only the microwave observations to identify the chromospheric variability so that all three emission components can be isolated without any EUV observations. This could also lead to complete spectral parameterization based on $F_{10.7}$ or other microwave measurements, similar to the method of Girazian & Withers (2015).

There are also obvious next steps to take to expand the analysis begun here. Stephen White has already set in motion a project to compute DEMs for the complete time series of AIA observations. This would allow a spatially resolved investigation of the daily DEMs presented herein that would help improve the

understanding of the rotational modulation of the signals and better connect the photospheric magnetic fields to the emission components. In addition, the AIA is still in operation, and by calibrating AIA DEMs from those derived with EVE it would allow for the extension of all these analyses for another three years and into the future, hopefully all the way into the next solar cycle.

Lastly, the current commissioning of EOVSA is the most exciting development for coronal radio observations since the upgrade to the VLA. EOVSA will provide daily (and faster) full-Sun images between 3 and 18 GHz. Coupled with AIA DEMs, these data will allow for the analysis presented in Chapter 4 every day and open the door for regular three dimensional measurements of coronal active region magnetic fields (e.g. White 2005; Iwai & Shibasaki 2013; Wang et al. 2015; Miyawaki et al. 2016). EOVSA will dramatically alter the way the corona is studied by providing, for the first time, this new spectral window into the solar atmosphere.

APPENDIX

APPENDIX A. The EVE Spectrum Around Fe XVIII 93.9 Å

EVE data for the Fe XVIII 93.9 Å line are a commonly used diagnostic of solar flares because it is one of the strongest hot lines observed by EVE. With a peak emission temperature of 7 MK ($\log(T) = 6.85$), it is an ideal flare diagnostic, with small response to typical coronal temperatures but easily reached by even small flares (e.g., Warren et al. 2011; Petkaki et al. 2012). This region of the spectrum is especially notable because the Atmospheric Imaging Assembly on *SDO* (AIA; Lemen et al. 2012) employs 94 Å bandpass images as one of the primary diagnostics of high-temperature coronal plasma. However, this wavelength range lacks well-calibrated high-resolution spectra of the quality that is available at longer EUV wavelengths, and this limits the line identifications available for the CHIANTI database. The NASA *Extreme-Ultraviolet Explorer* (*EUVE*) mission observed the 93.9 Å Fe XVIII line in a large number of active stars, but with insufficient signal-to-noise ratio to identify cooler lines at neighboring wavelengths (e.g., Mewe et al. 1995; Sanz-Forcada et al. 2003). Such cool (e.g., Fe X) lines were known to lie near the Fe XVIII line when *SDO* was launched (Boerner et al. 2012), but CHIANTI did not reproduce the spectrum completely (Aschwanden & Boerner 2011; Reale et al. 2011; Testa et al. 2012; Aschwanden et al. 2013), although it is believed that the Fe XVIII 93.9 Å line itself is correctly represented in CHIANTI (Warren et al. 2012; Del Zanna 2013). Del Zanna et al. (2012) identified an Fe XIV line that is blended with Fe XVIII in the EVE spectra, and empirical corrections have been made to the AIA temperature response functions (Del Zanna 2013; Boerner et al. 2014). These complications are often avoidable in flare studies where the pre-flare emission can be subtracted (e.g. Warren et al. 2013) to isolate only contributions from the high-temperature flare plasma, which emits primarily

in the well-characterized Fe XVIII line.

Because the analysis in Chapter 5 focuses specifically on the nonflaring corona, this type of subtraction technique is inappropriate. It is therefore necessary to investigate the spectrum surrounding the Fe XVIII 93.9 Å line to determine whether it contributes sufficiently to the EVE spectra to constrain high-temperature emission. Figure A.1 compares EVE spectra with Version 8.0.2 of the CHIANTI model spectra generated using DEMs computed as described in Chapter 5.2. The CHIANTI models show the same three peaks visible in the EVE data, but with amplitudes about half or less of what is observed in the 91–97 Å range. Because these emission features span a wide range of coronal temperatures (1–7 MK, $\log(T) =$ 6–6.85), including those well represented in the calculated DEMs, it is clear that some other factor is affecting this region of the spectrum. The three most likely explanations are problems with the EVE MEGS-A calibration in this region of the spectrum, unexplained continuum emission, or significant emission from lines not identified in CHIANTI.

This conclusion does not address the issue of whether EVE daily nonflare spectra contain significant Fe XVIII emission. A number of methods for isolating Fe XVIII emission from AIA 94 Å images have been developed (e.g., Warren et al. 2012; Del Zanna 2013). An analogous method is possible using EVE spectra. It is possible to define EVE indices for the AIA 94, 171, and 211 Å bandpasses by integrating over the product of the daily EVE median spectra $I^{EVE}(\lambda)$ with the AIA effective area functions of wavelength,[1] $R^{AIA}(\lambda)$, for these windows and summing over wavelength:

[1]Derived from the Version 6 AIA response files in the SolarSoft distribution of AIA software (Boerner et al. 2012). The unit of effective area is cm^2.

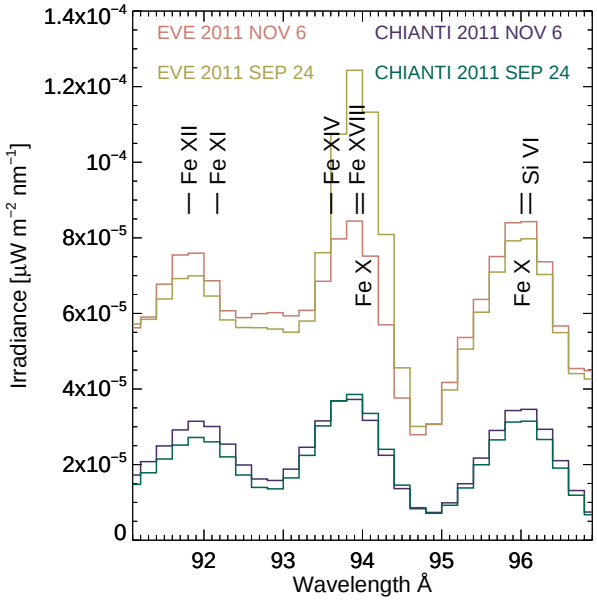

Fig. A.1.— EVE MEGS-A spectra and CHIANTI model spectra calculated from the DEMs derived as described in Chapter 5.2 of the wavelength range surrounding the Fe XVIII 93.9 Å line with the strongest emission lines marked. The 2011 September 24 spectrum includes emission from a flare, while the 2012 November 6 spectrum is typical of nonflaring periods during solar maximum. The CHIANTI models significantly underestimate the emission across this wavelength range. The synthetic spectrum fails to reproduce the increased flare emission on 2011 September 24 because none of the lines used in the DEM calculation are sensitive to flare emission (Figure 5.4).

$$\begin{aligned} E_{94} &= \int I^{EVE}(\lambda)\ R_{94}^{AIA}(\lambda)\ d\lambda \\ E_{171} &= \int I^{EVE}(\lambda)\ R_{171}^{AIA}(\lambda)\ d\lambda \\ E_{211} &= \int I^{EVE}(\lambda)\ R_{211}^{AIA}(\lambda)\ d\lambda. \end{aligned} \tag{A.1}$$

Since the units of EVE irradiance are W m^{-2} nm^{-1} and the summation is over wavelength and multiplied by effective area, these indices have units of W (nominally, the power received by each AIA detector). The following expression proves to be a surprisingly good proxy for E_{94}:

$$A_{94} = 0.0235 \frac{E_{171} E_{211}}{E_{171} + E_{211}} \quad \text{(A.2)}$$

Figure A.2 compares E_{94} (black line) with A_{94} (red line) for the period of MEGS-A observations. A_{94} is generally within a few percent of the EVE index on all days except for a limited number of days when there are sharp spikes in E_{94}. The ability of the AIA 171 and 193 Å bandpasses to reproduce the 94 Å behavior is not surprising. This is because the 94 Å region contains Fe X (94.0 Å) and Fe XIV (93.2 and 93.6 Å) lines in addition to Fe XVIII while the 171 Å AIA bandpass includes Fe IX with a temperature similar to Fe X and the 211 Å AIA bandpass is dominated by Fe XIV. Neither of these bandpasses contains any significant lines hotter than Fe XIV. The most widespread proxy used to separate Fe XVIII from the AIA images also uses the 171 and 211 Å images but in a linear combination (with two free parameters) proposed by Del Zanna (2013), while Warren et al. (2012) used a polynomial combination of 171 and 193 Å with seven free parameters, and Reale et al. (2011) suggested just the AIA 171 Å data to estimate the cool contribution to 94 Å.

Investigation of solar activity on days when the A_{94} proxy departs significantly from the EVE E_{94} index shows that they are all days when significant, usually long-duration flaring occurs in the 19–21 UT window used to derive the EVE median spectra. Because of this it is likely that the EVE full-Sun spectrum around 94 Å only contains significant Fe XVIII emission when flares contribute, and that EVE data do not provide evidence for significant Fe XVIII emission in nonflaring full-Sun spectra. The DEMs derived from the EVE data do not suggest the presence of Fe XVIII emission down to the 7% MEGS-A precision, suggesting that EVE spectra at 94 Å do not help constrain the high-temperature emission

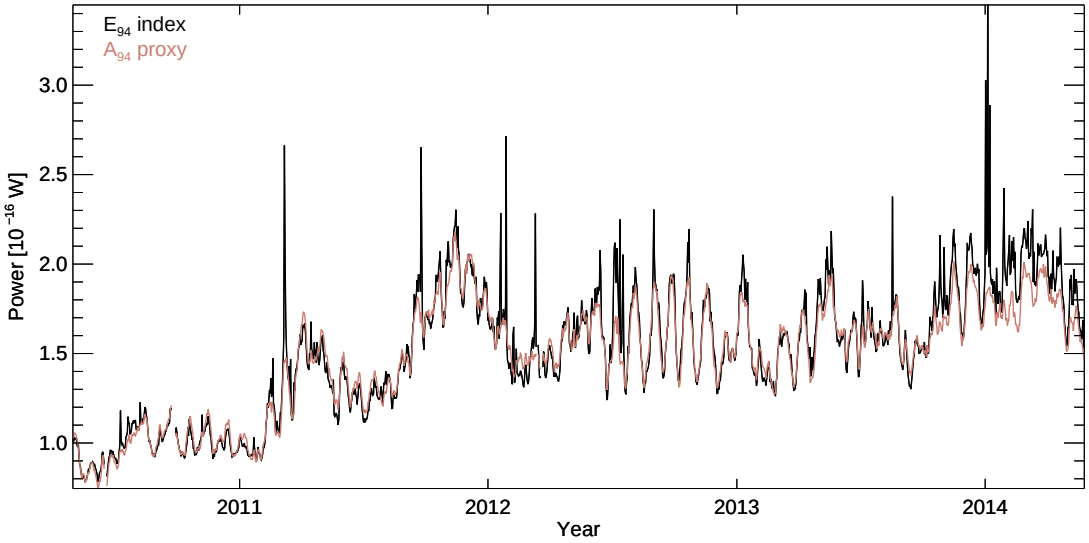

Fig. A.2.— Time series of the intensity in the AIA 94 Å EVE index E_{94} (black) and the 171/211 Å proxy A_{94} (red) as observed by MEGS-A. The sharp spikes in E_{94} where it deviates from A_{94} are times when significant Fe XVIII emission contributes to the 93.9 Å line, suggesting the presence of significant flares with high-temperature plasma.

from the quiet Sun. Imaging observations that better isolate hot areas in active regions will be more successful in constraining the hot component of the solar corona since they are not competing with the cool emission from the entire Sun, as is the case for EVE data.

REFERENCES

Abbott, B. P., et al. 2016a, Physical Review Letters, 116, 1

—. 2016b, Physical Review Letters, 116, 1

—. 2017, Physical Review Letters, 118, 1

Altrock, R. C., DeMastus, H. L., Evans, J. W., Keil, S. L., Neidig, D. F., Radick, R. R., & Simon, G. W. 1985, in Handbook of Geophysics and the Space Environment, ed. A. S. Jursa (Springfield: Air Force Geophysics Laboratory), 1.1–1.25

Anderson, A. D. 1962, Journal of the Atmospheric Sciences1, 19, 207

Anderson, G. P., & Muench, H. S. 1985, in Handbook of Geophysics and the Space Environment, ed. A. S. Jursa (Springfield: Air Force Geophysics Laboratory), 21.1–21.14

Antiochos, S. K., & Sturrock, P. A. 1976, Solar Physics, 49, 359

—. 1978, The Astrophysical Journal, 220, 1137

Argiroffi, C., Peres, G., Orlando, S., & Reale, F. 2008, Astronomy & Astrophysics, 488, 1069

Aschwanden, M. J., & Boerner, P. 2011, The Astrophysical Journal, 732, 81

Aschwanden, M. J., Boerner, P., Schrijver, C. J., & Malanushenko, A. 2013, Solar Physics, 283, 5

Aschwanden, M. J., Sun, X., & Liu, Y. 2014, The Astrophysical Journal, 785, 34

Asplund, M., Grevesse, N., Sauval, a. J., & Scott, P. 2009, Annual Review of Astronomy and Astrophysics, 47, 481

Auchère, F., Boulade, S., Koutchmy, S., Smartt, R. N., Delaboudinière, J. P., Georgakilas, A., Gurman, J. B., & Artzner, G. E. 1998, Astronomy & Astrophysics, 336, L57

Baker, D., Brooks, D. H., Démoulin, P., Yardley, S. L., van Driel-Gesztelyi, L., Long, D. M., & Green, L. M. 2015, The Astrophysical Journal, 802, 104

Balan, N., Bailey, G. J., & Jayachandran, B. 1993, Planetary and Space Science, 41, 141

Balmer, J. 1885, Annalen der Physik und Chemie, 25, 5

Barlier, F., Berger, C., Falin, J. L., Kockarts, G., & Thuillier, G. 1978, Annales de Geophysique, 34, 9

Bastian, T. S., & Dulk, G. A. 1988, in Solar and Stellar Coronal Structure and Dynamics, ed. R. C. Altrock, 386–391

Bhatnagar, V. P., & Mitra, A. P. 1966, Journal of Atmospheric Sciences, 23, 233

Bilitza, D., Altadill, D., Zhang, Y., Mertens, C., Truhlik, V., Richards, P., McKinnell, L.-A., & Reinisch, B. 2014, Journal of Space Weather and Space Climate, 4, A07

Blake, R. L., Chubb, T. A., Friedman, H., & Unzicker, A. E. 1963, The Astrophysical Journal, 137, 3

Boerner, P., et al. 2012, Solar Physics, 275, 41

Boerner, P. F., Testa, P., Warren, H., Weber, M. A., & Schrijver, C. J. 2014, Solar Physics, 289, 2377

Bohr, N. 1913, Philosophical Magazine Series 6, 26, 1

Bouwer, S. D. 1992, Solar Physics, 142, 365

Bowman, B. R., Kent Tobiska, W., Marcos, F. a., & Valladares, C. 2008, Journal of Atmospheric and Solar-Terrestrial Physics, 70, 774

Bradshaw, S. J., & Cargill, P. J. 2010, The Astrophysical Journal, 717, 163

Brickhouse, N. S., & Schmelz, J. T. 2006, The Astrophysical Journal, 636, L53

Brooks, D. H., Baker, D., Driel-gesztelyi, L. V., & Warren, H. P. 2017, Nature Communications, 8, 1

Brueckner, G. E., et al. 1995, Solar Physics, 162, 357

Cargill, P. J., & Bradshaw, S. J. 2013, The Astrophysical Journal, 772, 40

Cargill, P. J., & Klimchuk, J. a. 2004, The Astrophysical Journal, 605, 911

Carroll, B. W., & Ostlie, D. A. 2007, An Introduction to Modern Astrophysics Second Addition, 2nd edn., ed. A. R. S. Black, D. Greco, & C. Benson (San Francisco, CA: Pearson Addison Wesley)

Caspi, A., McTiernan, J. M., & Warren, H. P. 2014, The Astrophysical Journal Letters, 788, L31

Champion, K. S. W., Cole, A. E., & Kantor, A. J. 1985, in Handbook of Geophysics and the Space Environment, ed. A. S. Jursa (Springfield: Air Force Geophysics Laboratory), 14.1–14.43

Chen, Y., Liu, L., & Wan, W. 2011, Journal of Geophysical Research (Space Physics), 116, A04304

—. 2012, Journal of Geophysical Research (Space Physics), 117, A03313

Cheung, M. C. M., Boerner, P., Schrijver, C. J., Testa, P., Chen, F., Peter, H., & Malanushenko, A. 2015, The Astrophysical Journal, 807, 143

CIRA. 1961, CIRA 1961: COSPAR International Reference Atmosphere, 1961 (Amsterdam: North-Holland Publishing Co), 177

—. 1965, CIRA 1965: COSPAR international reference atmosphere, 1965 (Amsterdam: North-Holland Publishing Co), 313

—. 1972, CIRA 1972: COSPAR international reference ionosphere 1972 (Berlin: Akademie-Verlag), 450

Covington, A. E. 1947, Nature, 159, 405

—. 1948, Proceedings of the IRE, 36, 454

—. 1951, Journal of the Royal Astronomical Society of Canada, 45, 15

—. 1969, Journal of the Royal Astronomical Society of Canada, 63, 125

Covington, A. E., Medd, W. J., Harvey, G. A., & Broten, N. W. 1955, Journal of the Royal Astronomical Society of Canada, 49, 235

Craig, I. J. D., & Brown, J. C. 1976, Astronomy & Astrophysics, 49, 239

Dandekar, B. S. 1985, in Handbook of Geophysics and the Space Environment, ed. A. S. Jursa (Springfield: Air Force Geophysics Laboratory), 10.38–10.45

Dantzig, G., Orden, A., & Wolfe, P. 1955, Pacific Journal of Mathematics, 5, 183

De Lafontaine, J., & Garg, S. C. 1982, Proceedings of the Indian Academy of Science, Earth and Planetary Sciences, 5, 197

Del Zanna, G. 2013, Astronomy & Astrophysics, 558, A73

Del Zanna, G., Dere, K. P., Young, P. R., Landi, E., & Mason, H. E. 2015, Astronomy & Astrophysics, 582, A56

Del Zanna, G., O'Dwyer, B., & Mason, H. E. 2011, Astronomy & Astrophysics, 535, A46

Del Zanna, G., Storey, P. J., Badnell, N. R., & Mason, H. E. 2012, Astronomy & Astrophysics, 541, A90

Deng, L. H., Li, B., Zheng, Y. F., & Cheng, X. M. 2013, New Astronomy, 23, 1

Dere, K. P., Landi, E., Mason, H. E., Monsignori Fossi, B. C., & Young, P. R. 1997, Astronomy and Astrophysics Supplement Series, 125, 149

Dere, K. P., Landi, E., Young, P. R., Del Zanna, G., Landini, M., & Mason, H. E. 2009, Astronomy & Astrophysics, 498, 915

Dickinson, R. E., Ridley, E. C., & Roble, R. G. 1981, Journal of Geophysical Research, 86, 1499

Domingo, V., Fleck, B., & Poland, A. I. 1995, Solar Physics, 162, 1

Doschek, G. a., Warren, H. P., Laming, J. M., Mariska, J. T., Wilhelm, K., Lemaire, P., Schühle, U., & Moran, T. G. 1997, The Astrophysical Journal, 482, L109

Dudok De Wit, T., & Bruinsma, S. 2011, Geophysical Research Letters, 38, L19102

Dudok de Wit, T., Bruinsma, S., & Shibasaki, K. 2014, Journal of Space Weather and Space Climate, 4, A06

Dudok de Wit, T., Kretzschmar, M., Lilensten, J., & Woods, T. 2009, Geophysical Research Letters, 36, L10107

Dulk, G. A. 1985, Annual Review, Astronomy & Astrophysics, 23, 169

Eddy, J. A., & Ise, R. 1979, A new sun : the solar results from SKYLAB (Washington, DC: Scientifi and Technical Information Office, National Aeronautics and Space Administration)

Feldman, U. 1992, Physica Scripta Volume T, 46, 202

Feldman, U., & Behring, W. E. 1974, The Astrophysical Journal Letters, 189, L45

Felli, M., Lang, K. R., & Willson, R. F. 1981, The Astrophysical Journal, 247, 325

Fletcher, L., Hannah, I. G., Hudson, H. S., & Innes, D. E. 2013, The Astrophysical Journal, 771, 104

Fontenla, J. M., Codrescu, M., Fedrizzi, M., Fuller-Rowell, T., Hill, F., Landi, E., & Woods, T. 2017, The Astrophysical Journal, 834, 54

Foukal, P. 1998, Geophysical Research Letters, 25, 2909

Fowler, A. 1912, Monthly Notices of the Royal Astronomical Society, 73, 62

Fröhlich, C. 2009, Astronomy & Astrophysics, 501, L27

Fuller-Rowell, T. J., & Rees, D. 1980, Journal of Atmospheric Sciences

Fürst, E., Hirth, W., & Lantos, P. 1979, Solar Physics, 63, 257

Gaetz, T. J., & Salpeter, E. E. 1983, The Astrophysical Journal Supplement Series, 52, 155

Garret, H. B. 1985, in Handbook of Geophysics and the Space Environment, ed. A. S. Jursa (Springfield: Air Force Geophysics Laboratory), 7.1–7.37

Gary, D. E. 1996, in Astronomical Society of the Pacific Conference Series, ed. A. R. Taylor & J. M. Paredes, Vol. 93, San Francisco, CA, 387–396

Gary, D. E., Hurford, G. J., Nita, G. M., White, S. M., Tun, S. D., Fleishman, G. D., & McTiernan, J. M. 2011, in AAS/Solar Physics Division Abstracts #42, 1.02

Giacconi, R. 2009, Experimental Astronomy, 25, 143

Giacconi, R., Reidy, W. P., Zehnpfennig, T., Lindsay, J. C., & Muney, W. S. 1965, ApJ, 142, 1274

Gingerich, O., Noyes, R. W., Kalkofen, W., & Cuny, Y. 1971, Solar Physics, 18, 347

Girazian, Z., & Withers, P. 2015, Journal of Geophysical Research: Space Physics, 120, 6779

Golub, L., & Pasachoff, J. M. 2010, The Solar Corona, 2nd edn. (Cambridge University Press)

Gopalswamy, N., White, S. M., & Kundu, M. R. 1991, The Astrophysical Journal, 379, 366

Grechnev, V. V., et al. 2003, Solar Physics, 216, 239

Greenstein, J. L. 1984, in The Early Years of Radio Astronomy - Reflections Fifty Years after Jansky's Discovery, ed. W. T. Sullivan (New York: Cambridge University Press), 67–81

Greenstein, J. L., & Minkowski, R. 1953, The Astrophysical Journal, 118, 1

Hadamard, J. 1902, Princeton University Bulletin, 13, 49

Haigh, J. D. 2004, in Solar Variability and its Effects on Climate (American Geophysical Union), 65–81

Hannah, I. G., & Kontar, E. P. 2012, Astronomy & Astrophysics, 539, A146

Harris, I., & Priester, W. 1962, Journal of Geophysical Research, 67, 4585

Hedin, A. E., Reber, C. A., Newton, G. P., Spencer, N. W., Brinton, H. C., Mayr, H. G., & Potter, W. E. 1977, Journal of Geophysical Research, 82, 2148

Henney, C. J., Toussaint, W. a., White, S. M., & Arge, C. N. 2012, Space Weather, 10, S02011

Hey, J. S. 1946, Nature, 157, 47

Hock, R., Woods, T., Eparvier, F. G., & Chamberlin, P. C. 2010, in 38th COSPAR Scientific Assembly, 5

Hock, R. A. 2012, PhD thesis, University of Colorado at Boulder

Hock, R. a., Chamberlin, P. C., Woods, T. N., Crotser, D., Eparvier, F. G., Woodraska, D. L., & Woods, E. C. 2012, Solar Physics, 275, 145

Huang, J., Hao, Y., Zhang, D., & Xiao, Z. 2016, Journal of Geophysical Research (Space Physics), 121, 6844

Hudson, R. D. 1971, Reviews of Geophysics and Space Physics, 9, 305

Iwai, K., & Shibasaki, K. 2013, Publications of the Astronomical Society of Japan, 65

Jacchia, L. G. 1964, SAO Special Report, 170

—. 1971, SAO Special Report, 332

Jansky, K. G. 1933, Popular Astronomy, 41, 548

Javaraiah, J. 2016, Astrophysics and Space Science, 361, 208

Johnson, R. W. 2011, Astrophysics and Space Science, 332, 73

Kahler, S. W., Meekins, J. F., & Kreplin, R. W. 1970, The Astrophysical Journal, 162, 293

Kallmann-Biji, H. K., & Sibley, W. L. 1964, in Space Research IV: Proceedings of the Fourth International Space Science Symposium, ed. P. Muller (Warsaw: North-Holland Publishing Co), 279

Kashyap, V., & Drake, J. J. 1998, The Astrophysical Journal, 503, 450

—. 2000, Bullitin of the Astronomical Society of India, 28, 475

Kennedy, M. B., Milligan, R. O., Mathioudakis, M., & Keenan, F. P. 2013, The Astrophysical Journal, 779, 84

King-Hele, D. G., & Quinn, E. 1965, Journal of Atmospheric and Terrestrial Physics1, 27, 197

King-Hele, D. G., & Rees, J. M. 1963, Journal of Atmospheric and Terrestrial Physics, 25, 495

King-Hele, D. G., & Walker, D. M. C. 1961, in Space Research II: Proceedings of the Second International Space Science Symposium, ed. H. C. van de Hulst, C. de Jager, & A. F. Moore (Florence: North-Holland Publishing Co), 918

Klimchuk, J. A. 2006, Solar Physics, 234, 41

—. 2015, Philosophical Transactions of the Royal Society of London Series A, 373, 20140256

Klimchuk, J. A., Patsourakos, S., & Cargill, P. J. 2008, The Astrophysical Journal, 682, 1351

Klobuchar, J. A. 1985, in Handbook of Geophysics and the Space Environment, ed. A. S. Jursa (Springfield: Air Force Geophysics Laboratory), 10.84–10.88

Knizhnik, K. J., Antiochos, S. K., & Devore, C. R. 2015, The Astrophysical Journal, 809, 137

Krieger, A. S. 1977, in Coronal Holes and High Speed Wind Streams, ed. J. B. Zirker, 71–102

Krieger, A. S., Timothy, A. F., & Roelof, E. C. 1973, Solar Physics, 29, 505

Kumar, S., Paresce, F., Bowyer, S., & Lampton, M. 1974, Applied Optics, 13, 575

Kundu, M. R. 1959, International Astronomical Union, 9, 222

—. 1965, Solar Radio Astronomy (New York: John Wiley & Sons)

Landi, E., & Chiuderi Drago, F. 2003, The Astrophysical Journal, 589, 1054

—. 2008, The Astrophysical Journal, 675, 1629

Landi, E., Young, P. R., Dere, K. P., Del Zanna, G., & Mason, H. E. 2013, The Astrophysical Journal, 763, 86

Lean, J. L., & Brueckner, G. E. 1989, The Astrophysical Journal, 337, 568

Leenaarts, J., Carlsson, M., & van der Voort, R. 2012, The Astrophysical Journal, 749, 136

Lemen, J. R., et al. 2012, Sol. Phys., 275, 17

Lin, R. P., et al. 2002, Solar Physics, 210, 3

Lockyer, J. N. 1868, Proceedings of the Royal Society of London Series I1, 17, 131

Lorentz, H. A. 1895, Attempt of a Theory of Electrical and Optical Phenomena in Moving Bodies (Leiden: E. J. Brill), 139

Lukianova, R., Holappa, L., & Mursula, K. 2017, Journal of Geophysical Research (Space Physics), 122, 2740

Lyman, T. 1906, The Astrophysical Journal, 23, 181

Makarov, V. I., Stoyanova, M. N., & Sivaraman, K. R. 1982, Journal of Astrophysics and Astronomy, 3, 379

Mariska, J. T. 1986, Annual Review of Astronomy and Astrophysics, 24, 23

Markov, A. A. 1906, Izv. Fiz.-Matem. Obsch. Kazan Univ.(2nd Ser), 15, 135

Martin, H. A., Neveling, W., Priester, W., & Roemmer, M. 1961, in Space Research II: Proceedings of the Second International Space Science Symposium, ed. H. C. van de Hulst, C. de Jager, & A. F. Moore (Florence: North-Holland Publishing Co), 902

Martin, S. F., Bilimoria, R., & Tracadas, P. W. 1994, in NATO Advanced Science Insittutes (ASI) Series C, ed. R. J. Rutten & C. J. Schrijver (Kluwer Academic Publishers), 303–338

Martyn, D. F. 1948, Proceedings of the Royal Society Series A Mathematical and Physical Sciences, 193, 44

Maruyama, T. 2010, Journal of Geophysical Research, 115, A04306

—. 2011, Journal of Geophysical Research, 116, A08303

Mathur, S. B., & Mitra, A. P. 1960, Journal of Scientific & Industrial Research, 19A, 311

McIntosh, S. W., et al. 2014, The Astrophysical Journal, 792, 12

McNamara, L. F. 1985, in Handbook of Geophysics and the Space Environment, ed. A. S. Jursa (Springfield: Air Force Geophysics Laboratory), 10.45–10.62

Metropolis, N., Rosenbluth, A. W., Rosenbluth, M. N., Teller, A. H., & Teller, E. 1953, The Journal of Chemical Physics, 21, 1087

Metropolis, N., & Ulam, S. 1949, Journal of American Statistical Association, 44, 335

Mewe, R., Kaastra, J. S., Schrijver, C. J., van den Oord, G. H. J., & Alkemade, F. J. M. 1995, Astronomy & Astrophysics, 296, 477

Meyer, J.-P. 1985, The Astrophysical Journal Supplement Series, 57, 173

Milligan, R. O., Chamberlin, P. C., Hudson, H. S., Woods, T. N., Mathioudakis, M., Fletcher, L., Kowalski, A. F., & Keenan, F. P. 2012, The Astrophysical Journal Letters, 748, L14

Miyawaki, S., Iwai, K., Shibasaki, K., Shiota, D., & Nozawa, S. 2016, The Astrophysical Journal, 818, 8

Moe, O. K., Cook, J. W., & Mango, S. A. 1979, Solar Physics, 61, 319

Münch, G. 1966, The Astrophysical Journal, 145, 237

Munro, R. H., & Withbroe, G. L. 1972, 1The Astrophysical Journal, 176, 511

Nakajima, H., et al. 1985, Publications of the Astronomical Society of Japan, 37, 163

Nakajima, H., et al. 1994, in IEEE Proceedings, Vol. 82, 705–713

Nasmyth, J. 1852, Monthly Notices of the Royal Astronomical Society1, 13, 5

National Research Council. 1981, Solar-Terrestrial Research for the 1980's (Washington, DC: The National Academies Press), 166

Nicolet, M. 1961, SAO Special Report, 75

Nuevo, F. A., Vásquez, A. M., Landi, E., & Frazin, R. 2015, The Astrophysical Journal, 811, 128

Oort, J. H. 1932, Bulletin of the Astronomical Institutes of the Netherlands, 6, 249

Orlando, S., Peres, G., & Reale, F. 2000, The Astrophysical Journal, 528, 524

Orlando, S., Peres, G., & Reale, F. 2001, in Solar encounter. Proceedings of the First Solar Orbiter Workshop, ed. B. Battrick, H. Sawaya-Lacoste, E. Marsch, V. Martinez Pillet, B. Fleck, & R. Marsden (Puerto de la Cruz: ESA Special Publication), 301–306

—. 2004, Astronomy and Astrophysics, 424, 677

Paetzold, H. K. 1963, in Space Research III: Proceedints of the Third International Space Science Symposium, ed. W. Priester (Washington, DC: North-Holland Publishing Co), 28

Paetzold, H. K., & Zschorner, H. 1961, in Space Research II: Proceedings of the Second International SPace Science Symposium, ed. H. C. van de Hulst, C. de Jager, & A. F. Moore (Florence: North-Holland Publishing Co), 958

Parenti, S. 2014, Living Reviews in Solar Physics, 11, 1

Parker, D. G., Ulrich, R. K., & Pap, J. M. 1998, Solar Physics, 177, 229

Pasachoff, J. M., & Muzyka, D. F. 1976, Vistas in Astronomy, 19, 341

Paschen, F. 1908, Annalen der Physik, 332, 537

Perlmutter, S., et al. 1999, The Astrophysical Journal, 517, 565

Pesnell, W. D. 2014, EVE MEGS-A and SAM have been Turned Off

Pesnell, W. D., Thompson, B. J., & Chamberlin, P. C. 2011, Solar Physics, 275, 3

Petkaki, P., Del Zanna, G., Mason, H. E., & Bradshaw, S. J. 2012, Astronomy & Astrophysics, 547, A25

Petralia, a., Reale, F., Testa, P., & Del Zanna, G. 2014, Astronomy & Astrophysics, 564, A3

Pickering, E. C. 1897, The Astrophysical Journal, 5, 92

Pickering, E. C., & Fleming, W. P. 1896, The Astrophysical Journal, 4, 369

Piddington, J. H., & Minnett, H. C. 1951, The Commonwealth Scientific and Industrial Research Organization Australia, 4, 131

Planck, M. 1900, Deutsche Physikalische Gesellschaft, 2, 237

Plowman, J., Kankelborg, C., & Martens, P. 2013, The Astrophysical Journal, 771, 2

Poduval, B., DeForest, C. E., Schmelz, J. T., & Pathak, S. 2013, The Astrophysical Journal, 765, 144

Qian, L., et al. 2014, in Modeling the IonosphereThermosphere System, ed. J. Huba, R. W. Schunk, & G. Khazanov (Washington, DC: John Wiley & Sons), 73–83

Raouafi, N. E., Riley, P., Gibson, S., Fineschi, S., & Solanki, S. K. 2016, Frontiers in Astronomy and Space Sciences, 3, 20

Reale, F., Guarrasi, M., Testa, P., Deluca, E. E., Peres, G., & Golub, L. 2011, The Astrophysical Journal Letters, 736, L16

Reale, F., & Landi, E. 2012, Astronomy & Astrophysics, 543, A90

Reale, F., Landi, E., & Orlando, S. 2012, The Astrophysical Journal, 746, 18

Reames, D. V. 1999, The Astrophysical Journal, 518, 473

Reber, G. 1940, The Astrophysical Journal, 91, 621

—. 1944, The Astrophysical Journal, 100, 279

Rich, F. J. 1985, in Handbook of Geophysics and the Space Environment, ed. A. S. Jursa (Springfield: Air Force Geophysics Laboratory), 9.1–9.4

Richards, P. G., Fennelly, J. A., & Torr, D. G. 1994, Journal of Geophysical Research, 99, 8981

Ridley, A. J., Deng, Y., & Tóth, G. 2006, Journal of Atmospheric and Solar-Terrestrial Physics, 68, 839

Riess, A. G., et al. 1998, The Astronomical Journal, 116, 1009

Rosner, R., Tucker, W. H., & Vaiana, G. S. 1978, The Astrophysical Journal, 220, 643

Rubin, V. C., Ford, J. W. K., & Thonnard, N. 1978, The Astrophysical Journal Letters, 225, L107

Rutherford, E. 1911, Philosophical Magazine, 21, 669

Rybicki, G. B., & Lightman, A. P. 1979, Radiative Processes in Astrophysics (John Wiley & Sons)

Saint-Hilaire, P., Hurford, G. J., Keating, G., Bower, G. C., & Gutierrez-Kraybill, C. 2012, Solar Physics, 277, 431

Sanz-Forcada, J., Brickhouse, N. S., & Dupree, A. K. 2003, The Astrophysical Journal Supplement Series, 145, 147

Scherrer, P. H., et al. 2011, Solar Physics, 275, 207

Schmahl, E. J., & Kundu, M. R. 1995, Journal of Geophysical Research, 100, 19851

Schmahl, E. J., & Kundu, M. R. 1998, in Astronomy Society of the Pacific Conference Series, ed. K. S. Balasubramaniam, J. Harvey, & D. Rabin, Vol. 140, San Francisco, CA, 387–399

Schonfeld, S. J., White, S. M., Henney, C. J., Arge, C. N., & McAteer, R. T. J. 2015, The Astrophysical Journal, 808, 29

Schonfeld, S. J., White, S. M., Hock-Mysliwiec, R. A., & McAteer, R. T. J. 2017, The Astrophysical Journal, 844, 163

Schou, J., et al. 2011, Solar Physics, 275, 229

Schrijver, C. J., & McMullen, R. A. 2000, The Astrophysical Journal, 531, 1121

Schrijver, C. J., & Siscoe, G. L., eds. 2009, Heliophysics: Plasma Physics of the Local Cosmos (New York: Cambridge University Press)

Schunk, R. W., & Nagy, A. F. 2004, Ionospheres: Physics, Plasma Physics, and Chemistry (Cambridge University Press)

Selhorst, C. L., Costa, J. E. R., Giménez de Castro, C. G., Valio, A., Pacini, a. a., & Shibasaki, K. 2014, The Astrophysical Journal, 790, 134

Selhorst, C. L., Giménez de Castro, C. G., Válio, a., Costa, J. E. R., & Shibasaki, K. 2011, The Astrophysical Journal, 734, 64

Smolkov, G. I., Pistolkors, A. A., Treskov, T. A., Krissinel, B. B., & Putilov, V. A. 1986, Astrophysics and Space Science, 119, 1

Solomon, S. C., & Qian, L. 2005, Journal of Geophysical Research: Space Physics, 110, A10306

Southworth, G. C. 1945, in Classics in Radio Astronomy, ed. W. T. Sullivan (Springer Netherlands), 168–181

Suess, K., Snow, M., Viereck, R., & Machol, J. 2016, Journal of Space Weather and Space Climate, 6, A10

Sun, X., Hoeksema, J. T., Liu, Y., Wiegelmann, T., Hayashi, K., Chen, Q., & Thalmann, J. 2012, Astrophys. J., 748, 77

Svalgaard, L., & Hudson, H. S. 2010, Astronomy Society of the Pacific Conference Series, 428, 325

Swarup, G., Kakinuma, T., Covington, A. E., Harvey, G. A., Mullaly, R. F., & Rome, J. 1963, The Astrophysical Journal, 137, 1251

Tanaka, H., Castelli, J. P., Covington, A. E., Krüger, A., Landecker, T. L., & Tlamicha, A. 1973, Solar Physics, 29, 243

Tanaka, H., & Kakinuma, T. 1957, Proceedings of the Research Institute of Atmospherics, Nagoya University, 4, 60

Tapping, K. F. 1987, Journal of Geophysical Research, 92, 829

—. 2013, Space Weather, 11, 394

Tapping, K. F., Boteler, D., Charbonneau, P., Crouch, a., Manson, a., & Paquette, H. 2007, Solar Physics, 246, 309

Tapping, K. F., Cameron, H. T., & Willis, A. G. 2003, Solar Physics, 215, 357

Tapping, K. F., & Charrois, D. P. 1994, Solar Physics, 150, 305

Tapping, K. F., & DeTracey, B. 1990, Solar Physics, 127, 321

Tapping, K. F., & Valdés, J. J. 2011, Solar Physics, 272, 337

Teriaca, L., Warren, H. P., & Curdt, W. 2012, The Astrophysical Journal Letters, 754, L40

Testa, P., Drake, J. J., & Landi, E. 2012, The Astrophysical Journal, 745, 111

Timothy, A. F., Krieger, A. S., & Vaiana, G. S. 1975, Solar Physics, 42, 135

Tobiska, W. K. 1996, Advances in Space Research, 18, 3

Tobiska, W. K., Bouwer, S. D., & Bowman, B. R. 2008, Journal of Atmospheric and Solar-Terrestrial Physics, 70, 803

Tokumaru, M., Satonaka, D., Fujiki, K., Hayashi, K., & Hakamada, K. 2017, Solar Physics, 292, 41

Tomczyk, S., et al. 2008, Solar Physics, 247, 411

Torii, C., Tsukiji, Y., Kobayashi, S., Yoshimi, N., Tanaka, H., & Enome, S. 1979, Proceedings of the Research Institute of Atmospherics, Nagoya University, 26, 129

Tóth, G., et al. 2005, Journal of Geophysical Research (Space Physics), 110, A12226

Tripathi, D., Mason, H. E., Young, P. R., & Zanna, G. D. 2008, Astronomy & Astrophysics Special feature, 481, 53

Truhlik, V., Bilitza, D., & Triskova, L. 2012, Earth, Planets and Space, 64, 531

Tsuchiya, A., & Nagane, K. 1965, Publications of the Astronomical Society of Japan, 17, 86

Tziotziou, K., Georgoulis, M. K., & Liu, Y. 2013, The Astrophysical Journal, 772, 115

Vásquez, A. M. 2016, Advances in Space Research, 57, 1286

Vats, H. O., Deshpande, M. R., Shah, C. R., & Mehta, M. 1998, Solar Physics, 181, 351

Veck, N. J., & Parkinson, J. H. 1981, Monthly Notices of the Royal Astronomical Society, 197, 41

Walsh, R. W., & Ireland, J. 2003, The Astronomy and Astrophysics Review, 12, 1

Wang, Z., Gary, D. E., Fleishman, G. D., & White, S. M. 2015, The Astrophysical Journal, 805, 93

Warren, H. P. 2014, The Astrophysical Journal Letters, 786, L2

Warren, H. P., & Brooks, D. H. 2009, The Astrophysical Journal, 700, 762

Warren, H. P., Brooks, D. H., & Winebarger, A. R. 2011, The Astrophysical Journal, 734, 90

Warren, H. P., Byers, J. M., & Crump, N. A. 2017, The Astrophysical Journal, 836, 215

Warren, H. P., Mariska, J. T., & Doschek, G. a. 2013, The Astrophysical Journal, 770, 116

Warren, H. P., Winebarger, A. R., & Brooks, D. H. 2012, The Astrophysical Journal, 759, 141

White, S. M. 1999, Solar Physics, 190, 309

—. 2005, in Solar and Space Weather Radiophysics: Current Status and Future Developments, ed. D. E. Gary & C. U. Keller (Dordrecht: Springer Netherlands), 89–113

White, S. M., & Kundu, M. R. 1997, Solar Physics, 174, 31

White, S. M., Kundu, M. R., & Gopalswamy, N. 1992, The Astrophysical Journal, 78, 599

White, S. M., Thomas, R. J., Brosius, J., & Kundu, M. R. 2000, The Astrophysical Journal, 534, 203

Wild, J. P., Smerd, S. F., & Weiss, A. A. 1963, Annual Review, Astronomy &Astrophysics, 1, 291

Wilson, R. M., Rabin, D., & Moore, R. L. 1987, Solar Physics, 111, 279

Withbroe, G. L., & Noyes, R. W. 1977, Annual Review of Astronomy and Astrophysics, 15, 363

Wood, K., & Raymond, J. 2000, The Astrophysical Journal, 540, 563

Woods, T. N., et al. 2000, Physics and Chemistry of the Earth C, 25, 393

—. 2012, Solar Physics, 275, 115

Yan, Y., Zhang, J., Wang, W., Liu, F., Chen, Z., & Ji, G. 2009, Earth, Moon, and Planets, 104, 97

Young, P. R., Watanabe, T., Hara, H., & Mariska, J. T. 2009, Astronomy & Astrophysics, 495, 587

Zhang, J., Kundu, M. R., White, S. M., Dere, K. P., & Newmark, J. S. 2001, The Astrophysical Journal, 561, 396

Zhang, J., White, S. M., & Kundu, M. R. 1998, The Astrophysical Journal, 504, L127

Zhang, Q.-h., et al. 2016, Research in Astronomy and Astronphysics, 16, 167

Zhu, C., Liu, R., Alexander, D., & Mcateer, R. T. J. 2016, The Astrophysical Journal Letters, 821, L29

Zirin, H., Baumert, B. M., & Hurford, G. J. 1991, The Astrophysical Journal, 370, 779

Zirker, J. B. 1977, in Coronal Holes and High Speed Wind Streams, ed. J. B. Zirker, 1–26

Zirker, J. B. 1993, Solar Physics, 148, 43

Zwicky, F. 1933, Helvetica Physica Acta, 6, 110